1 **Aerosol optical properties calculated from size distributions, filter samples and absorption photometer data**

2 **at Dome C, Antarctica and their relationships between seasonal cycles of sources**

4 Aki Virkkula[1,3], Henrik Grythe[2], John Backman[1], Tuukka Petäjä[3], Maurizio Busetto[4], Christian Lanconelli[4,6],

5 Angelo Lupi[5], Silvia Becagli[7,8], Rita Traversi[7,8], Mirko Severi[7,8], Vito Vitale[5],

6 Patrick Sheridan[9], Elisabeth Andrews[9,10]

8 [1]Finnish Meteorological Institute (FMI), Erik Palmenin aukio 1, P.O.Box 503, FI-00101 Helsinki

9 [2]Norwegian Institute for Air Research (NILU), P.O.Box 100, 2027 KJELLER

10 [3]University of Helsinki, Institute for Atmospheric and Earth System Research (INAR) / Physics, Faculty of

11 Science, Helsinki, Finland

12 [4]National Research Council of Italy, Institute of Atmospheric Sciences and Climate (CNR-ISAC), Via P. Gobetti

13 101, 40129 Bologna, Italy

14 [5]National Research Council of Italy, Institute of Polar Sciences (CNR-ISP), Via P. Gobetti 101, 40129 Bologna,

15 Italy

16 [6]European Commission, Joint Research Centre, Ispra (VA), Italy

17 [7]University of Florence, Dept. of Chemistry, Sesto Fiorentino (Florence) – Italy

18 [8]National Research Council of Italy, Institute of Polar Sciences (CNR-ISP), University of Venice, V. Torino 155,

19 30172 Venice-Mestre, Italy.

20 [9]NOAA Global Monitoring Laboratory, Boulder (CO), USA

21 [10]Cooperative Institute for Research in Environmental Sciences, University of Colorado, Boulder (CO), USA

23 Correspondence to: A. Virkkula (aki.virkkula@fmi.fi)

25 **Abstract**

26 Optical properties of surface aerosols at Dome C, Antarctica in 2007-2013 and their potential source areas are

27 presented. Scattering coefficients (σ_{sp}) were calculated from measured particle number size distributions with a

28 Mie code and from filter samples using mass scattering efficiencies. Absorption coefficients (σ_{ap}) were

29 determined with a 3-wavelength Particle Soot Absorption Photometer (PSAP) and corrected for scattering by

30 using two different algorithms. The scattering coefficients were also compared with σ_{sp} measured with a

31 nephelometer at the South Pole Station (SPO). The minimum σ_{ap} was observed in the austral autumn and the

32 maximum in the austral spring, similar to other Antarctic sites. The darkest aerosol, i.e., the lowest single

scattering albedo $\omega_o \approx 0.91$ was observed in September and October and the highest $\omega_o \approx 0.99$ in February and March. The uncertainty of the absorption Ångström exponent α_{ap} is high. The lowest α_{ap} monthly medians were observed in March and the highest in August – October. The equivalent black carbon (eBC) mass concentrations were compared with eBC measured at three other Antarctic sites: the SPO and two coastal sites, Neumayer and Syowa. The maximum monthly median eBC concentrations are almost the same (~3 ± 1 ng m^{-3}) at all these sites in October-November. This suggests that there is no significant difference in eBC concentrations between the coastal and plateau sites. The seasonal cycle of the eBC mass fraction exhibits a minimum f(eBC) $\approx$ 0.1% in February-March and a maximum ~4-5% in August-October. Source areas were calculated using 50-day FLEXPART footprints. The highest eBC concentrations and the lowest ω_o were associated with air masses coming from South America, Australia and Africa. Vertical simulations that take BC particle removal processes into account show that there would be essentially no BC particles arriving at Dome C from north of latitude 10°S at altitudes < 1600 m. The main biomass-burning regions Africa, Australia and Brazil are more to the south and their smoke plumes have been observed at higher altitudes than that so they can get transported to Antarctica. The seasonal cycle of BC emissions from wildfires and agricultural burning and other fires in South America, Africa and Australia were calculated from data downloaded from the Global Fire Emissions Database (GFED). The maximum total emissions were in August-September but the peak of monthly average eBC concentrations is observed 2 – 3 months later in November not only at Dome C but also at SPO and the coastal stations. The air mass residence-time-weighted BC emissions from South America are approximately an order of magnitude larger than from Africa and Oceania suggesting that South American BC emissions are the largest contributors to eBC at Dome C. At Dome C the maximum and minimum scattering coefficients were observed in austral summer and winter, respectively. At SPO σ_{sp} was similar to that observed at Dome C in the austral summer but there was a large difference in winter, suggesting that in winter SPO is more influenced by sea spray emissions than Dome C. The seasonal cycles of σ_{sp} at Dome C and at the SPO were compared with the seasonal cycles of secondary and primary marine aerosol emissions. The σ_{sp} measured at SPO correlated much better with the sea-spray aerosol emission fluxes in the Southern Ocean than σ_{sp} at Dome C. The seasonal cycles of biogenic secondary aerosols were estimated from monthly average phytoplankton biomass concentrations obtained from the CALIOP satellite sensor data. The analysis suggests that a large fraction of the biogenic scattering aerosol observed at Dome C has been formed in the polar zone but it may take a month for the aerosol to be formed, grown and get transported from the sea level to Dome C.

1. Introduction

The Antarctic interior region has scarce observations of atmospheric constituents and many aspects of the atmospheric properties are underdetermined. The Antarctic dome or the polar vortex, which is much stronger than its northern counterpart and present throughout the year (Karpetchko et al., 2005), at most times efficiently prevents transport into the Antarctic troposphere from lower latitudes. However, wildfires and agricultural burning emissions from Africa, South America and Australia do affect vast regions of the southern hemisphere, including Antarctica. For instance, Hara et al. (2010) found that haze episodes at Syowa Station, during which visibility can drop to 10 km for periods of ~30 h, were caused by biomass burning aerosol from South America transported to the Antarctic coast via the eastward approach of cyclones. At the Neumayer station large-scale meridional transport of biomass-burning derived black carbon, preferentially from South America, seems to determine the BC burden and causes a distinct and consistent spring / early summer concentration maximum (Weller et al., 2013).

Concordia station lies on Dome C (75°06'S, 123°23'E), at 3233 m above sea level (a.s.l.) on the East Antarctic plateau, about 1100 km from the nearest coastline, the Ross Sea. The base is French / Italian operated, with research fields within astronomy and glaciology as well as atmospheric sciences. The atmospheric instrumentation is located in a small cabin southwest of the main base (at the site described by Udisti et al., 2012) where it is upwind of the base at the prevailing wind directions. Concordia is one of only three permanent year-round stations operated on the Antarctic Plateau, the others being the American Amundsen-Scott observatory (South Pole (SPO), 2835 m.a.s.l., about 1300 km from the nearest open sea, 1600 km away from Dome C) and the Russian Vostok station (78°28'S, 106°51'E, 3488 m.a.s.l., 600km away). Thus, there are large spatial distances between the continuous atmospheric observation. However, properties of the Antarctic atmosphere tend to extend both over longer temporal and spatial scales than elsewhere (Fiebig et al., 2014) suggesting that the scarce observations that exist can be assumed to be representative of larger areas than typical in other climate regions. This would imply that Dome C is an important indicator for the entire Antarctic inland. Though measurement conditions are harsh the continuous long-term monitoring provided here can be a baseline for the aerosol optical properties of the Antarctic inland and may provide indications of changes in atmospheric constituents and aerosol levels.

There are several studies on the aerosol chemical composition at Dome C (e.g., Jourdain et al., 2008; Becagli et al., 2012, 2021; Udisti et al., 2004, 2012; Legrand et al., 2016, 2017a, 2017b), and also the aerosol optical depth (AOD) has been measured there (Tomasi et al., 2007). However, in situ surface aerosol scattering and

absorption coefficients at Dome C have not been presented. The light absorption coefficient and particle number size distributions (PNSD) have been measured continuously with a 3-wavelength Particle Soot Absorption Photometer (PSAP) and a differential mobility particle sizer (DMPS) since 2007. The PNSD data have already been used in several papers. Järvinen et al. (2013) analyzed the seasonal cycle and modal structure of PNSD measured with the DMPS, Chen et al. (2017) analyzed number size distribution of air ions measured with an Air Ion Spectrometer (AIS) and the PNSD measured with the DMPS and Lachlan-Cope et al. (2020) used the Dome C DMPS data for comparing with the PNSD measured at the coastal site Halley. The PSAP data, however, have not been presented in detail. Caiazzo et al. (2021) used some of the PSAP data mainly for evaluating elemental carbon (EC) sample contamination. Grythe (2017) used the data from 2007-2013 as part of his PhD thesis but in the present paper we will analyze that period in more detail. Here we will describe the methods for measuring absorption and calculating scattering from the size distributions and filter samples.

The goals of the paper are to present descriptive statistics of extensive and intensive aerosol optical properties at Dome C in 2007 – 2013, their seasonal cycles and the relationships between the seasonal cycles of major sources of absorbing and scattering aerosols. The AOPs will be compared with other observations from other Antarctic sites, in most detail the scattering coefficients measured at the South Pole.

2. Methods

2.1 Sampling site

Concordia station is a permanently operated French / Italian Antarctic research base on East Antarctic plateau. The observations are performed in isolated sites around the main base. The Dome C sampling site is the same as used by Udisti et al. (2012), Becagli et al. (2012), and Järvinen et al. (2013). It is located about 1 km southwest of the station main buildings, upwind in the direction of the prevailing wind. The northeastern direction (10°–90°) has been declared as the contaminated sector. Below the validity of the contaminated sector will be analyzed by using the absorption photometer data. For in situ aerosol instrumentation the sample air was taken at the flowrate of 5 Liters Per Minute (LPM) from the roof of the cabin with a straight 2-m long 25-mm diameter stainless steel tube inlet. It was covered with a protective cap to protect against snow fall and ice buildup.

2.2 Instruments

2.2.1 Aerosol measurements

Light absorption by particles was measured with a Radiance Research 3λ PSAP at three wavelengths, λ = 467 nm, 530 nm, and 660 nm. There was no nephelometer measuring scattering coefficient so it was calculated from particle size distributions and filter sample data as described below. Particle number size distributions were measured at 10-minute time resolution in the size range 10 – 620 nm with a custom-built differential mobility particle sizer (DMPS) as described by Järvinen et al. (2013) and in the size range 0.3 – 20 µm with a Grimm model 1.108 optical particle counter (OPC) in 2007 – 2009. RH was not measured in the Dome C sample air but it can be safely claimed that it was dry. The absolute humidity in the air on the upper plateau is very low and temperature varies from colder than about -20°C in the austral summer down to about 80°C in the austral winter. When air is sampled to the instruments in the measurement containers where temperature is > +10 °C RH decreases to very low values. In addition to the in-situ instruments, PM_1 and PM_{10} filter samples were collected for chemical analyses by ion chromatography. The length of the sampling period of the PM_1 and PM_{10} samples was 3 or 4 days and 1 day, respectively.

The data coverage for the PSAP, the DMPS, the OPC and the PM_1 and PM_{10} filter sample data are presented in Fig. 1. The number of hours of accepted data and the number of samples are shown in parentheses for the continuous instruments and the filter samplers, respectively. The filtering criteria will be presented below (section 2.4).

2.2.2 Meteorological measurements

Ambient air temperature (t), relative humidity (RH), wind speed (WS) and wind direction (WD) data were from the routine meteorological observation at Station Concordia as part of the IPEV/PNRA Project - a collaborative project between "Programma Nazionale di Ricerche in Antartide" (PNRA) and Institut Polaire Français Paul-Emile Victor (IPEV) (www.climantartide.it).

2.3 Data processing

2.3.1 Mass concentrations from size distributions

60-minute average size distributions $n(D_p)$ were first calculated from the original 10-minute data and corrected for STP (p = 1013 hPa, T = 273.15 K). The DMPS $n(D_p)$ data were corrected for diffusion losses during the inversion (Järvinen et al., 2013; Chen et al., 2017). Mass concentration were calculated from the number size distributions measured with the DMPS from

$$m(\text{DMPS}) = \rho_\text{p} V(\text{DMPS}) = \rho_\text{p} \int\limits_{10\text{nm}}^{620\text{nm}} \tfrac{\pi}{6} D_\text{p}^3 n(D_\text{p}) dD_\text{p} \tag{1}$$

2   where the density ρ_p = 1.7 g cm^{-3} was used. For particle density of 1.7 g cm^{-3} the particle diameter 620 nm

3   corresponds to the aerodynamic diameter $D_a = \sqrt{\rho_p/\rho_0}\, D_p = \sqrt{1.7} \times 620 nm \approx$ 808 nm, where ρ_0 = 1 g cm^{-3}.

4   To be consistent with the definitions of filter-sample size ranges that typically show the upper aerodynamic

5   diameter of a sampler inlet the mass concentration calculated from Eq. (1) will be referred to as

6   m(DMPS,PM$_{0.8}$) and the volume concentration as V(DMPS,PM$_{0.8}$).

8   In December 2007 – July 2009 there was also the Grimm 1.108 OPC that measures number concentrations of

9   particles in the D_p range of 0.3 – 20 µm. The particle number concentrations in the size range Dp > 1 µm were

10   first corrected for wind-speed dependent and particle diameter dependent inlet and sampling tube losses as

11   described in the supplement. The three largest channels of the OPC measure the number concentrations in D_p

12   range of 7.5 – 20 µm. For an assumed density ρ_p = 1.7 g cm^{-3} the diameter D_p = 7.5 µm corresponds to the

13   aerodynamic diameter D_a = 9.8 µm. Assuming that ρ_p is constant over the whole size range the mass

14   concentration of particles smaller than D_a = 10 µm is calculated from the number size distributions by excluding

15   the three largest particle OPC channels as

$$m\big(n(D_\text{p}), \text{PM}_{10}\big) = \rho_\text{p} V\big(n(D_\text{p}), \text{PM}_{10}\big) = \rho_\text{p}\big(V(\text{DMPS}, \text{PM}_{0.8}) + V(\text{OPC}, \text{PM}_{0.8-10})\big) \tag{2}$$

17 The fraction of volume concentration measured by the DMPS equals

$$fV(\text{DMPS}) = \frac{V(\text{DMPS}, \text{PM}_{0.8})}{V\big(n(D_\text{p}), \text{PM}_{10}\big)} \tag{3}$$

19 This fraction was calculated from data collected during the simultaneous operation of the DMPS and the OPC.

20 The monthly average fV(DMPS) values presented in Table 1 were used for the period 2008 – 2013 to calculate

21 mass concentrations in the size range D_a < 10 µm from

$$m(\text{DMPS}, \text{PM}_{10}) = \frac{\rho_\text{p} V(\text{DMPS}, \text{PM}_{0.8})}{fV(\text{DMPS})} = \frac{m(\text{DMPS}, \text{PM}_{0.8})}{fV(\text{DMPS})} \tag{4}$$

23 In other words, the variable names m(DMPS,PM$_{0.8}$) and m(DMPS,PM$_{10}$) will be used below to emphasize that

24 these mass concentrations were calculated from DMPS data. The mass concentrations m(DMPS,PM$_{0.8}$) and

25 m(DMPS,PM$_{10}$) can be considered to be the lower and upper estimates of m.

27 **2.3.2 Scattering coefficients from the size distributions**

28 Scattering coefficients were calculated using the 60-minute average size distributions from

1 $$\sigma_{sp}(m, \lambda) = \int Q_s(D_p, m, \lambda) \tfrac{\pi}{4} D_p^2 n(D_p) dD_p \qquad\qquad (5)$$

2 where Q_s is the scattering efficiency calculated using the Mie code by Barber and Hill (1990), m is the refractive

3 index, λ is the wavelength and $n(D_p)$ is the particle number size distribution. Analogous to the mass

4 concentrations the scattering coefficients were determined from the simultaneous DMPS and OPC

5 measurements in December 2007 – July 2009 from

6 $$\sigma_{sp}\left(n(D_p), PM_{10}\right) = \sigma_{sp}(DMPS, PM_{0.8}) + \sigma_{sp}(OPC, PM_{0.8-10}) \qquad\qquad (6)$$

7 where $\sigma_{sp}(OPC, PM_{0.8})$ and $\sigma_{sp}(OPC, PM_{0.8-10})$ are the scattering coefficient calculated from the particle number

8 size distributions in the size ranges measured by the DMPS and the OPC, respectively. As explained above, the

9 number size distributions for $D_p > 1$ μm were corrected for the inlet and sampling tube losses. For

10 $\sigma_{sp}(DMPS, PM_{0.8})$ the refractive index of sulfuric acid (SA, H_2SO_4, $m_r = 1.426 + 0i$, Seinfeld and Pandis, 1998) was

11 used. This refractive index is slightly lower than that estimated for submicron aerosols at two low-altitude

12 Antarctic stations Aboa, and Neumayer in Queen Maud Land. Virkkula et al. (2006) measured particle number

13 size distributions in the size range $D_p < 800$ nm with a DMPS and light scattering of submicron particles with a

14 nephelometer at the Finnish a site about 130 km inland from the open Weddell Sea in January 2000. With an

15 iteration procedure matching nephelometer-measured and size-distribution-derived scattering coefficients the

16 real refractive indices were 1.43 ± 0.07 and 1.45 ± 0.04 at $\lambda = 550$ nm for all data and excluding new particle

17 formation, respectively. Juránýi and Weller (2019) measured size distributions with an SMPS and a laser

18 aerosol spectrometer (LAS) for a full year at the coastal site Neumayer and by fitting data of the two

19 instruments in the overlapping range of 120 - 340 nm obtained $m_r = 1.44 ± 0.08$. Considering that both Aboa

20 and Neumayer are closer to sources of ammonia that neutralizes aerosol and increases the refractive index

21 above that of pure sulfuric acid (1.426) it was assumed here that the use of 1.426 for the calculation of σ_{sp} from

22 the size range measured with the DMPS is reasonable. For the larger particle size range, $\sigma_{sp}(OPC, PM_{0.8-10})$ the

23 refractive index of NaCl ($m_r = 1.544$, Seinfeld and Pandis, 1998) was used. This value is in line with the average

24 refractive index of 1.54 with a range from 1.50 to 1.58 in the particle size range 0.3 - 12 μm in impactor

25 samples taken at the South Pole (Hogan et al., 1979) and with the supermicron particle refractive index of 1.53

26 ± 0.02 calculated from the chemical composition of 12-stage impactor samples taken at the coastal site Aboa

27 (Virkkula et al., 2006).

29 The fraction of scattering coefficient measured by the DMPS was calculated from

30 $$f\sigma_{sp}(DMPS, \lambda) = \frac{\sigma_{sp}(DMPS, PM_{0.8}, \lambda)}{\sigma_{sp}\left(n(D_p), PM_{10}, \lambda\right)} \qquad\qquad (7)$$

1   The wavelengths of λ = 467 nm, 530 nm, and 660 nm were used to match the PSAP data. Similar to fV(DMPS),

2    $f\sigma_{sp}$(DMPS,λ) was calculated from data collected during the simultaneous operation of the DMPS and the OPC,

3   the seasonal monthly statistics were calculated (Table 1) and the respective monthly averages were applied to

4   the period 2008 – 2013 to calculate σ_{sp} in the size range D_a < 10 μm from

$$\sigma_{sp}(\mathrm{DMPS,PM}_{10},\lambda) = \frac{\sigma_{sp}(\mathrm{DMPS,PM}_{0.8},\lambda)}{f\sigma_{sp}(\mathrm{DMPS},\lambda)} \tag{8}$$

6   The wavelength symbol λ will be used below only when necessary. The variable names σ_{sp}(DMPS,PM$_{0.8}$) and

7   σ_{sp}(DMPS,PM$_{10}$) will be used to emphasize that these scattering coefficients were calculated from DMPS data in

8   the aerodynamic particle size ranges D_a < 0.8 μm and D_a < 10 μm. The scattering coefficients σ_{sp}(DMPS,PM$_{0.8}$)

9   and σ_{sp}(DMPS,PM$_{10}$) can also be considered to be the lower and upper estimates of σ_{sp} at the given

10   wavelength.

12   Figure 2 shows the average particle number, volume and scattering size distributions at λ = 530 nm in the size

13   range 10 nm – 10 μm and the respective normalized cumulative size distributions in the size range of 10 nm –

14   7.5 μm during the period from 14 December 2007 to 14 July 2009 in summer and in winter. Fig. 2a and 2b show

15   that for the number concentrations the OPC size range plays an insignificant role whereas the larger particles

16   contribute significantly to both total particle volume concentration (Figs. 2c and 2d) and scattering coefficients

17   (Figs. 2e and 2f) and that this contribution varies seasonally. The contributions of fV(DMPS) and $f\sigma_{sp}$(DMPS,λ)

18   were calculated for hourly-averaged size distributions from Eqs. (3) and (7), the monthly seasonal statistics

19   were calculated and presented in Table 1 and as a boxplot in Fig. 3. Both the table and the boxplot show that

20   both fV(DMPS) and $f\sigma_{sp}$(DMPS,λ) have maxima in summer and minima in winter. They also show that the

21   ranges are large. Consequently the use of the monthly averages presented in Table 1 for calculating

22   m(DMPS,PM$_{10}$) and σ_{sp}(DMPS,PM$_{10}$), Eqs. (4) and (8), creates an additional uncertainty to the results. Another

23   important result is that the wavelength dependency of $f\sigma_{sp}$(DMPS,λ) is clear and it also has a seasonal cycle.

25   The wavelength dependency of the scattering coefficient can be described by the scattering Ångström

26   exponent

$$\alpha_{sp} = -\frac{\ln\left(\sigma_{sp}(\lambda_1)\big/\sigma_{sp}(\lambda_2)\right)}{\ln\left(\lambda_1/\lambda_2\right)} \tag{9}$$

28   that was calculated by using the wavelength pair 467/660 nm. The variable names α_{sp}(DMPS,PM$_{0.8}$) and

29   α_{sp}(DMPS,PM$_{10}$) will be used below for α_{sp} calculated from σ_{sp}(DMPS,PM$_{0.8}$) and σ_{sp}(DMPS,PM$_{10}$), respectively.

1 **2.3.3 Absorption coefficients and equivalent black carbon concentrations**

2 The PSAP data were first corrected for flow and spot size. The flow was calibrated 37 times during 2007 - 2013

3 with a TSI flow meter. The slopes and offsets of the calibrations were interpolated for each hour and the PSAP

4 flows were corrected accordingly. All absorption coefficients were corrected to STP (1013.25 hPa and 273.15

5 K).

7 The PSAP measures signal and reference detector counts and the respective sums, $\sum SIG$ and $\sum REF$ are used

8 for calculating non-scattering-corrected absorption coefficient, here $\sigma_{ap,nsc}$, from

$$\sigma_{ap,nsc} = f(Tr)\frac{A}{Q\Delta t}\ln\left(\frac{\left(\sum_{\Delta t} SIG \Big/ \sum_{\Delta t} REF\right)_{t-\Delta t}}{\left(\sum_{\Delta t} SIG \Big/ \sum_{\Delta t} REF\right)_{t}}\right) = f(Tr)\sigma_0 \qquad (10)$$

10 where A is the filter spot area, Q the flow rate, Tr = $(\Sigma SIG/\Sigma REF)_t/(\Sigma SIG/\Sigma REF)_{t=0}$ is the transmittance, f(Tr) the

11 loading correction function and Δt the count integration time. The PSAP reports $\sigma_{ap,nsc}$ with a 0.1 Mm^{-1}

12 resolution at a 1-second time resolution. Averaging the 1-sec data is not good enough since at Dome C

13 absorption coefficients are most of the time clearly lower than 0.1 Mm^{-1}. Therefore the signal and reference

14 counts ΣSIG and ΣREF were used in (10) with Δt = 60 min. Manufacturer-cut spots of the standard filter

15 material Pallflex E70-2075W were used in the PSAP. The spot diameter was measured to be 4.9 ± 0.1 mm, so

16 the spot area A was 18.9 ± 0.6 mm^2. The uncertainty of A is ~3%.

18 Transmittance is reduced mainly by light absorption but also also due to scattering aerosol which results in the

19 so-called apparent absorption and has to be taken into account in the data processing. There are different

20 algorithms for processing PSAP data, e.g. by Bond et al. (1999), Virkkula et al. (2005), Müller et al. (2014), and Li

21 et al. (2020). Here we will use both the algorithm presented by Bond et al. (1999) (here B1999) with the

22 adjustment presented by Ogren (2010):

$$\sigma_{ap} = \frac{1}{1.22}\left(\frac{0.97\cdot 0.873}{1.0796\cdot Tr + 0.71}\sigma_0 - 0.02\cdot\sigma_{sp}\right) = \frac{1}{1.5557\cdot Tr + 1.0227}\sigma_0 - 0.0164\cdot\sigma_{sp} = \sigma_{ap,nsc} - 0.0164\cdot\sigma_{sp} \qquad (11)$$

24 and the algorithm presented by Virkkula et al. (2005) with the constants updated by Virkkula (2010) (here

25 V2010):

$$\sigma_{ap} = \left(k_0 + k_1(h_0 + h_1\omega_0)\, ln(Tr)\right)\sigma_0 - s\cdot\sigma_{sp} \qquad (12)$$

27 where

$$\omega_0 = \sigma_{sp}\Big/\left(\sigma_{sp} + \sigma_{ap}\right) \qquad (13)$$

1   is the single-scattering albedo and k_0, k_1, h_0, h_1, and s are wavelength-dependent constants. In the rest of the

2   paper the symbol $\sigma_{ap,nsc}$ will be used to present the non-scattering-corrected absorption coefficient, corrected

3   with the constants and formula in Eq. (11) excluding the subtraction of σ_{sp}.

5   Since there are the above-explained size-dependent uncertainties of scattering coefficient, additional

6   absorption coefficient estimates were calculated by using both algorithms. The upper estimates of absorption

7   coefficients $\sigma_{ap}(\sigma_{sp}(DMPS,PM_{0.8}))$ were calculated by using the lower estimate of scattering coefficient σ_{sp} =

8     $\sigma_{sp}(DMPS,PM_{0.8})$ in the scattering corrections in Eqs. (11) and (12) and the lower estimates of absorption

9   coeffcient $\sigma_{ap}(\sigma_{sp}(DMPS,PM_{10}))$ were calculated by using the upper estimate of scattering coefficient σ_{sp} =

10     $\sigma_{sp}(DMPS,PM_{10})$ in the scattering corrections. Consequently the lower and upper estimates of ω_o are denoted

11   as $\omega_o(\sigma_{sp}(DMPS,PM_{0.8}))$ and $\omega_o(\sigma_{sp}(DMPS,PM_{10}))$, respectively. They were calculated by using both Eqs. (11) and

12   (12) for calculating σ_{ap}.

14   Considering that the period with the simultaneous measurements with the DMPS and the OPC showed that the

15   DMPS size range always leads to an underestimation of both aerosol mass and scattering coefficient, it is likely

16   that σ_{ap} corrected for scattering with $\sigma_{sp}(DMPS, PM_{10})$ is closer to the true σ_{ap} than that corrected with

17     $\sigma_{sp}(DMPS, PM_{0.8})$. In the results both $\sigma_{ap,nsc}$, $\sigma_{ap}(\sigma_{sp}(DMPS,PM_{0.8}))$ and $\sigma_{ap}(\sigma_{sp}(DMPS,PM_{10}))$ will be presented to

18   evaluate the effect of using only the size range mesured with the DMPS for the scattering correction.

20   Similar to σ_{sp}, the wavelength dependency of light absorption by particles can roughly be described by the

21   absorption Ångström exponent:

22        $$\alpha_{ap} = -\frac{\ln\left(\sigma_{ap}(\lambda_1)/\sigma_{ap}(\lambda_2)\right)}{\ln\left(\lambda_1/\lambda_2\right)} \qquad (14)$$

23   that was calculated by using λ = 467 nm and 660 nm for $\sigma_{ap,nsc}$, $\sigma_{ap}(\sigma_{sp}(DMPS,PM_{10}))$ and both Eqs. (11) and

24   (12). The variable names $\alpha_{ap}(\sigma_{ap,nsc})$, $\alpha_{ap}(\sigma_{sp}(DMPS,PM_{10}),B1999)$ and $\alpha_{ap}(\sigma_{sp}(DMPS,PM_{10}),V2010)$, respectively,

25   will be used to denote the α_{ap} calculated in different ways. These calculations were conducted to study the

26   uncertainty of α_{ap} due to scattering corrections.

28   The absorption coefficient was used to estimate the concentration of equivalent black carbon, eBC (Petzold et

29   al. 2013) from:

30        $$eBC = \frac{\sigma_{ap}}{MAC} \qquad (15)$$

1   where MAC is the mass absorption coefficient. For freshly-emitted BC the MAC value is approximately 7.5 m^2

2   g^{-1} at λ = 550 nm (Bond et al., 2013). By assuming a wavelength-dependency of λ^{-1} this corresponds to MAC ≈

3   7.8 $m^2\ g^{-1}$ at λ = 530 nm. This can be considered to yield an upper estimate for eBC concentrations since for

4   coated BC particles MAC is larger (Bond et al.,2013). eBC was calculated by using $\sigma_{ap,nsc}$ and

5    $\sigma_{ap}(\sigma_{sp}(DMPS,PM_{10}))$ calculated with both algorithms, Eq. (11) and (12). The corresponding variable names

6   eBC($\sigma_{ap,nsc}$) and eBC($\sigma_{sp}(DMPS,PM_{10})$) will be used below for them. The scattering-corrected

7   eBC($\sigma_{sp}(DMPS,PM_{10})$) can be considered to be closer to the true eBC concentration. The reason for also

8   presenting eBC($\sigma_{ap,nsc}$) is that often an estimate of BC concentrations is needed even if it is known that it is an

9   upper estimate (Caiazzo et al., 2021). It is also comparable with the eBC often presented from Aethalometer

10   measurements. Presenting both yields a quantitative estimate of the bias due to not correcting the data for

11   scattering.

13   The eBC mass fractions in the two size ranges $D_a < 0.8$ µm and $D_a < 10$ µm were calculated from

$$feBC\left(m(DMPS,PM_{0.8})\right)=100\%\ \frac{eBC}{m(DMPS,PM_{0.8})} \tag{16}$$

$$feBC\left(m(DMPS,PM_{10})\right)=100\%\ \frac{eBC}{m(DMPS,PM_{10})} \tag{17}$$

16   where the mass concentrations m(DMPS,$PM_{0.8}$) and m(DMPS,PM_{10}) were defined in Eq. (4) and eBC calculated

17   from Eq. (15). Mass fractions were calculated for eBC($\sigma_{ap,nsc}$) and eBC($\sigma_{sp}(DMPS,PM_{10})$).

19   **2.3.4 Noise of scattering and absorption coefficients and eBC**

20   The uncertainty of scattering coefficients should in principle be calculated from the error propagation formula

21   $\left(\delta\sigma_{sp}\right)^2 = \Sigma\left(\partial\sigma_{sp}/\partial x_i\right)^2(\delta x_i)^2$, where δx_i is the uncertainty of variable x_i in calculating σ_{sp} (e.g., Sherman et

22   al., 2015). That would require taking into account all uncertainties of the size distribution measurements and

23   Mie modeling. However, a simplified approach was used here. The σ_{sp} calculated from the size distribution data

24   and the uncertainty of the size distribution range were used for calculating lower and upper estimates of σ_{sp} as

25   explained above. In addition to that the noise of σ_{sp} was estimated from the average of the absolute

26   differences of all two consecutive hourly-averaged scattering coefficients $\delta\sigma_{sp}$(average,1h) =

27   average($|\Delta\sigma_{sp}$(1h)$|$) = average($|\sigma_{sp}(t_{i+1}) - \sigma_{sp}(t_i)|$). The average noise of 24-h averages was calculated from

28   $\delta\sigma_{sp}(24h) = \delta\sigma_{sp}(average, 1h)/\sqrt{24}$. The noises were calculated for both $\sigma_{sp}(DMPS,PM_{0.8}$)) and

29   $\sigma_{sp}(DMPS,PM_{10})$. The noises are presented in Table 2. Note that the difference $|\sigma_{sp}(t_{i+1}) - \sigma_{sp}(t_i)|$ is not only due

30   to random noise so higher $|\Delta\sigma_{sp}|$ values are observed when σ_{sp} is in reality increasing or decreasing so the true

1   random noise is slightly lower. When σ_{sp} is used in calculating the scattering correction of σ_{ap} in B1999 (Eq.

2   (11)) σ_{sp} is multiplied by 0.0164. Consequently, the σ_{sp} noise for the 24-h averages results in a 0.0164σ_{sp} noise

3   for σ_{ap}. These noises are also presented in Table 2.

5   The uncertainty of the absorption coefficient should also be calculated from the error propagation formula,

6   similar to Sherman et al. (2015). However, here only the uncertainty of the spot size (~3%) and the statistical

7   noise are taken into account. The noise of the non-scattering-corrected hourly $\sigma_{ap,nsc}$ was estimated from the

8   average of the absolute differences of all two consecutive absorption measurements $\delta\sigma_{ap,nsc}$(average) =

9   average($|\Delta\sigma_{ap,nsc}|$) = average($|\sigma_{ap,nsc}(t_i) - \sigma_{ap,nsc}(t_i)|$) similar to the noise estimate of σ_{sp}. The noise of 24-hour

10 averages was estimated from $\delta\sigma_{ap,nsc}(24h) = \delta\sigma_{ap,nsc}(average, 1h)/\sqrt{24}$. The noise in the scattering-

11 corrected absorption cofficients were calculated from $\delta\sigma_{ap} = \delta\sigma_{ap,nsc} + 0.0164\delta\sigma_{sp}$ for both $\sigma_{ap}(\sigma_{sp}(DMPS,PM_{0.8}))$

12 and $\sigma_{ap}(\sigma_{sp}(DMPS,PM_{10}))$ and for 1h and 24h averages (Table 2). The noise determined this way is formally

13 correct only for σ_{ap} calculated with the B1999 formula, Eq. (11), not for V2010. However, calculated directly

14 fom the absolute differences, the average$|\Delta\sigma_{ap}(B1999)| \approx$ average$|\Delta\sigma_{ap}(V2010)|$, but the contribution of

15 scattering to the noise was only determined for B1999 as explained above. For V2010, Eq. (12) a formal error

16 propagation calculation is more complicated due to the iterative form of the procedure and it is out of the

17 scope of the present paper. The noise of eBC was calculated from $\delta(eBC(\sigma_{ap})) = \delta\sigma_{ap}/MAC$ for both non-

18 scattering-corrected and scattering-corrected eBC. The detection limits were defined as $2\times\delta(eBC(\sigma_{ap}))$. The

19 results are presented in Table 3.

21 The largest uncertainty factor for σ_{ap}, ω_o, α_{ap}, and eBC is not related to noise. It is due to the uncertainty of the

22 refractive index and size distributions used for calculating σ_{sp} and the algorithm. This was evaluated by

23 calculating σ_{ap} by using the lower and upper estimates of σ_{sp} in both scattering correction algorithms. These

24 four values were used then for calculating ω_o, α_{ap}, and eBC and they are presented below in relevant tables and

25 figures.

27 **2.4 Filtering and preprocessing the in situ data**

28 Both PSAP absorption and DMPS-derived scattering coefficient data were filtered manually by removing rapidly

29 changing values since they can be assumed to result from contamination from the station or from some

30 technical problem. The PSAP transmittance data were used to filter out data measured at Tr < 0.7 following

31 recommendations in WMO/GAW Report No. 227 (2016) and the PSAP handbook (Springston, 2018). During

32 most of 2010 the PSAP flow was extremely unstable so practically the whole year was removed.

All major sources of light absorbing aerosol other than the Dome C base are so far away that rapid variations in $\sigma_{ap,nsc}$ are due to either instrument malfunction or influence from the base, for instance emissions from vehicles. Further filtering of the data was done by removing data in which 10-minute averages of $\sigma_{ap,nsc}$ were more than 10 times larger than the hourly $\sigma_{ap,nsc}$. This was done to remove short events that are local but do not appear to come directly from the base, based on wind direction. In all roughly 13% of the data were deemed contaminated.

Additionally, wind data were used to remove clear contamination from the station. The sampling site is located upwind of the base itself by the prevailing wind directions. The base has a year-round diesel generator and vehicles operated within the base-area move around the base from November to February. Fig. 4 shows the distribution of $\sigma_{ap,nsc}$ in 5° wind direction (WD) sectors at wind speed WS > 2 m s^{-1}. The generator at the base is clearly observed as a pronounced peak of in $\sigma_{ap,nsc}$ at WD 60°. If the 75th percentile of the $\sigma_{ap,nsc}$ cumulative distribution is used as the criterion for the contaminated sector data when sector data when the wind direction was between 30°<WD<90° would be filtered which is 6 % of the of data. If the 99th percentile of $\sigma_{ap,nsc}$ is used the contamination sector is wider, 20°<WD<110°, and 10% of the data would be filtered. Here the latter, i.e., the stricter criterion was used. The distribution of $\sigma_{ap,nsc}$ in the same WD sectors at several wind speed intervals are shown in the supplement, Fig. S1. It is obvious that at low wind speeds contaminated air can come from all directions. Therefore, when WS < 2 m s^{-1} all data were filtered out, regardless of WD.

Since the size distribution and absorption measurements are done in the same cabin, the DMPS and OPC data were also removed when the PSAP observations indicated contamination. Fig. 1 shows the instruments' operational time in hours. The DMPS measurements had more gaps than the PSAP. The three instruments required for a valid measurement were not always operational at the same time. After filtering, altogether 15815 hours of data remained for the statistical analyses. No filtering was applied to the PM_1 and PM_{10} filter samples. The contamination is mainly BC so it was be assumed that the effect on ion concentrations was not significant.

The calculations were done using hourly-averaged data. These data were filtered to remove contaminated data as explained above. The filtered data were then averaged over 24 hours to reduce noise and improve detection limits. In the discussions below, the running 24-hour averages were used, centered at each hour, i.e. $\sigma_{ap}(t,24H)$ = average($\sigma_{ap}(t-12,1H),...,\sigma_{ap}(t+11,1H)$) which means, for instance, that at noon $\sigma_{ap}(t=12,24H)$ = average($\sigma_{ap}(t=0,1H)$, ... , $\sigma_{ap}(t=23,1H)$) so the noon average represents all absorption coefficients measured

1   during that day. If, during any period to be averaged, there were less than 12 hours of non-contaminated data

2   then that 24-hour average was excluded from further analysis.

2.5 Filter sample analyses and data processing

There were two samplers in the immediate vicinity of the cabin where the other in situ measurements were made. There was a PM_{10} sampling head operating following the CSN EN 12341 European Standard. The PM_1 samples were collected on the backup filter of a Dekati PM_{10} impactor. In both of these particles were sampled on Teflon filters (Pall-Gelman, 47-mm diameter, 2-μm nominal porosity). PM_{10} and PM_1 load is obtained by summing the mass of the ions determined on Teflon filters. Note that this can be considered to be the lower estimate since there could be unidentified compounds, such as organic carbon on the filters.

Just before the analysis, half of each filter was extracted with 10 mL of ultrapure water (18 MΩ Milli-Q) in ultrasonic bath for 20 min. Every filter manipulation was carried out under a class-100 laminar-flow hood, to minimize contamination risks. Inorganic anions and cations, as well as selected organic anions, were simultaneously measured by using a three Thermo Scientific Dionex ion-chromatography system, equipped with electrochemical-suppressed conductivity detectors. The sample handling during the IC injection was minimized by using a specifically-designed Flow-Injection Analysis (IC-FIA) device (Morganti et al., 2007). Cations (Na^+, NH_4^+, K^+, Mg^{2+} and Ca^{2+}) were determined by using a Thermo Scientific Dionex CS12A-4 mm analytical column with 20 mM H_2SO_4 eluent. Inorganic anions (Cl^-, NO_3^-, SO_4^{2-} and $C_2O_4^{2-}$) were measured by a Thermo Scientific Dionex AS4A-4 mm analytical column with a 1.8 mM Na_2CO_3/1.7 mM $NaHCO_3$ eluent. F^- and some organic anions (acetate, glycolate, formate and methanesulfonate) were determined by a Thermo Scientific Dionex AS11 separation column by a gradient elution (0.075–2.5 mM $Na_2B_4O_7$ eluent). Further details on the ion chromatographic measurements are reported in Udisti et al. (2004) and Becagli et al. (2011, 2021). All concentrations were corrected to STP (1013.25 hPa and 273.15 K). The ion data used in the present work is a subset of the data from 2005 to 2013 that Becagli et al. (2021) used for an analysis of the relationships between non-sea-salt sulfate, MSA, biogenic sources and environmental constraints.

In addition to calculating scattering coefficients from the DMPS data, PM_1 and PM_{10} mass concentrations were also used for calculating scattering coefficients. The scattering coefficients were calculated by multiplying the mass concentrations with mass scattering efficiencies (MSE) presented by Hand and Malm (2007). The PM_{10} mass concentrations were multiplied by the mass scattering efficiency of 1.9 m^2 g^{-1} and the PM_1 concentrations were multiplied by 3.6 m^2 g^{-1}. These are the MSE for "total mixed" aerosol and "fine mixed" aerosol in the Table

1   5 in Hand and Malm (2007), respectively. It has to be kept in mind that the MSE values in the above-mentioned

2   paper were derived from measurements in the continental USA so they most likely have a high uncertainty

3   when applied to the Dome C aerosol. The MSE values presented by Quinn et al. (2002) were used for

4   calculating scattering coefficient of nss sulfate in PM_1 filters.

6   **2.6 Scattering data from the South Pole**

7   At the South Pole Station (SPO) light scattering coefficient has been measured for more than 40 years. An

8   integrating nephelometer was installed in 1979 and used to measure σ_{sp}, at four wavelengths (450, 550, 700,

9   850 nm). This nephelometer (Meteorology Research Inc. (MRI), Altadena, CA) was used until its failure in 2002,

10   and a TSI Model 3563 3-wavelength nephelometer (λ = 450 nm, 550 nm, and 700 nm) replaced it in November

11   2002. (Sheridan et al., 2016). Running 24-hour averages of σ_{sp}(550 nm) were calculated for the years 2007 –

12   2013 the same way as was done for the Dome C data. The data were used for comparisons with σ_{sp} calculated

13   from the Dome C data.

15   **2.7 Source area analyses**

16   The airmass history and transport of aerosols to Dome C were calculated with the Lagrangian dispersion model

17   FLEXPART (Stohl et al., 2005; Pisso et al, 2019). ECMWF reanalysis meteorology was used to run 60000

18   trajectories every 6 hour 50 days backwards from Dome C to make a statistical sampling of the air measured

19   there. The FLEXPART trajectories follow the mean flow of the atmosphere plus random perturbations to

20   account for turbulence.

22   In backward mode, the FLEXPART output is emission sensitivity S that is proportional to residence time within a

23   grid cell (Stohl et al., 2005; Hirdman et al., 2010; Pisso et al, 2019). Depending on the settings the output unit of

24   FLEXPART in the backward runs, can be s, s m^3 kg^{-1} or s kg m^{-3}. In the present work the unit of S is seconds (s).

25   When coupled with emissions, FLEXPART emission sensitivity creates a concentration at the release point that

26   is equivalent to forward simulations from emissions, except for some small numerical differences (Seibert and

27   Frank, 2004). One advantage of using a backward simulation in a case like this is that the emission sensitivity

28   fields can be used not only to simulate concentrations but also directly to quantitatively describe exactly where

29   the air that reaches Dome C originates, and, thus, potential emissions influences. Emission sensitivity close to

30   the surface – here at levels < 1000 m a.g.l – is often called the footprint (e.g., Hirdman et al. 2010). If a

31   footprint were multiplied with emission mass flux in kg m^{-3} s^{-1} at some grid cell the result would be a

1 concentration due to that emission at the receptor site (Stohl et al., 2005). In the present work this step was

2 not done.

4 To investigate the role of removal processes during transport, for all model runs, two different tracers were

5 used, one atmospheric tracer with no removal and simulated BC particles with a lognormal size distribution

6 (geometric mean diameter = 150 nm, geometric standard deviation 1.5) experiencing both dry and wet

7 deposition. All tracers were run backwards for 50 days, in most cases sufficient for the aerosol tracer to have

8 less than 1e-12 of the emission sensitivity of the inert air tracer, meaning any emission prior to this would have

9 been removed by the time of arrival at Dome C. The wet removal differentiates removal within and below

10 clouds, also considering the water phase of the clouds and the precipitation type. The FLEXPART removal

11 parameters are the efficiency of aerosols to serve as cloud condensation nuclei (CCN_{eff}) and ice nuclei (IN_{eff}).

12 The values used for them were CCN_{eff} = 0.9 and IN_{eff} = 0.1 as in Table 4 of Grythe et al. (2017). The FLEXPART

13 below-cloud scavenging is a scheme based on Laakso et al. (2003) and Kyrö et al. (2009), both described in

14 Grythe et al. (2017). The model includes a realistic distribution of clouds by incorporating three-dimensional

15 cloud information from ECMWF. For a detailed description see Grythe et al. (2017).

17 **2.7.1 Footprint difference calculations**

18 A statistical analysis was applied to differentiate types of air pathways using a method derived from Hirdman et

19 al. (2010). With the main aim to investigate the different pathways to Dome C, each 6hr interval was given a

20 rank in regards to eBC concentration and single-scattering albedo. The emission sensitivity of the 50-day

21 transport for an aerosol tracer was sorted according to its relative type. The emission sensitivities of the

22 highest (S_H) and the lowest (S_L) 10% of eBC concentration and ω_o were calculated by averaging their emission

23 sensitivities for a given grid cell I, j, m by:

$$S_* = \frac{1}{M} \sum_{m=1}^{M} S(i, j, m)$$
(18)

25 Where M is the number of measurements, and S_* can be any of the sorting criteria. The relative difference

26 between two emission sensitivities S_1 and S_2 in % is then calculated as:

$$RD_{1,2}(i, j) = 100\% \frac{S_1(i, j) - S_2(i, j)}{S_1(i, j) + S_2(i, j)}$$
(19)

28 In the calculation the emission sensitivities close to the surface, at < 1000 m a.g.l. were used and so Eq. (19) can

29 be called the relative difference of footprints. This analysis of the footprints can be used to differentiate

1   between different influencing factors on the airmass. This can be either the influence of transport, or removal

2   or combination of these (transport efficiency) or the emission strength.

4   **2.7.2 Emissions used for interpreting the footprint statistics and observed seasonal cycles**

5   The Global Fire Emissions Database (GFED) is a satellite information-based fire activity map. Monthly gridded

6   burned area and emissions from fires are included in the product (http://www.globalfiredata.org). Emitted BC

7   is calculated based on emission factors, which depend on the type of vegetation that is burning. Satellites give

8   snapshots collected to give pseudo global coverage and not continuous coverage. GFED v3.1 is based on the

9   area burned, which is derived by coupling Moderate resolution Imaging Spectroradiometer (MODIS) fire pixel

10   counts with surface reflectance images (Giglio et al., 2006, 2009, 2010). This widely used emission inventory

11   has uncertainties that arrive both from the emission factors and also from the amount of burnt material. A

12   comparison of this bottom-up inventory with top-down inventories found large regional differences, and top-

13   down estimates were about 30% higher (Bond et al., 2013).

15   For the scattering aerosol two sources were considered. An off-line tool (FLEX-SSA) developed by Grythe et al.

16   (2014) and Grythe (2017) to simulate sea spray aerosol (SSA) with FLEXPART was used. It uses inputs from the

17   ECMWF model. These inputs are the wind speed at 10 m above the surface (U10) and the sea surface

18   temperature (SST). The tool takes into account the sea ice fraction which is important to the Southern Ocean

19   SSA emissions. The other major marine scattering aerosols discussed below are biogenic secondary aerosols.

20   Behrenfeld et al. (2017) estimated monthly average phytoplankton biomass (C_{phyto}) concentrations in 2007 –

21   2015 from the Cloud-Aerosol Lidar with Orthogonal Polarization (CALIOP) satellite sensor data in three zones:

22   zone 1 = 45° - 55°S, zone 2 = 55° - 65°S and zone 3 = 65°-75°S. The data provided by Behrenfeld (2021, personal

23   communication) were used for calculating seasonal monthly C_{phyto} averages in the three zones in 2008 – 2013.

24   C_{phyto} can be used as a proxy of biological activity and emissions of dimethyl sulfide (DMS), a precursor of

25   secondary biogenic aerosols.

27   **3. Results and discusion**

28   **3.1 Overview of the data**

29   The time series of σ_{sp} calculated from the size distributions and from the PM_1 and PM_{10} concentrations and the

30   $\sigma_{ap,nsc}$ at Dome C and σ_{sp} measured with the nephelometer at the SPO are presented in Fig. 5. For the DMPS-

31   derived σ_{sp} only the upper estimate, $\sigma_{sp}(DMPS,PM_{10})$, Eq. (8) is shown. The descriptive statistics of aerosol

32   optical properties and mass concentrations in the whole period are presented in Tables 4 and 5.

1   Several observations can be made from the time series in Fig. 5. First, the scattering coefficients calculated

2   from the size distributions and the filter samples follow each other relatively well. There is a clear seasonal

3   cycle of both σ_{sp} and $\sigma_{ap,nsc}$. It is clearly seen that $\sigma_{ap,nsc}$ follows the temporal variations of σ_{sp}(DMPS), the high

4   and low values occur mainly simultaneously which is good, considering that these two AOPs were measured

5   with independent instruments. Since the PSAP and other filter-based absorption photometers are sensitive not

6   only to absorbing but also to scattering aerosol and since Dome C is far from BC sources it is possible that the

7   good correlation is due to the apparent absorption only. Below this will be studied simply by using Eqs. (11) and

8   (12) to account for the scattering artifact on the absorption measurement.

10   The σ_{sp} at Dome C and SPO agree better in austral summer than in winter. However, many high-concentration

11   episodes are observed also in winter almost simultaneous at Dome C and SPO. As an example, a four-month

12   period in May-August 2011 is presented in more detail in Fig. 6. The figure shows 24-hour running averages of

13   σ_{sp}, σ_{ap} and ω_o at λ = 530 nm at Dome C and σ_{sp} at λ = 550 nm at SPO. Fig. 6a shows the upper estimate σ_{sp} =

14   σ_{sp}(DMPS,PM$_{10}$), the corresponding lower estimate of σ_{ap} = $\sigma_{ap}(\sigma_{sp}$(DMPS,PM$_{10}$)) (corrected according to

15   B1999, Eq. 11) and the upper estimate of ω_o. Fig. 6b presents the lower estimate of σ_{sp} = σ_{sp}(DMPS,PM$_{0.8}$), the

16   corresponding upper estimate of σ_{ap} = $\sigma_{ap}(\sigma_{sp}$(DMPS,PM$_{0.8}$)) and the lower estimate of ω_o. In both Fig. 6a and

17   6b also the non-scattering-corrected absorption coefficient $\sigma_{ap,nsc}$ is shown.

19   In Fig. 6a, the period denoted by (1) shows an episode in which ω_o decreases significantly for several days,

20   being an example of long-range-transported eBC. Episodes (2) and (4) are examples of periods when σ_{sp} is

21   approximately an order of magnitude higher at SPO than at Dome C. There are also events such as episode (3)

22   when σ_{sp} is approximately the same at both sites. The peaks often seem to appear slightly earlier at SPO than

23   at Dome C, suggesting transport from SPO to Dome C rather than the other way around. An example of this is

24   shown in the footprint (Fig. 7) calculated for the episode denoted by (3) in Fig. 6. The footprint shows that the

25   air masses came from the direction of the Antarctic peninsula via SPO to Dome C. Air flow from the direction of

26   the Weddell Sea to SPO and then to Dome C is consistent with a very long known winter-time circulation

27   pattern (Alt et al., 1959) as reviewed by Shaw (1979). During the event denoted by episode (3) $\sigma_{ap,nsc}$ was also

28   high. However, when the scattering correction (Eq. 11) was applied the resulting σ_{ap} was not especially high

29   and ω_o was in the range of 0.98 – 1.00 for both the upper and lower estimates of σ_{sp}, which indicates that non-

30   scattering-corrected absorption coefficients may be considerably overestimated when σ_{sp} is high.

1   The scattering coefficients calculated from the size distributions, averaged over the filter sampling periods

2   correlate positively with the scattering coefficients calculated from the PM_1 and PM_{10} filters (Fig. 8). Ordinary

3   least squares regression was used here. The main purpose of the regression was to study whether there is a

4   statistically significant correlation between the scattering coefficients calculated from the size distributions and

5   the filter samples. According to the slopes 0.78 ± 0.02 and 0.76 ± 0.04 of the regression lines in Figd. 8a and 8c

6   σ_{sp}(DMPS, $PM_{0.8}$) seems to be the lower estimate of σ_{sp} also when it is compared with the filter-sample-

7   derived σ_{sp}. According to the slope of 1.29 ± 0.04 in Fig. 8b σ_{sp}(DMPS, PM_{10}) is an upper estimate of σ_{sp}

8   compared with σ_{sp}(PM_{10}) but when σ_{sp}(DMPS, PM_{10}) it is compared with σ_{sp}(PM_1) the slope is 1.01 ± 0.06 which

9   appears to be somewhat controversial. There are also other peculiarities in the scatter plots. The scatter plot of

10   σ_{sp}(DMPS, $PM_{0.8}$) vs. σ_{sp}(PM_{10}) (Fig. 8a) have data points where σ_{sp}(DMPS) is low, in the range of ~0.02 – 0.03

11   Mm^{-1} but σ_{sp}(PM_{10}) varies in a much larger range from ~0.02 to ~0.9 Mm^{-1}. This also occurs when σ_{sp}(DMPS,

12   PM_{10}) is compared with σ_{sp}(PM_{10}) (Fig. 8b). The pattern could be explained by too low values of of both

13   σ_{sp}(DMPS, $PM_{0.8}$) and σ_{sp}(DMPS, PM_{10}) or by too high values of σ_{sp}(PM_{10}). Similar suspicious pattern is not

14   observed in the comparison with the PM_1 filters (Fig. 8c and 8d) suggesting the problem may be with σ_{sp}(PM_{10}).

15   It is clear that this is not a calibration of either the size-distribution-derived or the filter-sample-derived σ_{sp} but

16   the main message of the regressions is that the values are in the same order of magnitude and that there is a

17   statistically significant positive correlation between them which increases confidence in the results. When the

18   regressions are compared with each other it has to be kept in mind that the sampling periods and the number

19   of samples of the PM_1 and PM_{10} data were not the same.

21   Other reasons for the wide scatter of the data points are the mass scattering efficiencies (MSE) used for

22   calculating scattering coefficients from the filter samples (see section 2.5), uncertainties in ion analyses from

23   the filters and uncertainties in calculating scattering coefficient from the size distributions, especially the

24   estimation of σ_{sp}(DMPS,PM_{10}) from size distributions measured with the DMPS only. In spite of all these

25   uncertainties the statistical values (averages and percentiles of the cumulative distributions) of the scattering

26   coefficients are reasonably similar. For instance, the medians of σ_{sp}(PM_{10}, λ=550 nm), σ_{sp}(PM_1, λ=550 nm),

27   σ_{sp}(DMPS, $PM_{0.8}$, λ=530 nm) and σ_{sp}(DMPS, PM_{10}, λ=530 nm), were 0.24 Mm^{-1}, 0.24 Mm^{-1}, 0.15 Mm^{-1}, and 0.23

28   Mm^{-1}, respectively (Table 4). The fact that the medians of σ_{sp}(PM_{10}) and σ_{sp}(PM_1) are the same is somewhat

29   suspicious, it would be expected that σ_{sp}(PM_1) < σ_{sp}(PM_{10}). At this point it is worth paying attention to the

30   statistics of the mass concentrations calculated from the size distributions and from the sum of ions in the filter

31   samples (Table 5). The median mass concentrations of the PM_1 and PM_{10} filters were 66 ng m^{-3} and 126 ng m^{-3},

32   respectively, in the expected order. These mass concentrations are also in reasonably good agreement with

1 median m(DMPS, $PM_{0.8}$) of 70 ng m^{-3} and median m(DMPS, PM_{10}) of 110 ng m^{-3} (Table 5). This suggests that the

2 MSE values used for calculating scattering coefficients from the filter masses were not correct. As it was

3 written in section 2.5 the MSE values were taken from Hand and Malm (2007) who derived them from

4 measurements conducted mainly in US national parks. Considering this, the agreement of the filter-sample-

5 derived with the size-distribution-derived σ_{sp} is reasonable.

3.2 Seasonal cycles of AOPs

3.2.1 Seasonal cycles of scattering and absorption coefficients

9 The seasonal cycles of scattering and absorption coefficients are presented in Fig. 9. The SPO scattering

10 coefficients presented in Fig. 9a-d were measured using the TSI nephelometer and the Dome C scattering

11 coefficients were calculated using the PM_1 (Fig. 9a) and PM_{10} (Fig. 9b) filter sample data as explained in section

12 2.5 and and from the number size distributions (Figs. 9c-d). The maximum and minimum monthly average and

13 median scattering coefficients were observed in austral summer and winter, respectively. At SPO the

14 scattering coefficient was similar to that at Dome C in austral summer but there was a large difference in

15 austral winter. At SPO the maximum monthy average scattering coefficients were observed in austral winter

16 but at Dome C in austral summer. This suggests that in austral winter SPO is more influenced by sea spray

17 emissions than Dome C. However, even though the averages and medians are lower at Dome C high scattering

18 coefficients are also occasionally observed there in austral winter, as is shown by the 95th percentiles in Fig. 9c

19 and 9d and above in the time series of winter 2011 (Fig. 6). The data does not explain the reasons of the

20 difference between Dome C and SPO in austral winter. It may either be due to different geographical locations,

21 different size ranges measured by the instruments or both.

23 A hypothetical explanation for the difference between the scattering coefficients at SPO and Dome C could be

24 that in the very dry conditions the particles are not spherical. It is true that the shape of particles affects light

25 scattering. However, it mainly affects the polarization of scattered light: spherical particles do not change the

26 state of the polarization of scattered light but nonspherical particle do. This is used for example in polarization

27 lidars to discriminate ice crystals, dust particles and droplets. However, integral photometric characteristics,

28 such as extinction, scattering and absorption cross sections and single-scattering albedo do not depend

29 significantly on particle shape as is shown in chapter 10 of the textbook by Mischenko et al. (2002). Therefore

30 nonsphericity is not a likely explanation for the difference.

1   The minimum monthly means and medians of σ_{ap} at Dome C were observed in austral autumn (MAM) and the

2   maximum monthly means and medians in austral spring (SON), which is different than the seasonal cycle of σ_{sp}.

3   (Fig 9e and 9f, Tables S2 and S4). As a result, the seasonal cycle of the single-scattering albedo ω_o is such that

4   the darkest aerosol, i.e., the lowest ω_o is observed in September and October and the highest ω_o in February

5   and March (Fig. 9g and 9h, Table S5). When the lower estimate for σ_{sp} (i.e., σ_{sp}(DMPS, PM$_{0.8}$)) is used for the

6   scattering correction (Eqs. (11) and (12)) the October monthly medians of ω_o are 0.862 and 0.868 when using

7   the B1999 and V2010 algorithms, respectively, and when the upper estimate σ_{sp}(DMPS, PM$_{10}$) is used for the

8   scattering corrections the October monthly medians of ω_o are 0.911 and 0.916 when using the B1999 and

9   V2010 algorithms, respectively (Table S5). The highest monthly median single-scattering albedos are ~0.98 and

10   > 0.99 with both algorithms when using the σ_{sp} lower and upper estimates for the scattering corrections,

11   respectively. These results show that when σ_{sp} is not measured but calculated from the size distributions the

12   σ_{ap} and ω_o are clearly less sensitive to the selection of the algorithm (B1999 or V2010) than to the scattering

13   coefficient used for the scattering correction. But as was noted in section 2.3.4, it is likely that

14   σ_{ap}(σ_{sp}(DMPS,PM$_{10}$)) is closer to the true absorption coefficient than σ_{ap}(σ_{sp}(DMPS,PM$_{0.8}$)) so we can also

15   consider the seasonal cycles presented in Figs. 9d, 9f and 9h to be the closest to the true ones.

17   **3.2.2 Seasonal cycles of scattering and absorption Ångström exponents**

18   The wavelength dependency of both scattering and absorption have clear seasonal cycles. The average

19   scattering Ångström exponent of particles in the DMPS size range, α_{sp}(DMPS,PM$_{0.8}$) varies from ~2.6 in austral

20   summer (DJF) to ~2.1 in austral winter (JJA) indicating that in austral summer the size distributions are

21   dominated by smaller particles than in winter (Fig. 10a, Table S3). This cycle is much clearer, when α_{sp} is

22   calculated from the upper estimate of scattering: average α_{sp}(DMPS,PM$_{10}$) varies from ~1.9 in austral summer

23   to ~0.8 in winter. The seasonal cycle of α_{sp}(DMPS,PM$_{10}$) is actually strikingly similar to the seasonal cycle of α_{sp}

24   of σ_{sp} measured at SPO. This supports the use of the wavelength-dependent formula (Eq. 8) for calculating

25   σ_{sp}(DMPS,PM$_{10}$,λ) from σ_{sp}(DMPS,PM$_{0.8}$,λ). The range of α_{sp} is much larger at SPO than at Dome C, however. The

26   main reason is probably that when σ_{sp}(DMPS,PM$_{10}$,λ) was calculated with Eq. (8) only the monthly averages of

27   fσ_{sp}(DMPS,λ) (Eq. 7) were used but the fσ_{sp}(DMPS,λ) range is actually quite large (Fig. 3). The SPO values were

28   calculated from direct PM$_{10}$ scattering measurements from a nephelometer.

30   The absorption Ångström exponent α_{ap} was calculated for the non-scattering corrected absorption coefficient

31    $\sigma_{ap,nsc}$ and for the scattering-corrected σ_{ap}(σ_{sp}(DMPS,PM$_{10}$)) with the two algorithms. Close to the σ_{ap} detection

32   limit the ratios of σ_{ap} at two wavelengths are very noisy so Fig. 10b, Table 4 and Table S6 present α_{ap} statistics

1   of absorption coefficients for $\sigma_{ap} > 3\times\delta\sigma_{ap}$ where $\delta\sigma_{ap}$ is the wavelength-dependent 24-h average noise at $\lambda =$

2   467 nm and $\lambda = 660$ nm (Table2). Note that the number of accepted data points is lower for the scattering-

3   corrected   than for the non-scattering-corrected α_{ap} (Table 4). The reason is that the scattering correction

4   often decreases σ_{ap} below $3\times\delta\sigma_{ap}$.

6   The first observation that can be made from looking at the statistics (Fig. 10b, Table 4 and Table S6) is that

7     $\alpha_{ap}(\sigma_{sp}(DMPS,PM_{10}),V2010)$ is always larger than $\alpha_{ap}(\sigma_{ap,nsc})$ and $\alpha_{ap}(\sigma_{sp}(DMPS,PM_{10}),B1999)$. The main

8   explanation of this is that the constants in the V2010 algorithm (Eq. 12) depend on wavelength but the B1999

9   algorithm (Eq. 11) uses the same constants for all wavelengths. The differences between the α_{ap} obtained from

10   different algorithms were also discussed by Backman et al. (2014) and Luoma et al. (2021).

12   The seasonal cycles of $\alpha_{ap}(\sigma_{ap,nsc})$ and $\alpha_{ap}(\sigma_{sp}(DMPS,PM_{10}),B1999)$ are qualitatively similar: the lowest medians

13   are observed in March and the maxima in August – October. This cycle is approximately anticorrelated with the

14   ω_o seasonal cycle: in March the median ω_o is the highest and the lowest in August – October. In March the

15   median $\alpha_{ap}(\sigma_{ap,nsc})$ and $\alpha_{ap}(\sigma_{sp}(DMPS,PM_{10}),B1999)$ were ~0.6 and 0.37 and in August-September 0.96 and

16   ~0.92-0.96, respectively (Table S6), essentially the value generally used for pure BC. The seasonal cycle of

17    $\alpha_{ap}(\sigma_{sp}(DMPS,PM_{10}),V2010)$ is a little bit different: the minimum median of ~1.2 is in February and the

18   maximum of ~1.7 occurs in June (Table S6).

20   The interpretation of α_{ap} is complicated. The α_{ap} is related to the dominant absorbing aerosol type but physical

21   properties of the particles also affect it. For externally mixed BC particles it is generally assumed to be around 1

22   (Hegg et al., 2002; Bond and Bergstrom, 2006; Bond et al., 2013) and higher for some organic aerosol from

23   biomass smoke and mineral dust (Kirchstetter et al., 2004; Russell et al., 2010; Devi et al, 2016). However, α_{ap}

24   also depends on the size of BC cores and coating thickness. It is easy to show with Mie models that for single

25   non-coated BC particles with $D_p < $ ~20 nm α_{ap} is indeed close to 1, but when $D_p \approx 100$ nm $\alpha_{ap} \approx 1.3$ depending

26   on the wavelength pair used for the calculation and < 1 when $D_p > $ ~150 nm. For BC particle size distributions

27   the width and the dominant particle size affect α_{ap}. Coating of BC cores affects α_{ap} even more: when BC

28   particles are coated either with a light-absorbing shell or even with a light-scattering shell α_{ap} can be clearly

29   larger than 1 (e.g., Gyawali et al., 2009; Lack and Cappa, 2010; Virkkula, 2021). Core-shell simulations of size

30   distributions of BC particles coated with a light-scattering shell show that $\alpha_{ap} > $ ~1.4 for the wavelength pair of

31   470/950 nm could be obtained for BC particle size distributions when the shell volume fraction is $> $ ~89 – 90%

32   and the geometric mean diameter of the BC particles is in the range of ~70 – 100 nm (Virkkula, 2021). Higher

1   α_{ap} would be obtained also by coating with a light-absorbing shell such as brown carbon. In the present work

2   such α_{ap} values were obtained for $\alpha_{ap}(\sigma_{sp}(DMPS,PM_{10}),V2010)$ for the wavelength pair 467/660 nm. So, if these

3   values are closer to the truth it seems that the BC particles that are observed at Dome C are thickly coated and

4   their dominant particle size is < ~100 nm. On the other hand, if the average α_{ap} ≈ 0.8 obtained for $\alpha_{ap}(\sigma_{ap,nsc})$

5   and $\alpha_{ap}(\sigma_{sp}(DMPS,PM_{10}),B1999)$ is closer to the truth, the core-shell simulation of Virkkula (2021) suggests that

6   BC particle size distributions would dominated by thinly-coated particles in the size range > 100 nm.

8   **3.3 Seasonal cycles of mass concentrations, eBC mass concentrations and mass fractions**

9   The seasonal cycles of the mass concentrations $m(DMPS,PM_{0.8})$ and $m(DMPS,PM_{10})$, see section 2.3.2, the

10   mass concentrations of the PM_1 and PM_{10} filter samples, the mass fraction of the sum of secondary sulfur ions,

11   the eBC mass concentrations and the eBC mass fractions $feBC(m(DMPS,PM_{0.8}))$ and $feBC(m(DMPS,PM_{10}))$ (Eqs.

12   16 and 17) presented in Fig. 11 and in Tables S1, S7, S8, and S9. Some corresponding published Antarctic data

13   are also plotted in Fig. 11 for comparison. The $m(DMPS,PM_{0.8})$ and the $m(PM_1)$ are consistent with each other

14   in that the minimum median mass concentrations are observed in May and June and maximum medians in

15   February. This cycle is very similar to that observed at the Norwegian station Troll in 2007-2011 (Fiebig et al.,

16   2014). The monthly average volume concentrations of particles in the size range 33 − 830 nm in Fig. 9 of Fiebig

17   et al. (2014) were digitized and multiplied by the same particle density ρ = 1.7 g cm^{-3} that was used for the

18   Dome C data and plotted in Fig 11a. The average (± standard deviation) of the ratio $m(DMPS,PM_{0.8},Dome$

19   $C)/m(DMPS,Troll)$ of the monthly averages is ~0.6 ± 0.2, i.e., about 40% lower at Dome C. Fiebig et al. (2014)

20   reasoned that the seasonal cycle of particles in the size range measured by the DMPS, i.e., $m(DMPS)$ is

21   controlled by photo-oxidation-limited aerosol formation. This is obviously true for Dome C also. In February,

22   when the maximum monthly average PM_1 and PM_{10} concentrations were observed also the contribution of the

23   sum of secondary sulfur ions (nss SO_4^{2-} + MSA^-) was the highest (Fig. 11b): the average (± standard deviation)

24   contributions to sum of ions in the PM_1 and PM_{10} filters was then ~81 ± 12% and ~ 61 ± 23%, respectively. The

25   concentrations and the contributions of nss SO_4^{2-} + MSA^- were the lowest in July, ~9 ±5 % and ~ 5 ± 5% for PM_1

26   and PM_{10}, respectively.

28   The seasonal cycle of larger particles ($m(PM_{10})$ and $m(DMPS,PM_{10})$) is much weaker (Fig. 11a) than the $m(PM_1)$

29   and $m(DMPS,PM_{0.8})$ cycle. The explanation is that the contribution of sea salt to aerosol mass is the highest in

30   winter (Fig. 11b) and that a large fraction of sea-salt particles is in the supermicron size range, in line with

31   other studies of aerosols at Dome C (e.g., Jourdain et al., 2008; Udisti et al., 2012; Legrand et al., 2017a,

32   2017b). Note that the seasonal cycle of the mass fraction of secondary sulfur ions is qualitatively similar to the

1   seasonal cycle of the scattering Ångström exponent α_{sp} (Fig. 10a): both have the highest values in the austral

2   summer and the lowest values in the austral winter. This is especially clear for the PM_{10} filters. The small insert

3   in Fig. 11b shows the scatter plot of the monthly average $\alpha_{sp}(DMPS,PM_{10})$ vs. (nss SO_4^{2-} + MSA^-)/PM_{10}. The

4   relationship is essentially linear and the correlation coefficient is high, $r^2 = 0.93$. Since the usual interpretation

5   of the size dependence of α_{sp} is that it is inversely proportional to dominating particle size it indicates that

6   when the mass fraction of secondary aerosol is the highest the dominating particle size is the smallest. As such

7   this is not a surprising observation but it is an additional piece of information that links the chemical

8   composition and aerosol optical properties.

10 The estimated $m(PM_{10})$ values are consistent with the concentrations measured gravimetrically by Annibaldi et

11 al. (2011) in December 2005 – January 2006. The average PM_{10} mass concentration they obtained was 134 ± 12

12 ng m^{-3} at p = 1013 hPa and T = 298 K which equals 146 ± 12 ng m^{-3} at p = 1013 hPa and T = 273 K used in the

13 present paper. The average (and median) PM_{10} mass concentrations in the present work were 167 ng m^{-3} (140

14 ng m^{-3}) and 167 ng m^{-3} (143 ng m^{-3}) in December and January, respectively (Table S1), in a good agreement with

15 the gravimetric measurement of Annibaldi et al. (2011) even though their measurements were not conducted

16 in the same period as ours.

18 In the austral summer the mass concentration calculated from the size distributions ($m(DMPS,PM_{0.8})$ and

19 $m(DMPS,PM_{10})$) were ~100 ng m^{-3} higher than the sums of ions in the PM_1 and PM_{10} filters (Table S1). Part of

20 the explanation could in principle be that the density 1.7 g cm^{-3} used for calculating mass concentrations from

21 the size distibutions was too high but it cannot explain all of it. Another possible explanation is that there were

22 organic compounds not observed with ion chromatography. Caiazzo et al. (2021) took filter samples at Dome C

23 in a different period, December 2016 – January 2018, analyzed them for organic and elemental carbon with an

24 OC/EC analyzer. The average OC concentration was 86 ± 29 ng m^{-3}, approximately the concentration difference

25 between the size distribution-derived and the sums of ions in the filter samples.

27 The eBC concentrations $eBC(\sigma_{ap,nsc})$ and $eBC(\sigma_{sp}(DMPS,PM_{10}))$ were calculated from Eq. (15). For the scattering-

28 corrected σ_{ap} the two algorithms, Eq. (11) ad (12) yielded essentially the same absorption coefficients at λ =

29 530 nm. Therefore only one of them is shown in the seasonal cycle plot in Fig 11c but both are presented in the

30 supplement Table S7. On the other hand, $eBC(\sigma_{ap,nsc})$ is also plotted to show how much the scattering

31 correction affects the calculated eBC concentrations in different seasons. For comparison, published monthly

32 median eBC seasonal cycles at three other Antarctic sites are plotted in Fig 11c: at Neumayer, a coastal site in

1   Queen Maud Land, using two two methods, an Aethalometer and a MAAP (Weller et al., 2013), at Syowa,

2   another Queen Maud Land coastal site using an Aethalometer (Hara et al., 2019), and at SPO using an

3   Aethalometer (Sheridan et al., 2016). The maximum median eBC concentrations are observed in October-

4   November at all sites. The maximum eBC in October-November is ~3 ± 1 ng m^{-3}, quite similar at all sites. For

5   eBC it appears that there is no significant difference between the coastal and plateau sites. The highest

6   monthly median eBC concentrations are those measured with the MAAP at Neumayer in October but, for the

7   same month, the median Aethalometer-derived eBC at Neumayer is the lowest. The lowest monthly median

8   eBC concentrations are observed in April-May at Neumayer, SPO and Dome C and three months earlier in

9   February at Syowa. The lowest monthly medians, ~0.2 ng m^{-3} and ~0.3 ng m^{-3} were observed at Dome C and

10   SPO in May, respectively. The minima were higher at the coastal sites. Note, however, that the eBC

11   concentrations measured with the Aethalometer in Fig. 11c were not corrected for scattering. This correction

12   was done only for the PSAP data from Dome C and automatically for the MAAP data from Neumayer. After the

13   corrections the Dome C monthly median eBC(σ_{sp}(DMPS,PM$_{10}$)) ranged from ~0.2 in May to ~3 ng m^{-3} in

14   October-November, i.e., approximately by an order of magnitude and approximately the same as at SPO. The

15   range is smaller at the coastal sites. This might be due to not correcting for the scattering artifact even though

16   the range of MAAP-derived eBC concentrations at Neumayer is also smaller than on the plateau sites.

18   The seasonal cycle of eBC is somewhat different from that of the mass concentration. Consequently, the

19   minimum eBC mass fractions in both size ranges (feBC(m(DMPS,PM$_{0.8}$) and feBC(m(DMPS,PM$_{10}$)), Eqs. (16) and

20   (17), were in February-March and the maxima in August-October (Fig. 11d, Tables S8 and S9). The eBC mass

21   fractions during this peak were actually quite high. Especially, if it is assumed that all eBC is in the size range

22   measured with the DMPS even for the scattering-corrected eBC monthly medians and averages of feBC varied

23   around 4-5% and the 75th percentiles around 6-7% by using both algorithms (Table S8). These are BC mass

24   fractions typically observed in urban locations (e.g., Liu et al., 2014; Shen et al., 2018), in airborne

25   measurements over Europe (McMeeking et al., 2010) and in biomass burning plumes (Pratt et al., 2011),

26   suggesting that in these periods a large fraction of aerosol was long-range transported aerosol from other

27   continents or highly processed air with larger more scattering aerosol preferentially removed. The highest eBC

28   monthly average and median mass concentrations were observed in November but then feBC was lower than

29   its maximum. This can be explained by the increase of the amount of new, non-absorbing natural secondary

30   particles and condensational growth of BC cores by compounds originating from the sea austral during spring

31   and summer. Järvinen et al. (2013) classified new particle formation (NPF) events observed at Dome C and the

32   highest fraction of new particle formation events was in November while in austral spring the particle growth

rate was also the highest. The minimum feBC monthly averages were < ~0.5% and medians < ~0.3% in February-March (Tables S8 and S9). This minimum occurs simultaneously also with the minimum eBC concentrations. This suggests that during this time of the year the amount of long-range transported aerosol from other continents is at minimum at the same time when the biogenic aerosol production from the oceans is still high.

The seasonal cycles of single-scattering albedo (Fig 9) and eBC mass fraction (Fig. 11d) are anticorrelated with each other. It is logical: the lower the feBC is, the higher is the fraction of scattering aerosol and ω_o. Their relationships can be used for assessing whether their observed seasonal cycles could be explained by internal mixing of BC particles and scattering components. Linear regressions of monthly average and median ω_o vs. feBC yield high correlation coefficients but the regression lines would yield negative values at feBC = 100%. So an exponential function of the form of $\omega_o(feBC) = \omega_o(feBC=0)exp(-k \cdot feBC)$ was fitted with the data (Fig. 12). The correlation coefficients were slightly worse, ~0.89 ± 0.01 for ω_o vs. feBC(m(DMPS,PM$_{0.8}$) (Fig. 12a) than the ~0.98 ± 0.01 for ω_o vs. feBC(m(DMPS,PM$_{10}$) (Fig. 12b). If the fitted exponential functions were valid up to feBC = 100% the ω_o(feBC(m(DMPS,PM$_{0.8}$) would predict that the average $\omega_o \approx 0.2$ and the ω_o(feBC(m(DMPS,PM$_{10}$) would predict that ω_o (feBC=100%) ≈ 0.06. These are reasonable values for pure BC: it has been measured that for fresh pure BC ω_0 is approximately 0.2 ± 0.1 (e.g., Bond and Bergstrom, 2006; Mikhailov et al, 2006; Bond et al., 2013).

To evaluate whether these relationships could be explained by coated spherical BC particles, lognormal size distributions n(D$_p$, GMD, GSD) were generated where GMD is the geometric mean diameter and GSD the geometric standard deviation and D$_p$ range is 3 nm – 10 μm. In the simulations all particles had a BC core and a scattering shell and the core volume fraction was the same for all particles in the size distribution. The core-shell model N-Mie (Voshchinnikov and Mathis, 1999) that is based on a recursive algorithm of Wu and Wang (1991) was used for calculating scattering and absorption efficiencies Q$_s$ and Q$_a$ and scattering and absorption coefficients. See Virkkula (2021) for a detailed description of the simulations.

The BC core volume fraction varied from 0.25 to 4% to cover the range of feBC(m(DMPS,PM10)) shown in Fig. 12b. The simulated ω_o vs. feBC(PM$_{10}$) agrees best with the observation-derived values when GSD = 1.8 and GMD = 200 nm. Smaller GMD and GSD yield lower ω_o vs. feBC(PM$_{10}$). A rigorous error-minimizing procedure was not done since the main goal of this simulation was to show that core-shell geometry can explain the observed ω_o vs. feBC(PM$_{10}$) relationship. However, a deeper analysis of the modal structure of the size

distributions was considered to be out of the scope of the present paper. Note that it was not assumed above that all particles observed at Dome C had a BC core. The simulations did not use any of the measured number concentrations or absorption coefficients. They were pure simulations with generated size distributions and variable BC core and scattering shell volume fractions. They were conducted to study whether the observed ω_o vs. feBC(PM_{10}) relationship could be explained with size distributions of coated BC particles. However, considering that the BC particles observed at Dome C most probably have been transported from the surrounding continents for thousands of kilometers it is very likely that at most of the observed BC particles have been coated during aging processes.

3.4 Aerosol sources and transport and their seasonal cycles

Source areas were modeled by using FLEXPART as described in section 2.7. The 60000 50-day backtrajectories were used for estimating vertical transport routes and the source areas of the observed aerosols. Sources of individual plumes are not analyzed, the main goal is to find explanations of the observed seasonal cycles of aerosol optical properties.

3.4.1 Vertical and horizontal transport

The average residence time of the trajectories in each grid cell in the altitude range 50 – 14400 m a.g.l. south of the Equator is shown for the inert tracer and for the simulated BC aerosol tracer (Fig. 13). The average altitude of both the inert tracer and the BC tracer decreases sharply as the latitude approaches 75°S which shows that on the average air masses descend over the high plateau. This is in line with several studies that show that stratospheric air is brought down into the lower troposphere by descending air masses above the Antarctic continent (Ito, 1989; James, 1989; Parish and Bromwich, 1991; King and Turner, 1997; Krinner and Genthon, 2003; Stohl and Sodemann, 2010). Even though the average altitude of the trajectories shows descending air masses above to Dome C for the inert tracer the low-level residence times are high also at low levels (<1000 m a.g.l.) at latitudes south of about 40°S indicating that it is not uncommon that air masses flow near the surface up to Dome C.

When transport was modeled with FLEXPART using in-cloud and below-cloud scavenging of aged BC particles as described by Grythe et al. (2017), for the BC tracer the residence times are lower than for the inert tracer except near Dome C. Additionally, the average trajectory altitude is clearly different than for the inert tracer. Far from Antarctica the BC tracer residence times are clearly smaller than for the inert tracer. This is due to the removal of BC particles by in-cloud and below-cloud scavenging and dry deposition. As a result there would be

1 essentially no BC particles arriving at Dome C from north of latitude 10°S at altitudes < 1600 m which is

2 indicated by the respective area in Fig. 13b just white. Consequently, those BC particles that do get lifted above

3 the clouds increase the average altitude of the BC tracer backtrajectories compared with the inert tracer

4 average altitude as is shown by the respective black and white lines in Fig 13b. At latitudes ~20°S – 50°S the BC

5 tracer average altitude is approximately 1000 m higher than that of the inert tracer.

7 Between Figs. 13a and 13b there are grey text boxes that show the approximate latitude range of some major

8 BC emitting regions. Indonesia is north of 10°S so BC particles should rise to about 2 km altitude in order to get

9 transported to Dome C. The Indonesian smoke plumes are generally lower than that (Tosca et al., 2011) so its

10 contribution to eBC observed at Dome C is probably negligible. The other three main biomass-burning regions

11 Africa, Australia and Brazil are more to the south and the smoke plume heights have been observed at clearly

12 higher altitudes (Pereira et al., 2016; Rémy et al., 2017; Gonzalez-Alonso et al., 2019). Smoke plumes were

13 recently observed at a height of 4 km over Brazil and even higher, at 6 km over Australia (Shikwambana and

14 Kganyago, 2021) . Comparison with Fig. 13b shows that from these altitudes it is likely that BC particles reach

15 also Dome C. All this is in agreement with Fiebig et al. (2009) who established a source-receptor relationship

16 between biomass burning events in Central Brazil and the aerosol observed at the Norwegian station Troll.

18 Near Dome C and over all continental Antarctica the BC tracer average altitude is lower than that of the inert

19 tracer. When BC has a lower average altitude than tracer it means that the air at that point has undergone

20 more removal above than below the average altitude. This suggests that near Dome C most removal takes

21 place in the clouds, higher up than the release point. This implies that there is more in-cloud removal than

22 precipitation scavenging or dry deposition over the plateau.

24 **3.4.2 Source areas of eBC and high and low ω_o using footprint differences**

25 Source areas were next estimated by using FLEXPART and calculating the footprint differences as described in

26 section 2.7.1. The relative difference (RD) (Eq. 19) of the emission sensitivities in the two lowest layers (<1000

27 m a.g.l.) was calculated for the highest and the lowest 10% of eBC concentration and ω_o. As it was shown in

28 section 3.3 the highest and lowest ω_o percentiles correspond to the lowest and the highest eBC mass fraction

29 percentiles.

30 The highest eBC concentrations have an increased signal from the surrounding continents Australia, Africa and

31 South America (Fig. 14a). However, high RD values are also associated with large areas over the Pacific Ocean,

32 the Indian Ocean and the Atlantic Ocean. These high RD values on the oceans may in principle be due to

shipping emissions but it is more likely that they are due to BC emissions from the continents where the emissions are considerably higher than from shipping. Smoke from South America is predominantly transported southeast into the South Atlantic (Freitas et al., 2005; Reid et al., 2009; Ulke et al., 2011) and further to the east. African smoke gets first transported westward to the Atlantic Ocean by easterly winds (Reid et al., 2009). Most of this smoke wraps around the the South Atlantic Subtropical High, gets mixed with the South American smoke plume and flows east in the subtropical jet region towards Australia and even further to the remote South Pacific (Singh et al., 2000; Staudt et al., 2002; Chatfield et al., 2002). During the transport to higher latitudes the smoke typically rises to about 5 – 7 km (Singh et al., 2000; Staudt et al., 2002; Reid et al., 2009).

In addition to the eastward transport in the subtropical jet smoke outflow associated with the trade winds, i.e., the dominating easterlies from South America towards the west to the Pacific Ocean has been observed between Equator and 20°S (Freitas et al., 2005, Ulke et al., 2011; Bourgeois et al., 2015). Bourgeois et al. (2015) studied aerosol transport over the Andes from the Amazon Basin to the remote Pacific Ocean by using six years (2007–2012) of data from the Cloud-Aerosol Lidar with Orthogonal Polarization (CALIOP) satellite instrument. They found that mainly biomass burning particles emitted during the dry season in the Amazon Basin, are lifted in significant amounts over the Andes. Aerosols reaching the top of the Andes, at altitudes typically between 4 and 5 km, are entrained into the free troposphere (FT) over the southeast Pacific Ocean and they can be traced on average over 4000 km away from the continent indicating an aerosol residence time of 8–9 days in the FT over the Pacific Ocean.

Koch et al. (2009) evaluated BC model predictions of several global models from the AeroCom model intercomparison project. Among several results they presented global maps of modeled BC surface concentrations and annual mean column BC loads predicted by the different models. Fig. 14a displays similarities with both the measurement studies and the global model intercomparison results of Koch et al. (2009). Especially the global maps of annual mean column BC load for GISS sensitivity simulations (Fig. 8 of Koch et al., 2009) have several patterns that are similar to the relative difference RD calculated using Eq. (19) for eBC concentrations measured at Dome C. Here the features of these two figures are compared qualitatively by moving eastwards starting fom Africa. The RD in Fig 14a is high above Africa and on the Atlantic Ocean west of Africa, in agreement with the column BC load predicted by all the GISS sensitivity simulations. To the east, between Africa and Australia there is a belt of high RD values, similar to most of the GISS sensitivity simulations. Interesting is that there is even a local minimum over the Indian Ocean in both the RD values and

1 the GISS simulations. The values over Australia are also high in both figures. There is a clear difference east of

2 Australia: the RD values are high even at the meridian of about 160°W – 180°W although the BC load in most

3 of the GISS simulations decreases clearly immediately to the east of Australia. The RD values then decrease to

4 another local minimum at the meridian of about 150°W and then increase towards South America, in

5 agreement with the GISS sensitivity simulations. Over South America the RD values are positive but decrease to

6 negative values on the South Atlantic immediately to the east of the continent. Such a decrease is not in the

7 GISS sensitivity simulations. So the RD values over the western half of the South Atlantic are the most

8 suspicious ones in Fig. 14a. They suggest that the lowest eBC concentrations observed at Dome C were

9 associated with air masses from there. This is not reasonable since the studies cited above show that South

10 American smoke plumes generally flow to the South Atlantic. This discrepancy remains unexplained.

12 The highest ω_o are obviously related to sea-spray aerosol (SSA) and biogenic secondary aerosol emissions from

13 the Southern Ocean (Fig. 14b). The differences between the oceanic sectors are not big but there some: in the

14 Atlantic and Pacific sectors the RD of ω_o is clearly positive south of latitude 30°S but in the Indian Ocean sector

15 RD is positive south of latitude ~40°S. This can be compared with the Chlorophyll-a (Chl-a) concentrations in

16 five oceanic sectors presented by Becagli et al. (2021). They determined seasonal cycle of Chl-a concentrations

17 in five sectors: Weddell Sea (WS, 60° W–20° E), Indian Ocean (IO, 20–90° E), Western Pacific Ocean (WP, 90–

18 160° E), Ross Sea (RS, 160° E–130° W), and the combined Bellingshausen and Amundsen Seas (BA, 130–60°W).

19 They found that the highest Chl-a concentrations were in the WS, RS and BA sectors and the lowest in the IO

20 and WP sectors. This is in line with the above-described geographical distribution of RD of ω_o in Fig. 14b

21 suggesting that the differences in the RD distributions are due to biogenic aerosols.

23 **3.4.3 Seasonal cycles of air mass transport from different regions**

24 Seasonal cycles of meteorological processes and conditions also affect properties of aerosols observed at Dome

25 C. The most evident is solar radiation that affects new particle formation (e.g., Ito, 1989; Fiebig et al., 2014;

26 Järvinen et al., 2013) but important are also the seasonal cycles of transport from the surrounding continents

27 and from the marine boundary layer of the Southern Ocean (Stohl and Sodemann, 2010). The seasonal

28 contributions of air masses from different regions were calculated as the fraction of time the FLEXPART

29 trajectories spent over Antarctica, the surrounding oceans and continents (Fig. 15).

30 In the austral summer (DJF) the contribution of continental air other than Antarctica is low and its minimum is

31 in April. This is true also for marine air masses other than the Southern Ocean. In summer the contribution of

32 Antarctic air is at the highest. Then in May the air mass transport from other continents increases clearly and it

1 reaches a maximum in July, a smaller fraction in August and a second maximum in September. The seasonal

2 cycle of transport from all the surrounding continental areas is qualitatively similar. It can be explained by the

3 seasonal cycle of the tropospheric polar vortex. Waugh et al. (2017) described the structures, seasonality, and

4 dynamics of the stratospheric and tropospheric polar vortices and their connections to extreme events at

5 Earth's surface. Estimating from their Fig. 2, the approximate edge of the tropospheric polar vortex of the

6 Southern Hemisphere is at the latitudes of 50°S in January and 30°S in July. This means that in the austral

7 winter the southern parts of South America, Africa and Australia are within the tropospheric polar vortex but

8 not in the austral summer. This is in line with Fig. 15. The next question is how well do the seasonal cycles of

9 the aerosol optical properties observed at Dome C follow the emissions of major absorbing and scattering

10 aerosols in different regions.

12 **3.4.4 Relationships of seasonal cycles of BC emissions in the surrounding continents and eBC at Dome C**

13 Monthly BC emissions from wildfires and agricultural burning and other fires in South America, Africa and

14 Oceania (Australia, New Zealand, Melanesia, Micronesia and Polynesia) in 2006-2012 were downloaded from

15 the Global Fire Emissions Database (GFED, V3.1). The seasonal cycles are presented in Fig. 16a together with

16 the monthly average eBC concentrations – corrected for scattering – observed at Dome C. It is obvious in Fig

17 16a that the maximum of the sum of the emissions occurs three months earlier than the maximum eBC

18 concentration at Dome C.

20 The seasonal cycles of air mass residence time over each of the major source areas play a crucial role in

21 explaining the relationship between eBC at DomeC and BC emissions. The BC emissions were multiplied with

22 the fraction of time (=f(t)) the FLEXPART trajectories spent over each of the three major source areas, shown in

23 Fig. 15. These quantities (f(t)×BC emissions) will be called residence-time-weighted BC emissions, RTW BC

24 emissions. They are plotted in Fig. 16b together with the normalized eBC concentrations. Linear regressions

25 between the eBC concentration and RTW BC emissions were calculated but only the respective squared

26 correlation coefficients R^2 are shown. The correlation between eBC concentrations and RTW BC emissions is

27 weak, $R^2 < 0.3$ (Fig. 16b). But the main reason is that the residence times shown in Fig. 15 present the fraction

28 of time that trajectories arriving at Dome C at any given month have spent over each of the regions before

29 arrival at Dome C. So next it was assumed that the transport time from each of the source areas to Dome C is

30 one month so f(t) of each month was multiplied with the BC emission one month earlier. This shifts the RTW BC

31 emission peaks of all the source areas so that all R^2 increase somewhat (Fig. 16c). When it is assumed that the

32 transport time is 2 months R^2 increase clearly, 0.688 for Oceania and 0.665 for South America, for Africa

correlation still remains low (Fig. 16d). In October-November, when the eBC concentrations at Dome C are the largest the 2-month-shifted RTW BC emissions from South America are approximately an order of magnitude larger than from Africa and Oceania suggesting that South American BC emissions are the largest contributor to eBC at Dome C.

The highest correlation between the eBC concentrations and RTW BC emissions with the 2-month time shift suggests further that transport time is considerably longer than the 30 days Stohl and Sodemann (2010) obtained in a 5.5-year climatology of atmospheric transport into the Antarctic troposphere. The two-month transport time naturally implies that BC aerosol residence time is also so long. Williams et al. (2002) estimated by modeling that in the upper atmosphere aerosols of 0.065 μm in size have residence times of approximately 1 month and can be transported on a hemispheric scale. Papastefanou (2006) determined residence times of tropospheric aerosols with different methods and obtained a much shorter mean value of 8 days. Kristiansen et al. (2012) estimated accumulation-mode aerosol removal times from the atmosphere using a global measurement data set collected over several months after the accident at the Fukushima Dai-ichi nuclear power plant in March 2011. After correction for radioactive decay, the $^{137}Cs/^{133}Xe$ ratios can be assumed to reflect the removal of aerosols by wet and dry deposition. Using this method Kristiansen et al. (2012) obtained removal times for ^{137}Cs of 10.0–13.9 days. The simulations of Croft et al. (2014) with instantaneous injections into layers at 5 km and 7 km yielded mean lifetimes of 14.7 days and 21.1 days, respectively. At higher altitudes removal mechanisms are weaker so lifetimes are longer. These are altitudes where biomass-burning smoke plumes have been observed, as discussed above. Note that these lifetimes are the e-folding lifetimes τ from $C(t) = C(t_0)exp(-t/τ)$. That means, for example, that if biomass burning smoke where BC concentration is 1000 ng m^{-3} – similar to concentrations observed in a Brazilian biomass burning measurement campaign (Brito et al., 2014) – rises to 5 km and gets transported for 60 days the BC concentration decreases to 16.9 ng m^{-3}. With τ = 10 d the concentration would decrease to 2.5 ng m^{-3}. At Dome C the 25th to 75th percentile range of eBC concentration in November is ~2 – 6 ng m^{-3} (Table S7). As the simple estimation shows this range is consistent with BC emissions of about 1 μg m^{-3} and transport for two months.

The above discussion does not mean that pollution episodes from the surrounding continents could not be transported faster than in two months. For instance, Fiebig et al. (2009) calculated the source areas and transport routes of an elevated aerosol concentration event observed at the Norwegian Troll station in Queen Maud Land. The analysis showed that the origin of the aerosol was biomass burning in Brazil 11 – 12 days before the arrival at Troll. Hara et al. (2010) analyzed several haze events observed at Syowa, the Japanese

1   Antarctic coastal station. They found that the traveling time from Southern Africa to Syowa varied in the range

2   of 4 to 8 days, even faster than to Troll in the episode analyzed by Fiebig et al. (2009). The explanation for the

3   considerably longer transport time to Dome C, 2 months, is that it was obtained from the correlation of

4   seasonal cycles of BC emissions and observed concentrations so it is more like a statistical estimate of seasonal

5   transport times. That suggests that on the average the BC emitted in the biomass burning in the surrounding

6   continents circulates the Southern Hemisphere and migrates slowly towards the Antarctic upper plateau.

8   Fig. 16 also shows that the observed concentration varies by an order of magnitude only although the

9   emissions vary by two orders of magnitude. This suggests that at the observed seasonal minimum eBC in

10   March-April the sources are something else than wildfires and agricultural burning BC emissions in the GFED

11   data. Possible sources can be other anthropogenic emissions such as traffic including shipping, industrial

12   emissions and heating. Stohl and Sodemann (2010) estimated that ship emissions south of 60°S account for

13   half of the total BC concentrations in the lowest 1000 m of the atmosphere south of 70°S in December.

14   However, due to the particle removal processes as described in section 3.4.1 the contribution of ship emissions

15   to BC at Dome C much lower. No quantitative estimations were calculated. Xu et al. (2021) recently presented

16   a new global BC emission inventory for all countries in the world for the years 1960 – 2017. In an Excel file

17   supplement Xu et al. (2021) presents the emissions classified into energy sector, industrial, residential, on-road

18   motor vehicles, other anthropogenic and wildfires. The sums of South American, Southern hemispheric African

19   and Oceanian emissions in the period 2008 – 2013 and the respective contributions of wildfire emissions were

20   calculated. They were ~40 ± 8 %, ~49 ± 2 % and ~59 ± 9 % for South American, Southern hemispheric African

21   and Oceanian emissions, respectively. However, only wildfire-emitted BC-particles have the potential to rise

22   high enough to avoid in-cloud or below-cloud scavenging during the transport, as was discussed above.

24   **3.4.5 Relationships of seasonal cycles of scattering aerosol emissions and σ_{sp} at Dome C and SPO**

25   The seasonal cycles of scattering coefficient at Dome C and at the SPO were compared with the seasonal cycles

26   of secondary and primary marine aerosol emissions. The sea-spray aerosol (SSA) emissions calculated with the

27   FLEX-SSA offline tool (section 2.7.2) show that SSA emissions from the Southern Ocean peak in the austral

28   winter (Fig. 17a). Sea ice and the glacier surfaces especially in the coastal regions are also important sources of

29   sea-salt aerosols (e.g., Frey et al., 2020; Hara et al., 2020). However, the aim was to find a qualitative

30   explanation of the high scattering coefficients observed in winter especially at SPO. The FLEX-SSA offline tool

31   was used for that and it yields a seasonal cycle that at at least partially explains the observations. There was no

32   tool for estimating seasonal cycles of sea-salt emissions from sea ice.

Secondary marine aerosols are formed from the oxidation of emission products of phytoplankton. Becagli et al. (2021) discussed the relationships between biogenic aerosols (nss SO_4^{2-} and MSA^-), Chlorophyll-a concentration which is a proxy for phytoplankton, sea ice extent and area, source areas and the transport routes to Dome C and the Southern Annular Mode (SAM). They showed that these relationships are different in early, middle, and late austral summer. Here a subset of the data is analyzed in a method that is complementary to that of Becagli et al. (2021). The phytoplankton concentration maximum is in summer and minimum in winter in the satellite data analysis of Behrenfeld et al. (2016) (Fig. 17a). However, phytoplankton concentration alone does not explain the seasonal cycle of secondary aerosol scattering coefficient. The DMS oxidation is a photochemical process so a simplified method was used for estimating solar radiation intensity. Global radiation intensity I_T (W m^{-2}) was calculated by using a clear sky model for direct and diffuse insolation (Bird and Hulstrom, 1981). I_T was calculated at the surface (p =1000 mbar) for each hour of the year at the prime meridian (0°) at three latitudes: 50°S, 60°S, and 70°S corresponding to the central latitudes of zone 1 (45°-55°S), zone 2 (55°-65°S), and the polar zone, zone 3 (65°-75°S). The monthly averages of I_T at 10:00 – 14:00 in each day of a month were calculated. The reasoning for using this time is that new particle formation is typically, although not exclusively, a daytime phenomenon at numerous locations around the world, also in Antarctica (e.g., Weller et al., 2015; Kerminen et al., 2018; Kim et al., 2019; Brean et al, 2021). The monthly product $C_{phyto}I_T$, was then used as a proxy of biogenic secondary aerosol emissions. Behrenfeld et al. (2016) also presented the photosynthetically active radiation (PAR) in the polar zone obtained from the MODIS Aqua ocean colour sensor acquired from http://oceancolor.gsfc.nasa.gov/cms. In addItion to the product $C_{phyto}I_T$, also the monthly product $C_{phyto}PAR$ was calculated for the zone 3 and used as a proxy for biogenic secondary aerosol emissions. In Zone 3 the two emission proxies $C_{phyto}I_T$ and $C_{phyto}PAR$ agree well (Fig. 17a).

The normalized seasonal cycles of the SSA flux and the secondary aerosol emission proxy $C_{phyto}PAR$ in the polar zone are plotted together with the normalized seasonal cycles of the scattering coefficients at Dome C (Fig. 17b) and at SPO (Fig. 17c). At Dome C both $\sigma_{sp}(DMPS,PM_{0.8})$ and $\sigma_{sp}(DMPS,PM_{10})$ approximately follow the seasonal cycle of the secondary aerosol emissions in October – April. In the austral winter the effect of SSA is visible especially in the high monthly σ_{sp} averages. The medians are cleary lower, they follow the secondary aerosol emission proxy even in May. Also the normalized seasonal cycle of $\sigma_{sp}(nss-SO_4^{2-},PM_1)$, the scattering coefficient calculated from non-seasalt sulfate concentrations in PM_1 filter samples is presented in Fig. 17b. It also follows approximately the seasonal cycle of $C_{phyto}PAR$ for the whole year. However, there appears to be a time lag. $C_{phyto}PAR$ grows fast in October but $\sigma_{sp}(nss-SO_4^{2-},PM_1)$ in November. When $C_{phyto}PAR$ is shifted by one month they agree clearly better. The linear regression of of $\sigma_{sp}(nssSO_4^{2-},PM_1)$ vs. $C_{phyto}PAR$ yields the correlation

1   coefficient $R^2 = 0.65$ when there is no $C_{phyto}PAR$ time shift and $R^2 = 0.92$ when $C_{phyto}PAR$ is shifted by one month

2   (Fig. 18). This suggests that on the average it takes approximately a month for the secondary aerosol to be

3   formed, grown, get mixed in the upper atmospheric layers and be transported to the upper plateau. As it was

4   discussed above, Williams et al. (2002) estimated by modeling that in the upper atmosphere aerosol residence

5   time can be ~1 month and Croft et al. (2014) obtained e-folding lifetimes would be ~15 days and ~21 days at 5

6   km and 7 km altitudes, respectively, so it is reasonable.

8   There is one thing that the time shift cannot explain. The maximum σ_{sp} – and mass concentrations as discussed

9   in Section 3.3 – was in February. This cannot be explained by the seasonal cycle of the biogenic secondary

10   aerosol emission proxy: the maximum $C_{phyto}PAR$ was in December so even a one month transport time does not

11   make February the maximum. Above it was assumed that the proxy is simply the product $C_{phyto}PAR$. However,

12   the underlying hypothesis of this proxy is that the emissions of the precursor gases of new particle formation,

13   mainly DMS, are linearly related to the phytoplankton mass concentrations. This is probably not the case, there

14   are other factors. Another explanation could be meteorological. Becagli et al. (2021) showed that the MSA and

15   nss-SO_4^{2-} maxima in February could possibly be explained by faster transport from the surrounding oceans with

16   air masses traveling at lower elevation than in December-January. Further analyses of that relationship are out

17   of the scope of the present paper, however. For more details, see Becagli et al. (2021). Note that σ_{sp}(nssSO_4^{2-},

18   PM_1) correlates well also with $C_{phyto}I_T$ of zones 1 and 2 shown in Fig. 17a which means the secondary marine

19   aerosol may have been formed and grown also further to the north than in the polar zone.

21   At SPO σ_{sp} is more strongly affected by the SSA emissions than at Dome C, especially in the austral winter and

22   spring (Fig. 17c). Note that at SPO the seasonal cycle of the normalized median σ_{sp} follows roughly the

23   normalized SSA emission flux in July – December. The seasonal cycle of the normalized average σ_{sp} is different

24   because averages are affected more by individual high transport events and medians represent better the

25   prevailing background aerosol of the season. As explained above, the difference between Dome C and SPO may

26   either be due to geographical locations, different size ranges measured by the instruments or both.

27   **4. Summary and conclusions**

28   Aerosol optical properties have been measured at several Antarctic sites but scattering and absorption data

29   measured at Dome C have not been not examined in detail earlier. This work fills that gap using light

30   absorption from a 3λ PSAP and light scattering coefficients (σ_{sp}) calculated from particle number size

31   distributions measured with a Differential Mobility Particle Sizer (DMPS) and an optical particle counter (OPC).

32   Additionally, single scattering albedo (ω_o), absorption Ångström exponent (α_{ap}), scattering Ångström exponent

1 (α_{sp}) and equivalent black carbon (eBC) concentrations were calculated. The sources of the aerosol were

2 estimated by calculating footprints with FLEXPART and by calculating seasonal cycles of transport of both

3 scattering and absorbing particles from different source areas.

5 Aerosol light scattering coefficient was calculated from the DMPS size distributions using two different

6 refractive indices and the contribution of scattering due to particles larger than those measured with the DMPS

7 to provide a lower and upper estimate of σ_{sp}. Light scattering was also estimated using mass scattering

8 efficiencies in conjunction with mass concentrations obtained from PM_1 and PM_{10} filter samples. The two most

9 frequently used algorithms to calculate aerosol absorption coefficients (σ_{ap}) from PSAP measurements require

10 scattering coefficients. Both algorithms were applied and both the upper and lower estimate of σ_{sp} were used

11 in order to provide understanding of the differences between the algorithms and the impact of the scattering

12 adjustment. The absorption coefficient calculated using the σ_{sp} upper estimate was considered to be the best

13 σ_{ap} estimate.

15 There were clear seasonal cycles of σ_{sp} and σ_{ap} at Dome C. The maximum and minimum of σ_{sp} were observed in

16 austral summer and winter, respectively. The Dome C scattering coefficients were also compared with σ_{sp}

17 measured with a nephelometer at the South Pole (SPO). At SPO the scattering coefficient was similar to that

18 measured at Dome C in austral summer but there was a large difference in the austral winter. At SPO the

19 maximum monthly averages were observed in austral winter. This suggests that, in winter, SPO is more

20 influenced by sea spray emissions than Dome C. At Dome C the σ_{ap} exhibited a different seasonal cycle of than

21 σ_{sp}– the minimum σ_{ap} was observed in the austral autumn and the maximum in spring. As a result the

22 seasonal cycle of the single-scattering albedo ω_o is such that the darkest aerosol, i.e., the lowest $\omega_o \approx 0.91$ is

23 observed October and the highest $\omega_o > 0.99$ in February and March.

25 The scattering Ångström exponent α_{sp} calculated from the σ_{sp} lower estimate varied from ~2.6 in austral

26 summer to ~2.1 in austral winter indicating that in austral summer the size distributions are dominated by

27 smaller particles than in winter. For the σ_{sp} upper estimate α_{sp} varied from ~1.9 in austral summer to ~0.8 in

28 winter. This seasonal cycle is quite similar to the seasonal cycle of α_{sp} of σ_{sp} measured at SPO. The uncertainty

29 of the absorption Ångström exponent α_{ap} is high, particularly in the clean conditions existing in Antarctica.

30 However, despite the high uncertainties the seasonal cycles of α_{ap}, with and without the scattering correction,

31 are qualitatively similar: the lowest monthly medians are observed in March while the maxima occur in August

1 – October. This cycle – even that of the non-scattering corrected α_{ap} – is anticorrelated with the ω_o seasonal

2 cycle.

4 The eBC mass concentrations were compared with eBC measured at three other sites: the South Pole and two

5 coastal sites Neumayer and Syowa. The maximum monthly median eBC concentrations are almost the same

6 ($\sim 3 \pm 1$ ng m^{-3}) at all these sites in October-November. This suggests that, as far as eBC is concerned, there is no

7 significant difference between the coastal and plateau sites. The seasonal cycle of eBC is slightly different from

8 the mass concentration calculated from the number size distributions measured with the DMPS. Consequently,

9 the seasonal cycle of the eBC mass fraction (f(eBC)) is such that f(eBC) minimum is in February-March and the

10 maximum is in August-October, anticorrelating with ω_o. The eBC mass fractions in this peak are actually quite

11 high and vary around 4-5% with the 75th percentiles > 6-7%, only slightly depending on PSAP correction

12 algorithm. These levels of eBC mass fractions are typically observed in polluted air, suggesting that in these

13 periods a large fraction of aerosol is long-range transported aerosol from other continents.

15 Source areas were calculated with 50-day FLEXPART footprints. The relative differences of the footprints

16 calculated for the highest and lowest 10% of eBC concentrations and ω_o showed that the highest eBC

17 concentrations and the lowest ω_o were associated with air masses coming from South America, Australia and

18 Africa. Vertical simulations that take BC particle removal processes into account show that there would be

19 essentially no BC particles arriving at Dome C from north of latitude 10°S at altitudes < 1600 m. The main

20 biomass-burning regions Africa, Australia and Brazil are more to the south and their smoke plumes have been

21 observed at higher altitudes than that so they can get transported to Antarctica.

23 The seasonal cycle of BC emissions from wildfires and agricultural burning and other fires in South America,

24 Africa and Australia were calculated from data downloaded from the Global Fire Emissions Database (GFED).

25 The maximum total emissions were in August-September but the peak of monthly average eBC concentrations

26 is observed November, 2 – 3 months later not only at Dome C but also at the South Pole and the coastal

27 stations. This is considerably longer than the 30 days presented in an earlier study. If this peak eBC

28 concentration is really due to the peak emissions from the above-mentioned fires in the surrounding

29 continents it means that the aerosol from these fires remains in air for several months and gets mixed

30 essentially over the entire Southern Hemisphere. This does not mean that pollution episodes from the

31 surrounding continents could not be transported faster than in two months. Earlier studies have clearly shown

32 that biomass-burning smoke can get transported frm South America or Africa to Antarctica in 1 – 2 weeks. The

explanation for the considerably longer transport time to Dome C, 2 months, is that it was obtained from the correlation of seasonal cycles of BC emissions and observed concentrations so it is more like a statistical estimate of seasonal transport times. That suggests that on the average the BC emitted in the biomass burning in the surrounding continents circulates the Southern Hemisphere and migrates slowly towards the Antarctic upper plateau.

The seasonal contributions of air masses from different regions were calculated as the fraction of time the FLEXPART trajectories spent over Antarctica, the surrounding oceans and continents. The BC emissions were multiplied with the fraction of time the trajectories spent over each of the three major source areas. In October-November, when the eBC concentrations at Dome C are the largest the 2-month-shifted residence-time-weighted BC emissions from South America are approximately an order of magnitude larger than from Africa and Oceania suggesting that South American BC emissions are the largest contributor to eBC at Dome C.

The seasonal cycles of scattering coefficient at Dome C and at the SPO were compared with the seasonal cycles of secondary and primary marine aerosol emissions. The seasonal cycles of sea spray aerosol (SSA) emissions were simulated with the FLEX-SSA offline tool. The seasonal cycles of biogenic secondary aerosols were estimated from monthly average phytoplankton biomass concentrations obtained from the CALIOP satellite sensor data. The correlation coefficients between scattering coefficients measured at Dome C and phytoplankton biomass concentrations and a biogenic secondary aerosol emission proxy are high. It may take a month for the biogenic aerosol to be formed and get transported from the sea level to Dome C. The scattering coefficients measured at SPO correlated much better with the SSA emission fluxes in the Southern Ocean than the scattering coefficients measured at Dome C. The difference between the scattering coefficients at these sites may either be due to geographical locations, different size ranges measured by the instruments or both.

Data Availability

The Dome C aerosol physical measurement data will be made openly available for the final publication at the EBAS database (http://ebas.nilu.no). The SPO data are there already. The Dome C aerosol chemical composition data will be available upon request by writing to RT, BS or MS.

Author contributions

AV contributed to designing the measurements of aerosol physical properties at Dome C, processing and analyzing data and writing most of the manuscript with contributions from all coauthors; HG did all the

FLEXPART modeling and processed GFED data and wrote the associated text; JB wrote the codes for data processing; TP reviewed and commented the manuscript; MB, CL and AL were responsible for the installation and long-term operation of the aerosol instruments at Dome C; SB, RT, and MS were responsible for the sampling and analyses of the PM1 and PM10 filter samples; VV contributed to designing and administration of the measurements at Dome C; PS and EA were responsible for the SPO aerosol measurements. All authors reviewed and commented the manuscript.

Competing interests

Tuukka Petäjä is editor of ACP.

Financial support

AV was funded by the Academy of Finland project Antarctic Climate Forcing Aerosol (ACFA) (decision nr. 335845) and by the Business Finland project Black Carbon Footprint (BCF) (grant nr. 528/31/2019). HG was supported by NILU's internal financing for publications (G-106057). Aerosol sampling at Dome C was carried out in the framework of the Air-Glacs1181 'Station Concordia' project, which was funded by the MIUR through the Italian 'Programma Nazionale di Ricerche in Antartide' (PNRA) and in the framework of 'DECA-POL' (2010/A3.05) PNRA project. EA was funded by the NOAA Climate Program Office and PS by NOAA base funds.

Acknowledgments

The field operations benefitted from the support of the French-Italian Concordia Station. Meteorological data and information were obtained from IPEV/PNRA Project ''Routine Meteorological Observation at Station Concordia, www.climantartide.it. The technicians at SPO are acknowledged for operating the instruments and Derek Hageman for data processing. Prof. Michael J. Behrenfeld of Oregon State University is acknowledged for providing the phytoplankton biomass concentrations from the CALIOP satellite sensor and the photosynthetically active radiation data from the MODIS Aqua ocean colour sensor.

References

Alt, J., P. Astapenko, and N.J. Ropar, Jr.: Some aspects of the antarctic atmospheric circulation in 1958, IGY Rep. 4, 113 pp., Nat. Acad. of Sci., Washington, D.C., 1959.

Annibaldi, A., Truzzi, C., Illuminati, S., Scarponi, G.: Direct gravimetric determination of aerosol mass concentration in central Antarctica. Anal. Chem., 83, 143-151, doi:10.1021/AC202408Z, 2011.

Backman, J., Virkkula, A., Vakkari, V., Beukes, J. P., Van Zyl, P. G., Josipovic, M., Piketh, S., Tiitta, P., Chiloane, K., Petäjä, T., Kulmala, M., and Laakso, L.: Differences in aerosol absorption Ångström exponents between correction algorithms for a particle soot absorption photometer measured on the South African Highveld, Atmos. Meas. Tech., 7, 4285–4298, https://doi.org/10.5194/amt-7-4285-2014, 2014.

Barber, P. W. and Hill, S. C.: Light scattering by particles: Computational methods, World Scientific Publishing, Singapore, 1990.

Becagli, S., Ghedini, C., Peeters, S., Rottiers, A., Traversi, R., Udisti, R., Chiari, M., Jalba, A., Despiau, S., Dayan, U., Temara, A.: MBAS (Methylene Blue Active Substances) and LAS (Linear Alkylbenzene Sulphonates) in Mediterranean coastal aerosols: sources and transport processes. Atmos. Environ., 45, 6788–6801, doi:10.1016/j.atmosenv.2011.04.041, 2011.

Becagli, S., Scarchilli, C., Traversi, R., Dayan, U., Severi, M., Frosini, D., Vitale, V., Mazzola, M., Lupi, A., Nava, S., and Udisti, R.: Study of present-day sources and transport processes affecting oxidised sulphur compounds in atmospheric aerosols at Dome C (Antarctica) from year-round sampling campaigns, Atmos. Environ., 52, 98–108, 2012.

Becagli, S., Marchese, C., Caiazzo, L., Ciardini, V., Lazzara, L., Mori, G., Nuccio, C., Scarchilli, C., Severi, M., and Traversi, R.: Biogenic aerosol in central East Antarctic Plateau as a proxy for the ocean-atmosphere interaction in the Southern Ocean. Science of The Total Environment, 151285, https://doi.org/10.1016/j.scitotenv.2021.151285, 2021.

Behrenfeld, M. J., Hu, Y., O'Malley, R. T., Boss, E. S., Hostetler, C. A., Siegel, D. A., Sarmiento, J. L., Schulien, J., Hair, J. W., Lu, X., Rodier, S., and Scarino, A. J.: Annual boom-bust cycles of polar phytoplankton biomass revealed by space-based lidar, Nat. Geosci., 10, 118–122, https://doi.org/10.1038/ngeo2861, 2017.

Bird, R. E. and Hulstrom, R. L., Simplified clear sky model for direct and diffuse insolation on horizontal surfaces, SERI/TR-642-761, 1981.

Bond, T. C., Anderson, T. L., and Campbell, D.: Calibration and Intercomparison of Filter-Based Measurements of Visible Light Absorption by Aerosols, Aerosol Sci. Tech., 30, 582–600, https://doi.org/10.1080/027868299304435, 1999.

Bond, T. C. and Bergstrom, R. W.: Light Absorption by Carbonaceous Particles: An Investigative Review, Aerosol Sci. Technol., 40, 27–67, 2006.

Bond, T. C., Doherty, S. J., Fahey, D. W., Forster, P. M., Berntsen, T., DeAngelo, B. J., Flanner, M. G., Ghan, S., Kärcher, B., Koch, D., Kinne, S., Kondo, Y., Quinn, P. K., Sarofim, M. C., Schultz, M. G., Schulz, M., Venkataraman, C., Zhang, H., Zhang, S., Bellouin, N., Guttikunda, S. K., Hopke, P. K., Jacobson, M. Z., Kaiser, J. W., Klimont, Z., Lohmann, U., Schwarz, J. P., Shindell, D., Storelvmo, T., Warren, S. G., and Zender, C. S.: Bounding the role of black carbon in the climate system: A scientific assessment, J. Geophys. Res., 118, 5380–5552, doi:10.1002/jgrd.50171, 2013.

Bourgeois, Q., Ekman, A. M. L., and Krejci, R.: Aerosol transport over the Andes from the Amazon Basin to the remote Pacific Ocean: A multiyear CALIOP assessment, J. Geophys. Res., 120, 8411–8425, https://doi.org/10.1002/2015JD023254, 2015.

Brean, J., Dall'Osto, M., Simó, R., Shi, Z., Beddows, D.C.S, and Harrison, R.: Open ocean and coastal new particle formation from sulfuric acid and amines around the Antarctic Peninsula. Nat. Geosci. https://doi.org/10.1038/s41561-021-00751-y. 2021.

Brito, J., Rizzo, L. V., Morgan, W. T., Coe, H., Johnson, B., Haywood, J., Longo, K., Freitas, S., Andreae, M. O., and Artaxo, P.: Ground-based aerosol characterization during the South American Biomass Burning Analysis (SAMBBA) field experiment, Atmos. Chem. Phys., 14, 12069–12083, https://doi.org/10.5194/acp-14-12069-2014, 2014.

Caiazzo, L., Calzolai, G., Becagli, S., Severi, M., Amore, A., Nardin, R., Chiari, M., Giardi, F., Nava, S., Lucarelli, F., Pazzi, G., Cristofanelli, P., Virkkula, A., Gambaro, A., Barbaro, E., Traversi, R.: Carbonaceous Aerosol in Polar

Areas: First Results and Improvements of the Sampling Strategies. Atmosphere 2021, 12, 320. https://doi.org/10.3390/atmos12030320, 2021.

Chatfield, R., Guo, Z., Sachse, G., Blake, D., and Blake, N.: The subtropical global plume in the Pacific Exploratory Mission Tropics A (PEM-Tropics A), PEM-Tropics B, and the Global Atmospheric Sampling Program (GASP): How tropical emissions affect the remote Pacific, J. Geophys. Res., 107(D16), doi:10.1029/2001JD000497, 2002.

Chen, X., Virkkula, A., Kerminen, V.-M., Manninen, H. E., Busetto, M., Lanconelli, C., Lupi, A., Vitale, V., Del Guasta, M., Grigioni, P., Väänänen, R., Duplissy, E.-M., Petäjä, T., and Kulmala, M.: Features in air ions measured by an air ion spectrometer (AIS) at Dome C, Atmos. Chem. Phys., 17, 13783–13800, https://doi.org/10.5194/acp-17-13783-2017, 2017.

Croft, B., Pierce, J. R., and Martin, R. V.: Interpreting aerosol lifetimes using the GEOS-Chem model and constraints from radionuclide measurements, Atmos. Chem. Phys., 14, 4313–4325, https://doi.org/10.5194/acp-14-4313-2014, 2014.

CSN EN 12341 European Standard: Ambient air–- Standard gravimetric measurement method for the determination of the PM10 or PM2,5 mass concentration of suspended particulate matter, https://www.en-standard.eu/csn-en-12341-ambient-air-standard-gravimetric-measurement-method-for-the-determination-of-the-pm10-or-pm2-5-mass-concentration-of-suspended-particulate-matter/

Devi, J. J., Bergin, M. H., Mckenzie, M., Schauer, J. J., and Weber, R. J.: Contribution of particulate brown carbon to light absorption in the rural and urban Southeast US. Atmospheric Environment, 136, 95-104, 2016.

Fiebig, M., Lunder, C. R., and Stohl, A.: Tracing biomass burning aerosol from South America to Troll Research Station, Antarctica, Geophys. Res. Lett., 36, L14815, doi:10.1029/2009GL038531, 2009.

Fiebig, M., Hirdman, D., Lunder, C. R., Ogren, J. A., Solberg, S., Stohl, A., and Thompson, R. L.: Annual cycle of Antarctic baseline aerosol: controlled by photooxidation-limited aerosol formation, Atmos. Chem. Phys., 14, 3083–3093, https://doi.org/10.5194/acp-14-3083-2014, 2014.

1 Freitas, S. R., Longo, K. M., Silva Dias, M., Silva Dias, P., Chatfield, R., Prins, E., Artaxo, P., Grell, G., and Recuero,

2 F.: Monitoring the transport of biomass burning emissions in South America, Environmental Fluid Mechanics,

3 doi:10.1007/s10652-005-0243-7, 5(1–2), 135–167, 2005.

5 Frey, M. M., Norris, S. J., Brooks, I. M., Anderson, P. S., Nishimura, K., Yang, X., Jones, A. E., Nerentorp

6 Mastromonaco, M. G., Jones, D. H., and Wolff, E. W.: First direct observation of sea salt aerosol production

7 from blowing snow above sea ice, Atmos. Chem. Phys., 20, 2549–2578, https://doi.org/10.5194/acp-20-2549-

8 2020, 2020.

10 Giglio, L., I. Csiszar, and C. O. Justice : Global distribution and seasonality of active fires as observed with the

11 Terra and Aqua Moderate Resolution Imaging Spectroradiometer (MODIS) sensors, J. Geophys. Res.,111,

12 G02016,doi:10.1029/2005JG000142, 2006.

14 Giglio, L., Loboda, T., Roy, D. P., Quayle, B., and Justice, C. O.: An active-fire based burned area mapping

15 algorithm for the MODIS sensor, Remote. Sens. Environ., 113, 408-420, doi:10.1016/j.rse.2008.10.006, 2009.

17 Giglio, L., Randerson, J. T., van der Werf, G. R., Kasibhatla, P. S., Collatz, G. J., Morton, D. C., and DeFries, R. S.:

18 Assessing variability and long-term trends in burned area by merging multiple satellite fire products,

19 Biogeosciences, 7, 1171–1186, doi:10.5194/bg-7-1171-2010, 2010.

21 Gonzalez-Alonso, L., Val Martin, M., and Kahn, R. A.: Biomass-burning smoke heights over the Amazon

22 observed from space, Atmos. Chem. Phys., 19, 1685–1702, https://doi.org/10.5194/acp-19-1685-2019, 2019.

24 Grythe, H., Ström, J., Krejci, R., Quinn, P., and Stohl, A.: A review of sea-spray aerosol source functions using a

25 large global set of sea salt aerosol concentration measurements, Atmos. Chem. Phys., 14, 1277–1297,

26 https://doi.org/10.5194/acp-14-1277-2014, 2014.

28 Grythe, H., Kristiansen, N. I., Groot Zwaaftink, C. D., Eckhardt, S., Ström, J., Tunved, P., Krejci, R., and Stohl, A.: A

29 new aerosol wet removal scheme for the Lagrangian particle model FLEXPART v10, Geosci. Model Dev., 10,

30 1447–1466, https://doi.org/10.5194/gmd-10-1447-2017, 2017.

Grythe, H.: Quantification of sources and removal mechanisms of atmospheric aerosol particles, PhD thesis, Stockholm University, 2017.

Gyawali, M., Arnott, W.P., Lewis, K., Moosmüller, H.: In situ aerosol optics in Reno, NV, USA during and after the summer 2008 California wildfires and the influence of absorbing and non-absorbing organic coatings on spectral light absorption. Atmos. Chem. Phys. 9, 8007-8015, 2009.

Hand, J. L., and Malm, W. C.: Review of aerosol mass scattering efficiencies from ground-based measurements since 1990, J. Geophys. Res., 112, D16203, doi:10.1029/2007JD008484, 2007.

Hara, K., K. Osada, M. Yabuki, G. Hashida, T. Yamanouchi, M. Hayashi, M. Shiobara, C.Nishita, and M.Wada: Haze episodes at Syowa Station, coastal Antarctica: Where did they come from?, J. Geophys. Res., 115, D14205, doi:10.1029/2009JD012582, 2010.

Hara, K., Sudo, K., Ohnishi, T., Osada, K., Yabuki, M., Shiobara, M., and Yamanouchi, T.: Seasonal features and origins of carbonaceous aerosols at Syowa Station, coastal Antarctica, Atmos. Chem. Phys., 19, 7817–7837, https://doi.org/10.5194/acp-19-7817-2019, 2019.

Hara, K., Osada, K., Yabuki, M., Matoba, S., Hirabayashi, M., Fujita, S., Nakazawa, F., and Yamanouchi, T.: Atmospheric seasalt and halogen cycles in the Antarctic, Environ. Sci.: Process Impacts, 22, 2003–2022, https://doi.org/10.1039/d0em00092b, 2020.

Hegg, D., Covert, D., Crahan, K., and Jonssen, H.: The dependence of aerosol light-scattering on RH over the Pacific Ocean, Geophys. Res. Lett., 29, 2002.

Hirdman, D., Sodemann, H., Eckhardt, S., Burkhart, J. F., Jefferson, A., Mefford, T., Quinn, P. K., Sharma, S., Ström, J., and Stohl, A.: Source identification of short-lived air pollutants in the Arctic using statistical analysis of measurement data and particle dispersion model output, Atmos. Chem. Phys., 10, 669–693, https://doi.org/10.5194/acp-10-669-2010, 2010.

Hogan, A.W., S. Barnard, and J. Bortniak: Physical properties of the aerosol at the South Pole, Geophys. Res. Lett., 6, 845–848, 1979.

1 Ito, T.: Antarctic submicron aerosols and long-range transport of pollutants, Ambio,18,34–41, 1989.

3 James, I. N.: The Antarctic drainage flow: Implications for hemispheric flow on the Southern Hemisphere,
4 Antarct. Sci.,1,279–290, doi:10.1017/S0954102089000404., 1989.

6 Jourdain, B., S. Preunkert, O. Cerri, H. Castebrunet, R. Udisti, and M. Legrand: Year-round record of size
7 segregated aerosol composition in central Antarctica (Concordia station): Implications for the degree of
8 fractionation of sea-salt particles, J. Geophys. Res., 113, D14308, doi:10.1029/2007JD009584, 2008

10 Jurányi, Z. and Weller, R.: One year of aerosol refractive index measurement from a coastal Antarctic site,
11 Atmos. Chem. Phys., 19, 14417–14430, https://doi.org/10.5194/acp-19-14417-2019, 2019.

13 Järvinen, E., Virkkula, A., Nieminen, T., Aalto, P. P., Asmi, E., Lanconelli, C., Busetto, M., Lupi, A., Schioppo, R.,
14 Vitale, V., Mazzola, M., Petäjä, T., Kerminen, V.-M., and Kulmala, M.: Seasonal cycle and modal structure of
15 particle number size distribution at Dome C, Antarctica, Atmos. Chem. Phys., 13, 7473-7487, doi:10.5194/acp-
16 13-7473-2013, 2013.

18 Karpetchko, A., Kyro, E., and Knudsen, B.: Arctic and Antarctic polar vortices 1957-2002 as seen from the ERA-
19 40 reanalyses, J. Geophys. Res., 110, D21109, doi:10.1029/2005JD006113, 2005.

21 Kerminen, V. M., Chen, X., Vakkari, V., Petäjä, T., Kulmala, M.,and Bianchi, F.: Atmospheric new particle
22 formation   and   growth:review   of   field   observations,   Environ.   Res.   Lett.,   13,
23 103003,https://doi.org/10.1088/1748-9326/aadf3c, 2018.

25 Kim, J., Yoon, Y. J., Gim, Y., Choi, J. H., Kang, H. J., Park, K.-T., Park, J., and Lee, B. Y.: New particle formation
26 events observed at King Sejong Station, Antarctic Peninsula – Part 1: Physical characteristics and contribution
27 to cloud condensation nuclei, Atmos. Chem. Phys., 19, 7583–7594, https://doi.org/10.5194/acp-19-7583-2019,
28 2019.

30 King, J. C., and Turner, J.: Antarctic Meteorology and Climatology, 409 pp., Cambridge Univ. Press, New York,
31 doi:10.1017/CBO9780511524967, 1997.

Koch, D., Schulz, M., Kinne, S., McNaughton, C., Spackman, J. R., Balkanski, Y., Bauer, S., Berntsen, T., Bond, T. C., Boucher, O., Chin, M., Clarke, A., De Luca, N., Dentener, F., Diehl, T., Dubovik, O., Easter, R., Fahey, D. W., Feichter, J., Fillmore, D., Freitag, S., Ghan, S., Ginoux, P., Gong, S., Horowitz, L., Iversen, T., Kirkevåg, A., Klimont, Z., Kondo, Y., Krol, M., Liu, X., Miller, R., Montanaro, V., Moteki, N., Myhre, G., Penner, J. E., Perlwitz, J., Pitari, G., Reddy, S., Sahu, L., Sakamoto, H., Schuster, G., Schwarz, J. P., Seland, Ø., Stier, P., Takegawa, N., Takemura, T., Textor, C., van Aardenne, J. A., and Zhao, Y.: Evaluation of black carbon estimations in global aerosol models, Atmos. Chem. Phys., 9, 9001–9026, https://doi.org/10.5194/acp-9-9001-2009, 2009.

Krinner G. and Genthon C.: Tropospheric transport of continental tracers towards Antarctica under varying climatic conditions, Tellus B, 55:1, 54-70, DOI: 10.3402/tellusb.v55i1.16354, 2003.

Kirchstetter, T. W., Novakov, T., and Hobbs, P. V.: Evidence that the spectral dependence of light absorption by aerosols is affected by organic carbon, J. Geophys. Res., 109, D21208, https://doi.org/10.1029/2004jd004999, 2004.

Kristiansen, N. I., Stohl, A., and Wotawa, G.: Atmospheric removal times of the aerosol-bound radionuclides ^{137}Cs and ^{131}I measured after the Fukushima Dai-ichi nuclear accident – a constraint for air quality and climate models, Atmos. Chem. Phys., 12, 10759–10769, https://doi.org/10.5194/acp-12-10759-2012, 2012.

Kyrö, E.-M., Grönholm, T., Vuollekoski, H., Virkkula, A., Kulmala, M., and Laakso, L.: Snow scavenging of ultrafine particles: field measurements and parameterization, Boreal Environ. Res., 14,527–538, 2009.

Laakso, L., Grönholm, Rannika, Ü., Kosmalea, M., Fiedlera, V., Vehkamäki, H., and Kulmala, M.: Ultrafine particle scavenging coefficients calculated from 6 years field measurements, Atmos. Environ., 37, 3605–3613, doi:10.1016/S1352-2310(03)00326-1, 2003.

Lachlan-Cope, T., Beddows, D. C. S., Brough, N., Jones, A. E., Harrison, R. M., Lupi, A., Yoon, Y. J., Virkkula, A., and Dall'Osto, M.: On the annual variability of Antarctic aerosol size distributions at Halley Research Station, Atmos. Chem. Phys., 20, 4461–4476, https://doi.org/10.5194/acp-20-4461-2020, 2020.

Lack, D. A. and Cappa, C. D.: Impact of brown and clear carbon on light absorption enhancement, single scatter albedo and absorption wavelength dependence of black carbon, Atmos. Chem. Phys., 10, 4207-4220, doi:10.5194/acp-10-4207-2010, 2010.

Legrand, M., Yang, X., Preunkert, S., and Theys, N.: Year-round records of sea salt, gaseous, and particulate inorganic bromine in the atmospheric boundary layer at coastal (Dumont d'Urville) and central (Concordia) East Antarctic sites, J. Geophys. Res. Atmos., 121, 997–1023, https://doi.org/10.1002/2015JD024066, 2016.

Legrand, M., Preunkert, S., Wolff, E., Weller, R., Jourdain, B., and Wagenbach, D.: Year-round records of bulk and size segregated aerosol composition in central Antarctica (Concordia site) – Part 1: Fractionation of sea-salt particles, Atmos. Chem. Phys., 17, 14039–14054, https://doi.org/10.5194/acp-17-14039-2017, 2017a.

Legrand, M., Preunkert, S., Weller, R., Zipf, L., Elsässer, C., Merchel, S., Rugel, G., and Wagenbach, D.: Year-round record of bulk and size-segregated aerosol composition in central Antarctica (Concordia site) – Part 2: Biogenic sulfur (sulfate and methanesulfonate) aerosol, Atmos. Chem. Phys., 17, 14055–14073, https://doi.org/10.5194/acp-17-14055-2017, 2017b.

Li, H., McMeeking, G. R., and May, A. A.: Development of a new correction algorithm applicable to any filter-based absorption photometer, Atmos. Meas. Tech., 13, 2865–2886, https://doi.org/10.5194/amt-13-2865-2020, 2020.

Liu, D., Allan, J. D., Young, D. E., Coe, H., Beddows, D., Fleming, Z. L., Flynn, M. J., Gallagher, M. W., Harrison, R. M., Lee, J., Prevot, A. S. H., Taylor, J. W., Yin, J., Williams, P. I., and Zotter, P.: Size distribution, mixing state and source apportionment of black carbon aerosol in London during wintertime, Atmos. Chem. Phys., 14, 10061–10084, https://doi.org/10.5194/acp-14-10061-2014, 2014.

Luoma, K., Virkkula, A., Aalto, P., Lehtipalo, K., Petäjä, T., and Kulmala, M.: Effects of different correction algorithms on absorption coefficient – a comparison of three optical absorption photometers at a boreal forest site, Atmos. Meas. Tech., 14, 6419–6441, https://doi.org/10.5194/amt-14-6419-2021, 2021.

1 McMeeking, G. R., Hamburger, T., Liu, D., Flynn, M., Morgan, W. T., Northway, M., Highwood, E. J., Krejci, R.,

2 Allan, J. D., Minikin, A., and Coe, H.: Black carbon measurements in the boundary layer over western and

3 northern Europe, Atmos. Chem. Phys., 10, 9393–9414, https://doi.org/10.5194/acp-10-9393-2010, 2010.

5 Mikhailov, E., Vlasenko, S., Podgorny, I., Ramanathan, V., and Corrigan, C.: Optical properties of soot-water

6 drop agglomerates: An experimental study, J. Geophys. Res., 111, 1–16, 2006.

7 Mishchenko, M. I., Travis, L., and Lacis, A.: Scattering, Absorption, and Emission of Light by Small Particles,

8 Cambridge University Press, 2002.

10 Morganti, A., Becagli, S., Castellano, E., Severi, M., Traversi, R., Udisti R.: An improved flow analysis-ion

11 chromatography method for determination of cationic and anionic species at trace levels in Antarctic ice cores.

12 Anal. Chim. Acta, 603, 190–198, 2007.

14 Müller, T., Virkkula, A., and Ogren, J. A.: Constrained two-stream algorithm for calculating aerosol light

15 absorption coefficient from the Particle Soot Absorption Photometer, Atmos. Meas. Tech., 7, 4049–4070,

16 https://doi.org/10.5194/amt-7-4049-2014, 2014.

18 Ogren, J. A.: Comment on "Calibration and Intercomparison of Filter-Based Measurements of Visible Light

19 Absorption by Aerosols," Aerosol Sci. Technol., 44(8), 589–591, doi:10.1080/02786826.2010.482111, 2010.

21 Papastefanou, C.: Residence time of tropospheric aerosols in association with radioactive nuclides, Appl.

22 Radiat. Isotopes, 64, 93–100, 2006.

24 Parish, T.R. and Bromwich, D.H.: Continental-scale simulation of the Antarctic katabatic wind regime, J. Clim.,

25 4, 135–146, https://doi.org/10.1175/1520-0442(1991)004<0135:cssota>2.0.co;2, 1991.

27 Pereira, G., Siqueira, R., Rosário, N. E., Longo, K. L., Freitas, S. R., Cardozo, F. S., Kaiser, J. W., and Wooster, M.

28 J.: Assessment of fire emission inventories during the South American Biomass Burning Analysis (SAMBBA)

29 experiment, Atmos. Chem. Phys., 16, 6961–6975, https://doi.org/10.5194/acp-16-6961-2016, 2016.

Petzold, A., Ogren, J. A., Fiebig, M., Laj, P., Li, S.-M., Baltensperger, U., Holzer-Popp, T., Kinne, S., Pappalardo, G., Sugimoto, N., Wehrli, C., Wiedensohler, A., and Zhang, X.-Y.: Recommendations for reporting "black carbon" measurements, Atmos. Chem. Phys., 13, 8365–8379, https://doi.org/10.5194/acp-13-8365-2013, 2013.

Pisso, I., Sollum, E., Grythe, H., Kristiansen, N. I., Cassiani, M., Eckhardt, S., Arnold, D., Morton, D., Thompson, R. L., Groot Zwaaftink, C. D., Evangeliou, N., Sodemann, H., Haimberger, L., Henne, S., Brunner, D., Burkhart, J. F., Fouilloux, A., Brioude, J., Philipp, A., Seibert, P., and Stohl, A.: The Lagrangian particle dispersion model FLEXPART version 10.4, Geosci. Model Dev., 12, 4955–4997, https://doi.org/10.5194/gmd-12-4955-2019, 2019.
Pratt, K. A., Murphy, S. M., Subramanian, R., DeMott, P. J., Kok, G. L., Campos, T., Rogers, D. C., Prenni, A. J., Heymsfield, A. J., Seinfeld, J. H., and Prather, K. A.: Flight-based chemical characterization of biomass burning aerosols within two prescribed burn smoke plumes, Atmos. Chem. Phys., 11, 12549–12565, https://doi.org/10.5194/acp-11-12549-2011, 2011.

Quinn, P. K., Miller, T. L., Bates, T. S., Ogren, J. A., Andrews, E., and Shaw, G. E.: A 3-year record of simultaneously measured aerosol chemical and optical properties at Barrow, Alaska, J. Geophys. Res.-Atmos., 107, 4130, doi:10.1029/2001JD001248, 2002.

Reid, J. S., Hyer, E. J., Prins, E. M., Westphal, D. L., Zhang, J., Wang, J., Christopher, S. A., Curtis, C. A., Schmidt, C. C., Eleuterio, D. P., Richardson, K. A., and Hoffman, J. P.: Global monitoring and forecasting of biomass-burning smoke: Description and lessons from the Fire Locating and Modeling of Burning Emissions (FLAMBE) program, J. Sel. Topics Appl. Earth Obs. Rem. Sens., 2, 144–162, 2009.

Rémy, S., Veira, A., Paugam, R., Sofiev, M., Kaiser, J. W., Marenco, F., Burton, S. P., Benedetti, A., Engelen, R. J., Ferrare, R., and Hair, J. W.: Two global data sets of daily fire emission injection heights since 2003, Atmos. Chem. Phys., 17, 2921–2942, https://doi.org/10.5194/acp-17-2921-2017, 2017.

Russell, P., Bergstrom, R., Shinozuka, Y., Clarke, A., DeCarlo, P., Jimenez, J., Livingston, J., Redemann, J., Dubovik, O., Strawa, A.: Absorption Angstrom Exponent in AERONET and related data as an indicator of aerosol composition. Atmos. Chem. Phys. 10, 1155-1169, 2010.

Seibert, P. and Frank, A.: Source-receptor matrix calculation with a Lagrangian particle dispersion model in backward mode, Atmos. Chem. Phys., 4, 51–63, 2004, http://www.atmos-chem-phys.net/4/51/2004/.

Seinfeld, J. H., and S. N. Pandis: Atmospheric Chemistry and Physics: From Air Pollution to Climate Change, John Wiley, Hoboken, N. J., 1998.

Shaw, G.: Considerations on the Origin and Properties of the Antarctic Aerosol, Rev. Geophys. 8, 1983 – 1998, 1979.

Shen, Y., Virkkula, A., Ding, A., Wang, J., Chi, X., Nie, W., Qi, X., Huang, X., Liu, Q., Zheng, L., Xu, Z., Petäjä, T., Aalto, P. P., Fu, C., and Kulmala, M.: Aerosol optical properties at SORPES in Nanjing, east China, Atmos. Chem. Phys., 18, 5265–5292, https://doi.org/10.5194/acp-18-5265-2018, 2018.

Sheridan, P., Andrews, E., Schmeisser, L., Vasel, B., and Ogren, J.: Aerosol measurements at South Pole: climatology and impact of local contamination. Aerosol Air Qual. Res. 16, 855–872. https://doi.org/10.4209/aaqr.2015.05.0358, 2016.

Sherman, J. P., Sheridan, P. J., Ogren, J. A., Andrews, E., Hageman, D., Schmeisser, L., Jefferson, A., and Sharma, S.: A multi-year study of lower tropospheric aerosol variability and systematic relationships from four North American regions, Atmos. Chem. Phys., 15, 12487–12517, https://doi.org/10.5194/acp-15-12487-2015, 2015.

Shikwambana, L. and Kganyago, M.: Observations of Emissions and the Influence of Meteorological Conditions during Wildfires: A Case Study in the USA, Brazil, and Australia during the 2018/19 Period. Atmosphere, 12, 11. https://dx.doi.org/10.3390/atmos12010011, 2021.

Singh, H. B., Viezee, W., Chen, Y., Bradshaw, J., Sandholm, S., Blake, D., Blake, N., Heikes, B., Snow, J., Talbot, R., Browell, E., Gregory, G., Sachse, G., and Vay, S.: Biomass burning influences on the composition of the remote South Pacific troposphere: analysis based on observations from PEM-Tropics-A, Atmos. Environ., 34(4), 635–644, 2000.

Springston, S.R.: Particle Soot Absorption Photometer (PSAP) Instrument Handbook; DOE ARM Climate Research Facility: Washington, DC, USA, 2018.

1   Staudt, A. C., Jacob, D. J., Logan, J. A., Bachiochi, D., Krishnamurti, T. N., and Poisson, N.: Global chemical model

2   analysis of biomass burning and lightning influences over the South Pacific in austral spring, J. Geophys. Res.,

3   107, 4200, doi:10.1029/2000JD000296, 2002.

5   Stohl, A. and Sodemann, H.: Characteristics of atmospheric transport into the Antarctic troposphere, J.

6   Geophys. Res., 115, D02305, doi:10.1029/2009JD012536, 2010.

8   Stohl, A., Forster, C., Frank, A., Seibert, P., and Wotawa, G.: Technical note: The Lagrangian particle dispersion

9   model FLEXPART version 6.2, Atmos. Chem. Phys., 5, 2461–2474, https://doi.org/10.5194/acp-5-2461-2005,

10   2005.

12   Tomasi, C., Vitale, V., Lupi, A., Di Carmine, C., Campanelli, M., Herber, A., Treffeisen, R., Stone, R-S., Andrews,

13   E., Sharma, S., Radionov, V., von Hoyningen-Huene, W., Stebel, K., Hansen, G.H., Myhre, C.L., Wehrli, C.,

14   Aaltonen, V., Lihavainen, H., Virkkula, A., Hillamo, R., Ström, J., Toledano, C., Cachorro, V.E., Ortiz, P., de Frutos,

15   A.M., Blindheim, S., Frioud, M., Gausa, M., Zielinski, T., Petelski, T., and Yamanouchi, T.: Aerosols in polar

16   regions: A historical overview on the basis of optical depth and in situ observations, J. Geophys. Res., 112,

17   D16205, doi:10.1029/2007JD008432, 2007.

19   Tosca, M. G., Randerson, J. T., Zender, C. S., Nelson, D. L., Diner, D. J., and Logan, J. A.: Dynamics of fire plumes

20   and smoke clouds associated with peat and deforestation fires in Indonesia, J. Geophys. Res., 116, D08207,

21   doi:10.1029/2010JD015148, 2011.

23   Udisti, R., Becagli, S., Benassai, S., Castellano, E., Fattori, I., Innocenti, M., Migliori, A., Traversi, R.: Atmosphere-

24   snow interaction by a comparison between aerosol and uppermost snow layers composition at Dome C (East

25   Antarctica). Ann. Glaciol, 39, 53–61, 2004.

27   Udisti, R., Dayan, U., Becagli, S., Busetto, M., Frosini, D., Legrand, M., Lucarelli, F., Preunkert, S., Severi, M.,

28   Traversi, R., and Vitale, V.: Sea spray aerosol in central Antarctica. Present atmospheric behaviour and

29   implications for paleoclimatic reconstructions, Atmos. Environ., 52, 109–120, 2012.

Ulke, A. G., Longo, K. M., and de Freitas, S. R.: Biomass Burning in South America: Transport Patterns and Impacts, in: Biomass – Detection, Production and Usage, edited by M. D. Matovic, InTech, Rijeka, Croatia, https://doi.org/10.5772/19264, 2011.

Virkkula, A.: Correction of the Calibration of the 3-wavelength Particle Soot Absorption Photometer (3 PSAP), Aerosol Sci. Tech., 44, 706–712, https://doi.org/10.1080/02786826.2010.482110, 2010.

Virkkula, A.: Modeled source apportionment of black carbon particles coated with a light-scattering shell, Atmos. Meas. Tech., 14, 3707–3719, https://doi.org/10.5194/amt-14-3707-2021, 2021.

Virkkula, A., Ahlquist, N. C., Covert, D. S., Arnott, W. P., Sheridan, P. J., Quinn, P. K., and Coffman, D. J.: Modification, calibration and a field test of an instrument for measuring light absorption by particles, Aerosol Sci. Tech., 39, 68–83, https://doi.org/10.1080/027868290901963, 2005.

Virkkula, A., Koponen, I. K., Teinilä, K., Hillamo, R., Kerminen, V.-M., and Kulmala, M.: Effective real refractive index of dry aerosols in the Antarctic boundary layer, Geophys. Res. Lett., 33, L06805, https://doi.org/10.1029/2005GL024602, 2006.

Voshchinnikov, N.V. and Mathis, J.S.: Calculating Cross Sections of Composite Interstellar Grains, Astrophys. J., 526, 257–264, https://doi.org/10.1086/307997, 1999.

Waugh, D. W., Sobel, A. H., and Polvani, L. M.: What is the polar vortex and how does it influence weather, B. Am. Meteorol. Soc., 98, 37–44, https://doi.org/10.1175/BAMS-D-15-00212.1, 2017.

Weller, R., Minikin, A., Petzold, A., Wagenbach, D., and König-Langlo, G.: Characterization of long-term and seasonal variations of black carbon (BC) concentrations at Neumayer, Antarctica, Atmos. Chem. Phys., 13, 1579–1590, https://doi.org/10.5194/acp-13-1579-2013, 2013.

Weller, R., Schmidt, K., Teinilä, K., and Hillamo, R.: Natural new particle formation at the coastal Antarctic site Neumayer, Atmos. Chem. Phys., 15, 11399–11410, doi:10.5194/acp-15-11399-2015, 2015.

1 Williams, J., de Reus, M., Krejci, R., Fischer, H., and Ström, J.: Application of the variability-size relationship to

2 atmospheric aerosol studies: estimating aerosol lifetimes and ages, Atmos. Chem. Phys., 2, 133–145, 2002,

3 http://www.atmos-chem-phys.net/2/133/2002/.

5 WMO/GAW Report No. 227: Aerosol Measurement Procedures,Guidelines and Recommendations, 2nd

6 Edn., 103 pp., August2016 (WMO-No. 1177), Geneva, Switzerland, 2016.

8 Wu Z.P., Wang Y.P.: Electromagnetic scattering for multilayered spheres: recursive algorithms, Radio Science,

9 26, 1393-1401, 1991.

11 Xu, H., Ren, Y., Zhang, W., Meng, W., Yun, X., Yu, X., Li, J., Zhang, Y., Shen, G., Ma, J., Li, B., Cheng, H., Wang, X.,

12 Wan, Y, and Tao, S.: Updated Global Black Carbon Emissions from 1960 to 2017: Improvements, Trends, and

13 Drivers. Environmental Science and Technology, 55 (12), 7869-7879, DOI: 10.1021/acs.est.1c0311, 2021.

1 **Tables**

2 Table 1. Seasonal variation of the fractions of volume concentration and scattering coefficients in the size range
3 measured by the DMPS of the respective values calculated from the combined size distributions measured with
4 the DMPS and the OPC at Dome C in December 2007 – July 2009.

	fV(DMPS), %		$f\sigma_{sp}$(DMPS,467), %		$f\sigma_{sp}$(DMPS,530), %		$f\sigma_{sp}$(DMPS,660), %	
month	average ± std	median	average ± std	median	average ± std	median	average ± std	median
JAN	85.7 ± 11.4	91.2	84.2 ± 10.4	88.3	77.3 ± 13.1	81.8	64.6 ± 16.3	68.7
FEB	85.1 ± 14.3	90.5	82.4 ± 14.6	87.1	75.6 ± 16.2	81.0	63.4 ± 17.8	68.4
MAR	78.9 ± 21.2	88.7	76.8 ± 20.7	85.6	70.0 ± 22.1	78.9	58.7 ± 22.7	66.3
APR	72.3 ± 23.5	83.8	72.7 ± 21.7	80.9	65.6 ± 23.2	73.1	54.5 ± 24.0	59.6
MAY	53.8 ± 24.8	48.9	60.5 ± 22.0	61.8	52.6 ± 23.0	51.9	41.4 ± 23.0	37.9
JUN	48.2 ± 18.3	48.7	59.5 ± 15.8	62.7	50.6 ± 15.5	53.0	38.0 ± 13.8	39.4
JUL	48.4 ± 18.3	47.9	60.6 ± 16.0	63.5	52.0 ± 15.9	54.2	39.6 ± 14.7	40.5
AUG	53.5 ± 15.5	55.3	66.3 ± 14.7	69.5	58.1 ± 14.6	60.4	45.7 ± 14.0	46.4
SEP	61.9 ± 14.3	64.1	72.2 ± 13.3	73.8	64.5 ± 13.6	65.9	52.4 ± 14.0	52.8
OCT	63.7 ± 14.2	65.5	72.5 ± 13.2	73.8	64.9 ± 13.7	65.8	52.6 ± 14.2	52.7
NOV	74.0 ± 13.2	77.0	76.9 ± 10.1	79.0	68.8 ± 11.5	70.8	55.2 ± 12.6	56.4
DEC	80.3 ± 13.6	84.0	79.9 ± 10.3	82.9	71.7 ± 11.4	74.9	57.2 ± 11.9	59.8
year	69.2 ± 22.3	73.8	73.0 ± 18.2	77.1	65.4 ± 19.3	68.8	53.1 ± 19.7	54.6

7 Table 2. Noise of scattering and absorption coefficients calculated from the particle number size distributions
8 and the PSAP data. σ_{sp}(DMPS,PM$_{0.8}$) and σ_{sp}(DMPS,PM$_{10}$). Noise was estimated as explained in section 2.5.

Average noise of scattering and absorption coefficients, Mm^{-1}								
Scattering	$\delta\sigma_{sp}$(DMPS,PM$_{0.8}$)			$\delta\sigma_{sp}$(DMPS,PM$_{10}$)				
$\Delta t \setminus \lambda$(nm)	467	530	660	467	530	660		
1 h	5.2×10^{-2}	4.2×10^{-2}	2.7×10^{-2}	7.2×10^{-2}	6.5×10^{-2}	5.3×10^{-2}		
24 h	1.1×10^{-2}	0.85×10^{-2}	0.55×10^{-2}	1.5×10^{-2}	1.3×10^{-2}	1.1×10^{-2}		
Average noise of PSAP data scattering correction, Mm^{-1}								
	0.0164×$\delta\sigma_{sp}$(DMPS,PM$_{0.8}$)			0.0164×$\delta\sigma_{sp}$(DMPS,PM$_{10}$)				
1 h	0.85×10^{-3}	0.68×10^{-3}	0.44×10^{-3}	1.2×10^{-3}	1.1×10^{-3}	0.87×10^{-3}		
24 h	0.17×10^{-3}	0.14×10^{-3}	0.091×10^{-3}	0.24×10^{-3}	0.22×10^{-3}	0.18×10^{-3}		
Absorption	$\delta\sigma_{ap,nsc}$			$\delta\sigma_{ap}(\sigma_{sp}$(PM$_{0.8}$))			$\delta\sigma_{ap}(\sigma_{sp}$(PM$_{10}$))		
$\Delta t \setminus \lambda$(nm)	467	530	660	467	530	660	467	530	660
1 h	3.2×10^{-3}	2.5×10^{-3}	2.7×10^{-3}	4.0×10^{-3}	3.2×10^{-3}	3.2×10^{-3}	4.3×10^{-3}	3.6×10^{-3}	3.6×10^{-3}
24 h	0.65×10^{-3}	0.52×10^{-3}	0.56×10^{-3}	0.82×10^{-3}	0.66×10^{-3}	0.65×10^{-3}	0.89×10^{-3}	0.74×10^{-3}	0.74×10^{-3}

11 Table 3. Noise and detection limits of eBC concentration calculated from the noise of the absorption
12 coefficients presented in Table 2.

eBC noise, ng m^{-3}			
	$\delta(eBC(\sigma_{ap,nsc}))$	$\delta(eBC(\sigma_{ap}(\sigma_{sp}$(DMPS,PM$_{0.8}$))))	$\delta(eBC(\sigma_{ap}(\sigma_{sp}$(DMPS,PM$_{10}$))))
1 h	0.327	0.415	0.464
24 h	0.067	0.085	0.100
eBC detection limits, ng m^{-3}			
	$2\delta(eBC(\sigma_{ap,nsc}))$	$2\delta(eBC(\sigma_{ap}(\sigma_{sp}$(DMPS,PM$_{0.8}$))))	$2\delta(eBC(\sigma_{ap}(\sigma_{sp}$(DMPS,PM$_{10}$))))
1 h	0.65	0.83	0.93
24 h	0.13	0.17	0.20

Table 4. Descriptive statistics of aerosol optical properties at Dome C in 2008 – 2013.

	λ (nm)	N	Ave ± std	5	25	50	75	95
						Percentiles		
Extensive AOPs								
Scattering coefficient, σ_{sp}, Mm^{-1}								
Filter samples								
$\sigma_{sp}(PM_{10})$	550	1765	0.31 ± 0.31	0.058	0.139	0.24	0.38	0.75
$\sigma_{sp}(PM_1)$	550	468	0.30 ± 0.23	0.046	0.118	0.24	0.41	0.75
DMPS-data								
$\sigma_{sp}(DMPS, PM_{0.8}))$	467	21987	0.35 ± 0.64	0.034	0.095	0.19	0.40	1.06
	530	21987	0.27 ± 0.51	0.026	0.073	0.15	0.30	0.80
	660	21987	0.16 ± 0.32	0.016	0.044	0.09	0.18	0.46
$\sigma_{sp}(DMPS, PM_{10}))$	467	21987	0.49 ± 0.98	0.054	0.141	0.27	0.52	1.36
	530	21987	0.42 ± 0.90	0.047	0.123	0.23	0.44	1.13
	660	21987	0.31 ± 0.75	0.035	0.091	0.16	0.32	0.80
Absorption coefficient, σ_{ap}, Mm^{-1}								
σ_{ap}, calculated using B1999								
$\sigma_{ap}(\sigma_{sp}(DMPS,PM_{10}))$	467	15778	0.015 ± 0.017	< 0.001	0.0028	0.0095	0.021	0.051
	530	15815	0.013 ± 0.015	< 0.001	0.0028	0.0085	0.019	0.044
	660	15657	0.011 ± 0.012	< 0.001	0.0032	0.0076	0.016	0.036
σ_{ap}, calculated using V2010								
$\sigma_{ap}(\sigma_{sp}(DMPS,PM_{10}))$	467	15778	0.016 ± 0.018	< 0.001	0.0032	0.0099	0.022	0.053
	530	15815	0.012 ± 0.015	< 0.001	0.0022	0.0076	0.017	0.041
	660	15657	0.009 ± 0.011	< 0.001	0.0016	0.0056	0.013	0.030
Intensive AOPs								
Single-scattering albedo $\omega_o = \sigma_{sp}(DMPS,PM_{10})/(\sigma_{sp}(DMPS,PM_{10}) + \sigma_{ap})$								
σ_{ap} calculated using B1999								
$\omega_o(\sigma_{ap,nsc})$	530	15815	0.933 ± 0.048	0.845	0.909	0.944	0.972	0.985
$\omega_o(\sigma_{sp}(DMPS,PM_{10}))$	530	15815	0.948 ± 0.049	0.857	0.923	0.959	0.988	1.000
σ_{ap} calculated using V2010								
$\omega_o(\sigma_{sp}(DMPS,PM_{10}))$	530	15815	0.952 ± 0.047	0.864	0.928	0.963	0.990	1.000
Scattering Ångström exponent α_{sp} (λ=467/660 nm)								
$\alpha_{sp}(\sigma_{sp}(DMPS,PM_{0.8}))$	467/660	21987	2.31 ± 0.28	1.90	2.10	2.25	2.54	2.79
$\alpha_{sp}(\sigma_{sp}(DMPS,PM_{10}))$	467/660	21987	1.34 ± 0.40	0.75	1.03	1.28	1.65	2.03
Absorption Ångström exponent (λ=467/660 nm) α_{abs} for $\sigma_{ap} > 3\ \delta\sigma_{ap}$								
σ_{ap} calculated using B1999								
$\alpha_{ap}(\sigma_{ap,nsc})$	467/660	15607	0.86 ± 0.34	0.29	0.67	0.87	1.02	1.37
$\alpha_{ap}(\sigma_{sp}(DMPS,PM_{10}))$	467/660	11475	0.76 ± 0.47	< 0	0.56	0.82	0.99	1.41
σ_{ap} calculated using V2010								
$\alpha_{ap}(\sigma_{sp}(DMPS,PM_{10}))$	467/660	10270	1.38 ± 0.39	0.73	1.18	1.38	1.60	2.03

Table 5. Statistical summary of mass concentrations estimated from particle number size distributions, sums of ion concentrations of PM_1 and PM_{10} filter samples and the PSAP data at Dome C in 2008 – 2013. The statistical values of the PM_1 and PM_{10} are those of all individual filters, the statistical values calculated from the DMPS and PSAP data are those of running 24h-averaged data, see details in the text. $m(DMPS,PM_{0.8})$: mass concentration calculated from the particle number size distributions measured with the DMPS assuming particle density of 1.7 g cm^{-3}; eBC: equivalent Black Carbon concentration calculated from the absorption coefficients at λ=530 nm calculated by using the B1999 algorithm without any scattering corrections and with B1999 and V2010 algorithms using $\sigma_{sp} = \sigma_{sp}(DMPS,PM_{10})$ for the scattering corrections and assuming MAC = 7.78 m^2 g^{-1}. fPM_{10}: scattering-corrected eBC mass fraction calculated from eBC/m(DMPS,PM_{10})×100%; $fPM_{0.8}$: scattering-corrected eBC mass fraction calculated from eBC/m(DMPS,$PM_{0.8}$)×100%.

	N	Ave ± std	Percentiles				
			5	25	50	75	95
Mass concentrations							
PM_{10} filters, ng m^{-3}	1765	162 ± 161	30	73	126	201	394
PM_1 filters, ng m^{-3}	468	82 ± 64	13	33	66	114	208
m(DMPS, $PM_{0.8}$), ng m^{-3}	21987	123 ± 161	12	31	70	150	382
m(DMPS, PM_{10}), ng m^{-3}	21987	173 ± 260	23	55	110	200	488
eBC from $\sigma_{ap}(\lambda = 530$ nm) calculated using B1999							
eBC(no σ_{sp} correction), ng m^{-3}	15815	2.6 ± 2.6	0.36	0.94	1.86	3.2	7.6
eBC(σ_{sp}(DMPS,PM_{10}))), ng m^{-3}	15815	1.7 ± 2.0	< 0.2	0.36	1.09	2.4	5.7
feBC(m(DMPS,$PM_{0.8}$)), %	15815	2.6 ± 2.7	< 0.1	0.51	1.60	4.0	7.7
feBC(m(DMPS,PM_{10})), %	15815	1.6 ± 1.7	< 0.1	0.34	1.14	2.4	4.7
eBC from $\sigma_{ap}(\lambda = 530$ nm) calculated using V2010							
eBC(σ_{sp}(DMPS,PM_{10}))), ng m^{-3}	15815	1.6 ± 1.9	< 0.2	0.28	0.97	2.2	5.3
feBC(m(DMPS,$PM_{0.8}$)), %	15815	2.4 ± 2.6	< 0.1	0.39	1.47	3.7	7.3
feBC(m(DMPS,PM_{10})), %	15815	1.5 ± 1.6	< 0.1	0.26	1.04	2.2	4.4
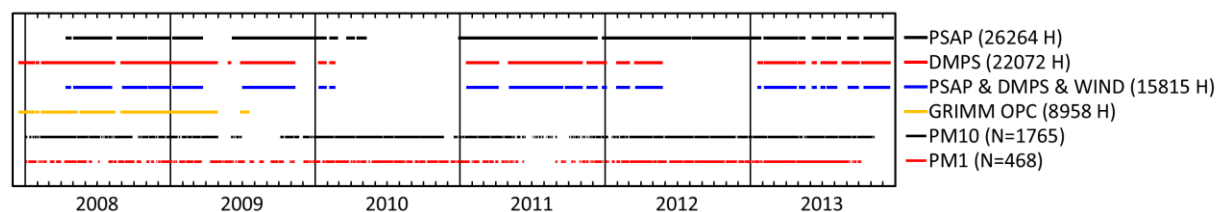
1 **Figures**

3 Figure 1. The periods of the PSAP, the DMPS, the Grimm OPC and the PM_1 and PM_{10} filter sample data. The

4 number of hours of accepted data and the number of samples are shown in parentheses for the continuous

5 instruments and the filter samplers, respectively.
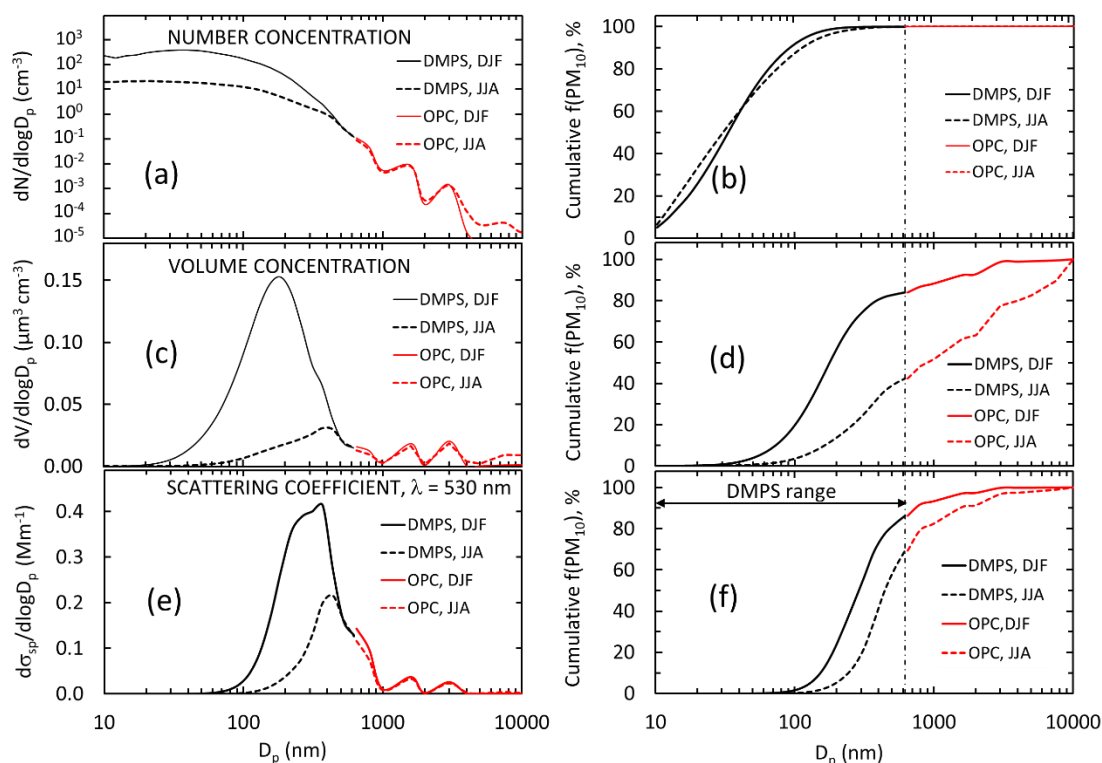
9 Figure 2. Average particle size distributions in summer (DJF) and in winter (JJA) in December 2007 – July 2009

10 when both the DMPS and the Grimm OPC were operational. Left: average and median (a) number, (c) volume,

11 and (e) scattering size distributions at λ =530 nm; right (b, d, and f): cumulative fractions of the respective

12 parameters in the size range D_p < 7.5 μm. which corresponds to the aerodynamic particle size range D_a < 9.8

13 μm.
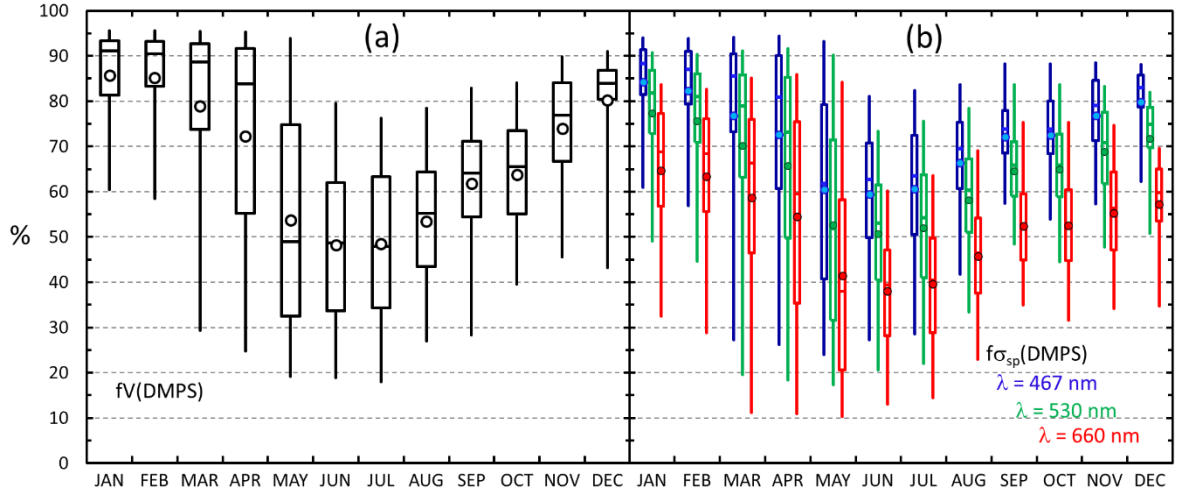
2 Figure 3. Seasonal cycle of the contribution of the size range measured by the DMPS to a) volume

3 concentration and b) scattering coefficient at the PSAP wavelengths in December 2007 – July 2009 when both

4 the DMPS and the Grimm OPC were operational. The circle shows the average, the horizontal line the median,

5 the box the 25th to 75th percentile range, and the whiskers the 5th to 95th percentile range in each month.
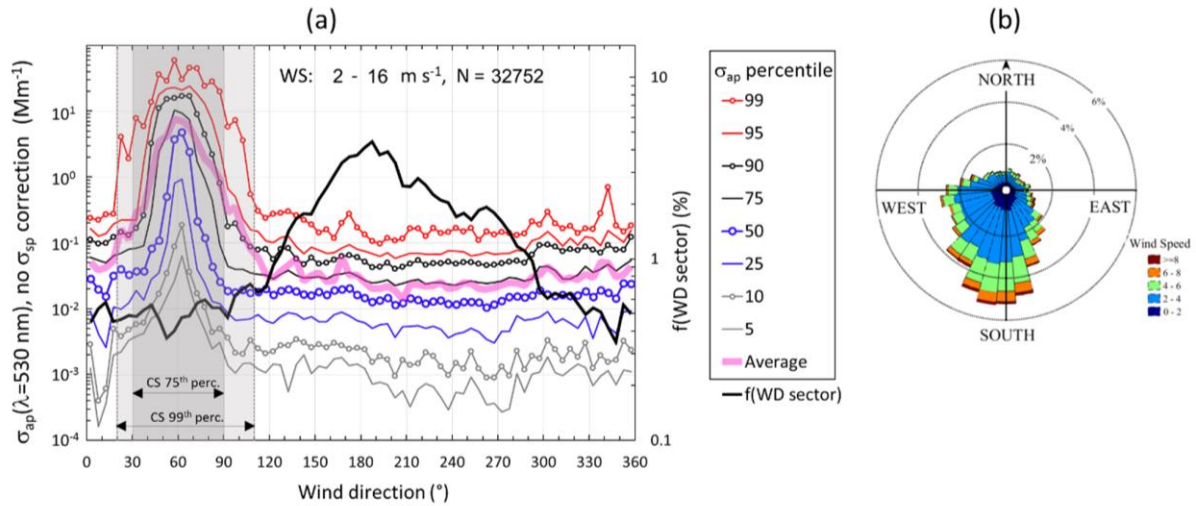
8 Figure 4. Wind and absorption coefficient. a) Hourly-averaged non-scattering-corrected absorption coefficients

9 ($\sigma_{ap,nsc}$, Eq. (1)) observed at wind speed WS > 2 m/s in 5° wind direction (WD) sectors. The lines present the

10 percentiles of the cumulative $\sigma_{ap,nsc}$ distribution in each WD sector. f(WD sector): fraction of wind data from

11 each sector. CS 75th perc.: Contamination sector determined from the 75th percentiles of the cumulative $\sigma_{ap,nsc}$

12 distribution. CS 99th perc.: Contamination sector determined from the 99th percentiles of the cumulative $\sigma_{ap,nsc}$

13 distribution. b) Distribution of WS and WD as a wind rose.
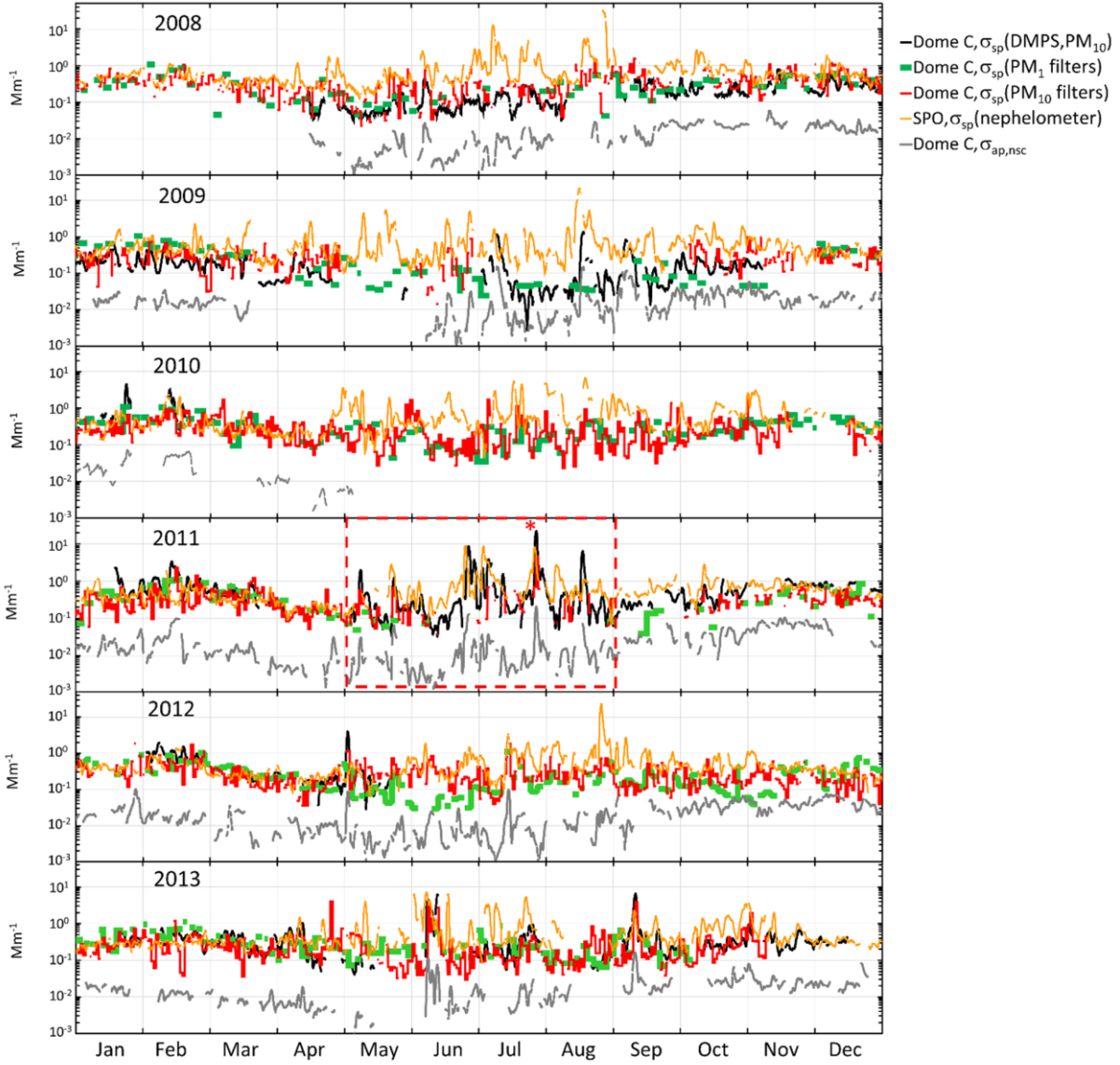
2   Figure 5. Time series of scattering coefficients calculated from the DMPS (σ_{sp}(DMPS,PM$_{10}$) at λ = 530), PM$_1$ and

3   PM$_{10}$ (λ = 550) filter data measured at Dome C and measured with the nephelometer at the South Pole Station

4   (SPO) (λ = 550) and $\sigma_{ap,nsc}$(λ = 530) measured with the PSAP at Dome C. The σ_{sp} from the DMPS and the

5   nephelometer and $\sigma_{ap,nsc}$ are running 24-hour averages at each hour ($\pm$ 12 hours), and the σ_{sp} from the PM1

6   and PM10 filters are those calculated for each filter. The red box within the 2011 time series shows the period

7   presented in more detail in Fig. 6 and the red asterisk symbol (*) for which the footprint in Fig. 7 was

8   calculated.
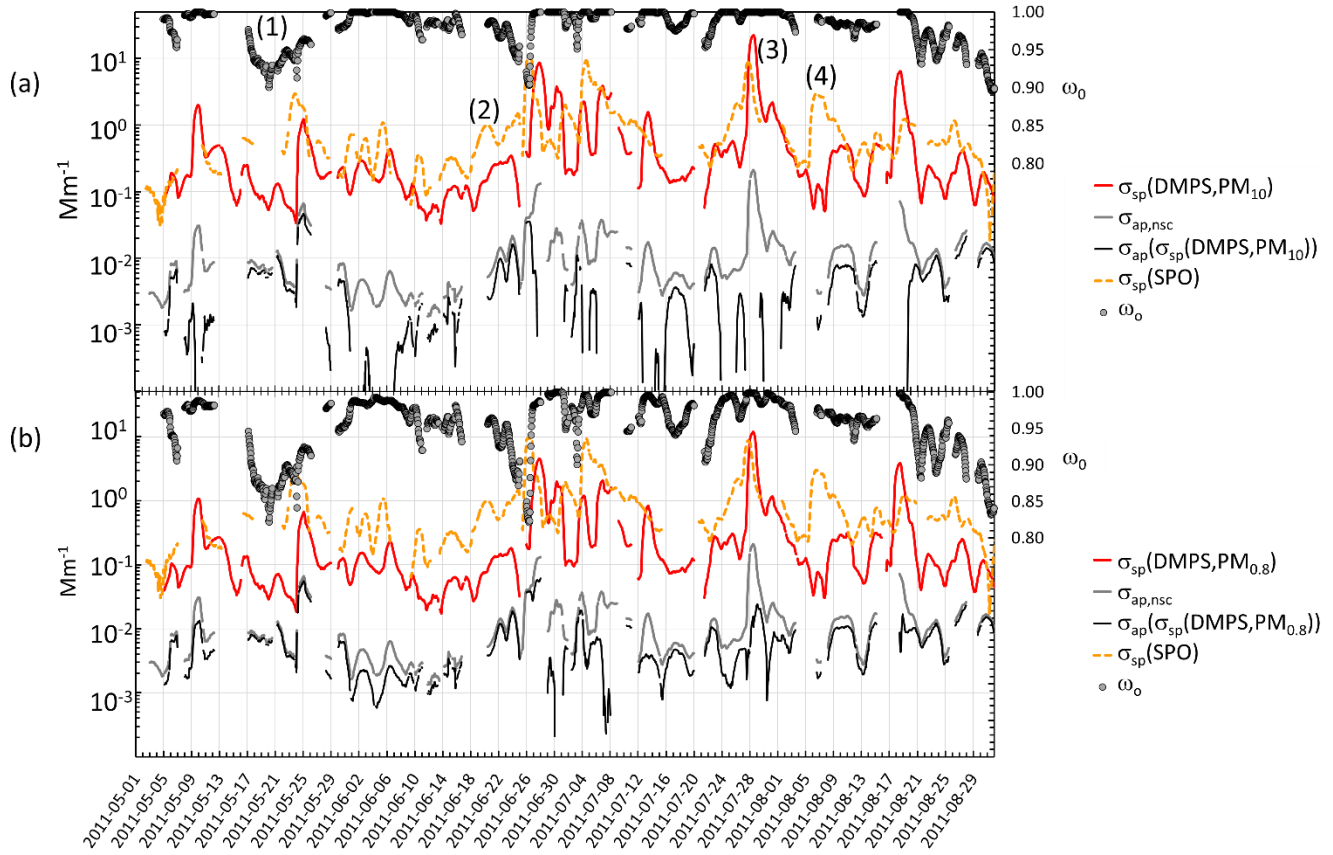
Figure 6. Four-month time series (May-August 2011) of σ_{sp}, σ_{ap} and ω_o at λ = 530 nm at Dome C and σ_{sp} at at λ = 550 nm at the South Pole Station (SPO): a) upper estimate of σ_{sp} (= σ_{sp}(DMPS,PM$_{10}$)), lower estimate of σ_{ap} (= $\sigma_{ap}(\sigma_{sp}$(DMPS, PM$_{10}$))) and upper estimate of ω_o. b) lower estimate of σ_{sp} (= σ_{sp}(DMPS, PM$_{0.8}$))), upper estimate of σ_{ap} (= $\sigma_{ap}(\sigma_{sp}$(DMPS, PM$_{0.8}$))) and lower estimate of ω_o. In both a) and b) also the non-scattering-corrected absorption coefficient is shown. All values are running 24-hour averages at each hour (± 12 hours). The numbers 1 – 4 are discussed in the text.
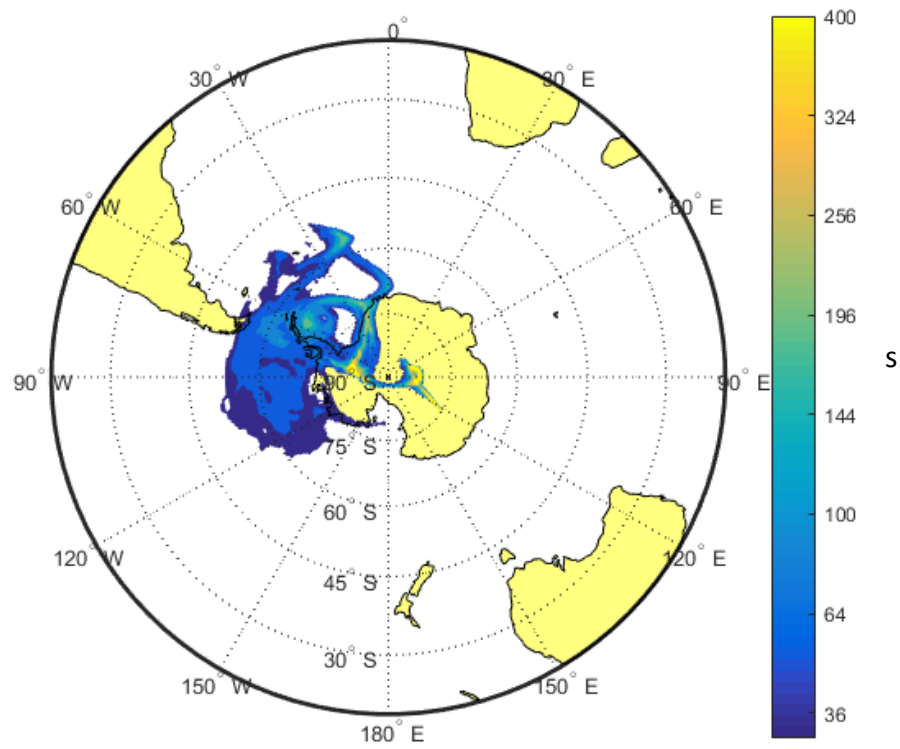
4 Figure 7. FLEXPART footprint of the overall highest day of scattering in winter 2011, on Jul 28, 2011, indicated

5 by the number (3) in Fig. 6.
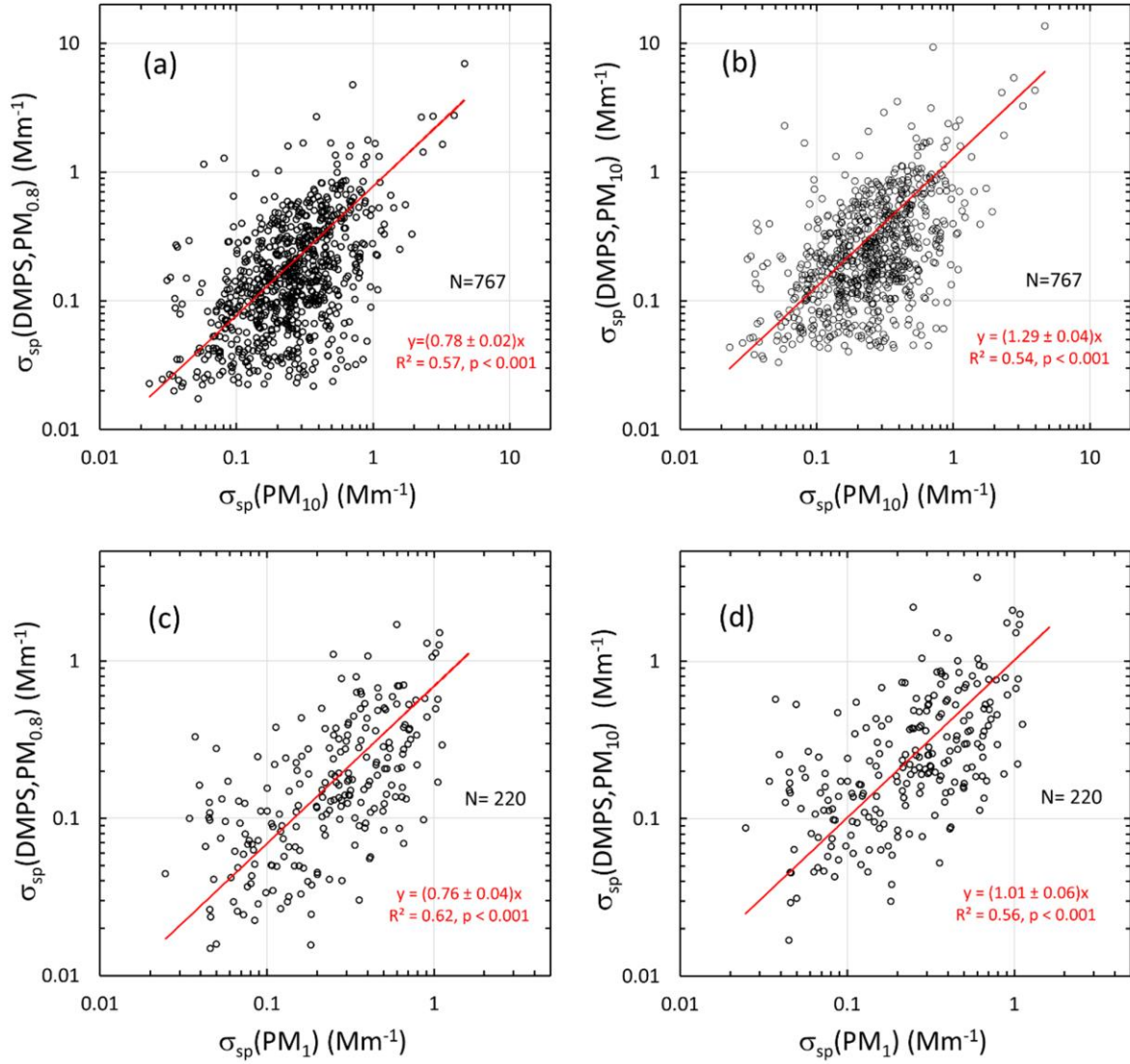
Figure 8. Comparison of scattering coefficients calculated from the DMPS vs. scattering coefficients calculated from the PM$_1$ and PM$_{10}$ filter sample data at Dome C, all at λ = 550 nm. The scattering coefficients calculated from the DMPS data were averaged for the sampling times of the PM$_1$ and PM$_{10}$ samples and interpolated to λ = 550 nm. a) lower estimate of σ$_{sp}$ (= σ$_{sp}$(DMPS, PM$_{0.8}$)) vs. σ$_{sp}$(PM$_{10}$), b) upper estimate of σ$_{sp}$ (= σ$_{sp}$(DMPS,PM$_{10}$)) vs. σ$_{sp}$(PM$_{10}$), c) σ$_{sp}$(DMPS, PM$_{0.8}$)) vs. σ$_{sp}$(PM$_1$), d) σ$_{sp}$(DMPS,PM$_{10}$)) vs. σ$_{sp}$(PM$_1$). N: number of data points. The red line shows the linear regression line that is forced through zero. The regression equations show the slope ± standard error of the slope, the squared correlation coefficient and the p value of the slope.
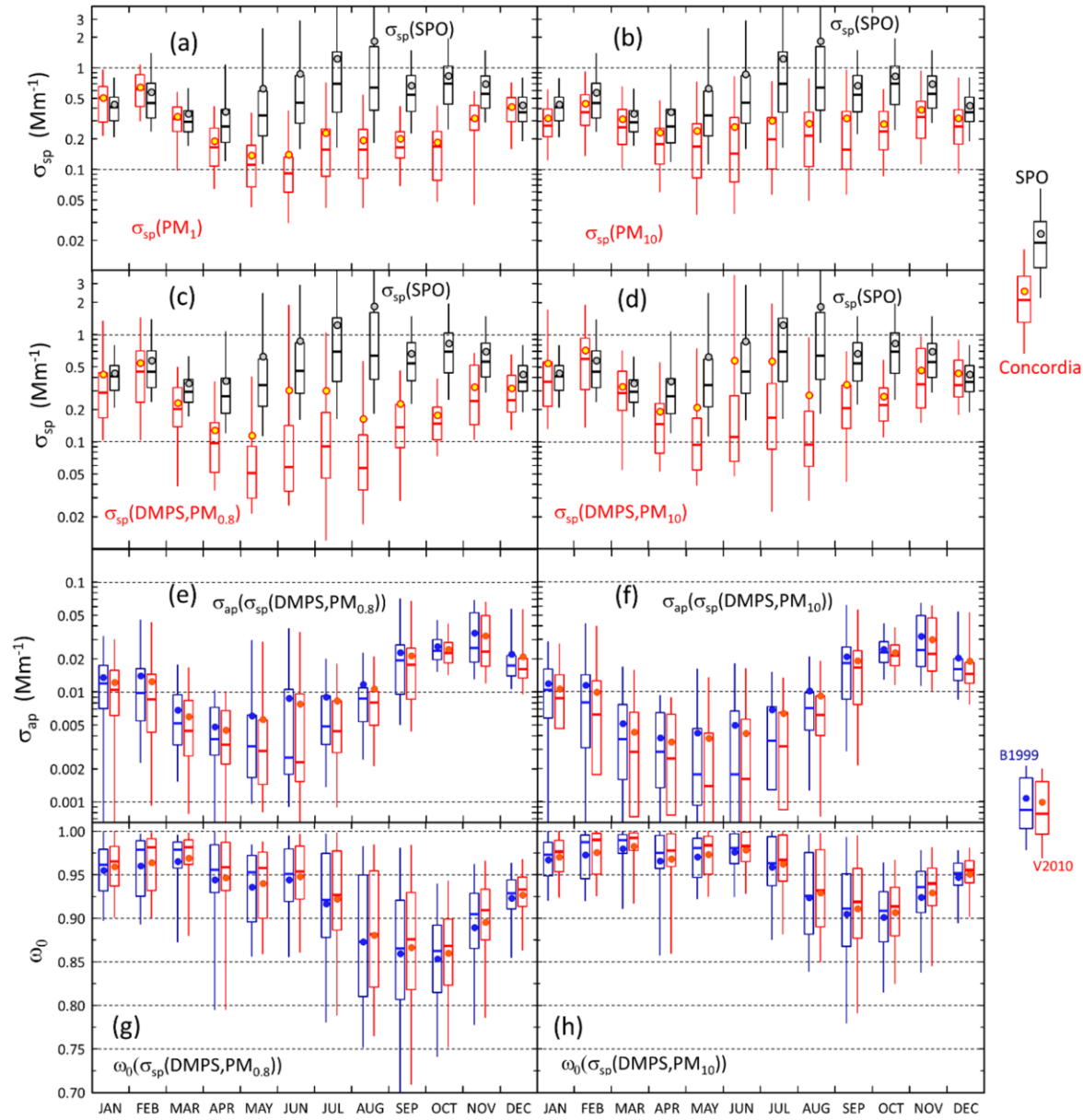
2   Figure 9. Seasonal cycles of scattering and absorption coefficients and single-scattering albedo. a) Scattering

3   coefficient (σ_{sp}) calculated from the sums of analyzed ion concentrations in PM_1 filters at λ = 550 nm, b) σ_{sp}

4   calculated from the sums of analyzed ion concentrations in PM_{10} filters, c) the lower estimate of σ_{sp} =

5    $\sigma_{sp}(DMPS,PM_{0.8})$, d) the upper estimate of σ_{sp} = $\sigma_{sp}(DMPS,PM_{10})$, e) absorption coefficient σ_{ap} calculated with

6   the algorithms of B1999 and V2010 (Eqs. (17) and (18))   by using the σ_{sp} lower estimate for scattering

7   correction, f) σ_{ap} calculated with the two algorithms by using the σ_{sp} upper estimate for scattering correction, g)

8   single-scattering albedo ω_o calculated by using the σ_{sp} lower estimate for both σ_{sp} and σ_{ap} and h) ω_o calculated

9   by using the σ_{sp} upper estimate for both σ_{sp} and σ_{ap}.
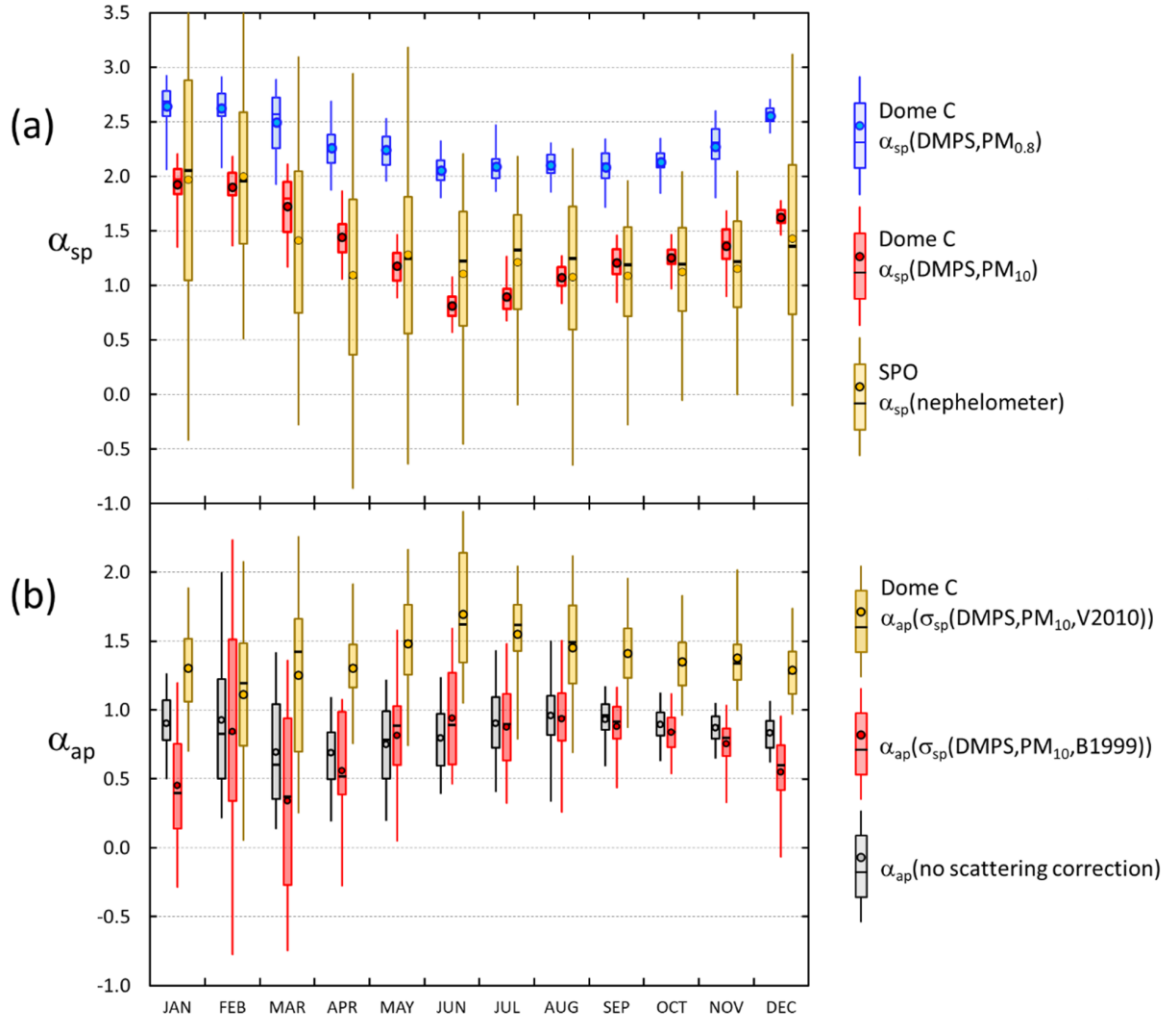
Figure 10. Seasonal cycles of the wavelength dependency of a) scattering and b) absorption. In a) the Ångström

exponent α_{sp} was calculated from the size distributions measured at Dome C (σ_{sp}(DMPS,PM$_{0.8}$) and

σ_{sp}(DMPS,PM$_{10}$) for the wavelength range $467 - 660$ and measured at the South Pole Station with a

nephelometer. The SPO α_{sp} was calculated for the wavelength range $550 - 700$ nm. In b) the absorption

Ångström exponent α_{ap} was calculated for the σ_{ap} without scattering correction, and by using the B1999 and

V2010 algorithms with scattering corrected using $\sigma_{sp} = \sigma_{sp}$(DMPS,PM$_{10}$), In all of them the data with $\sigma_{ap} > 3\delta\sigma_{ap}$

were used.
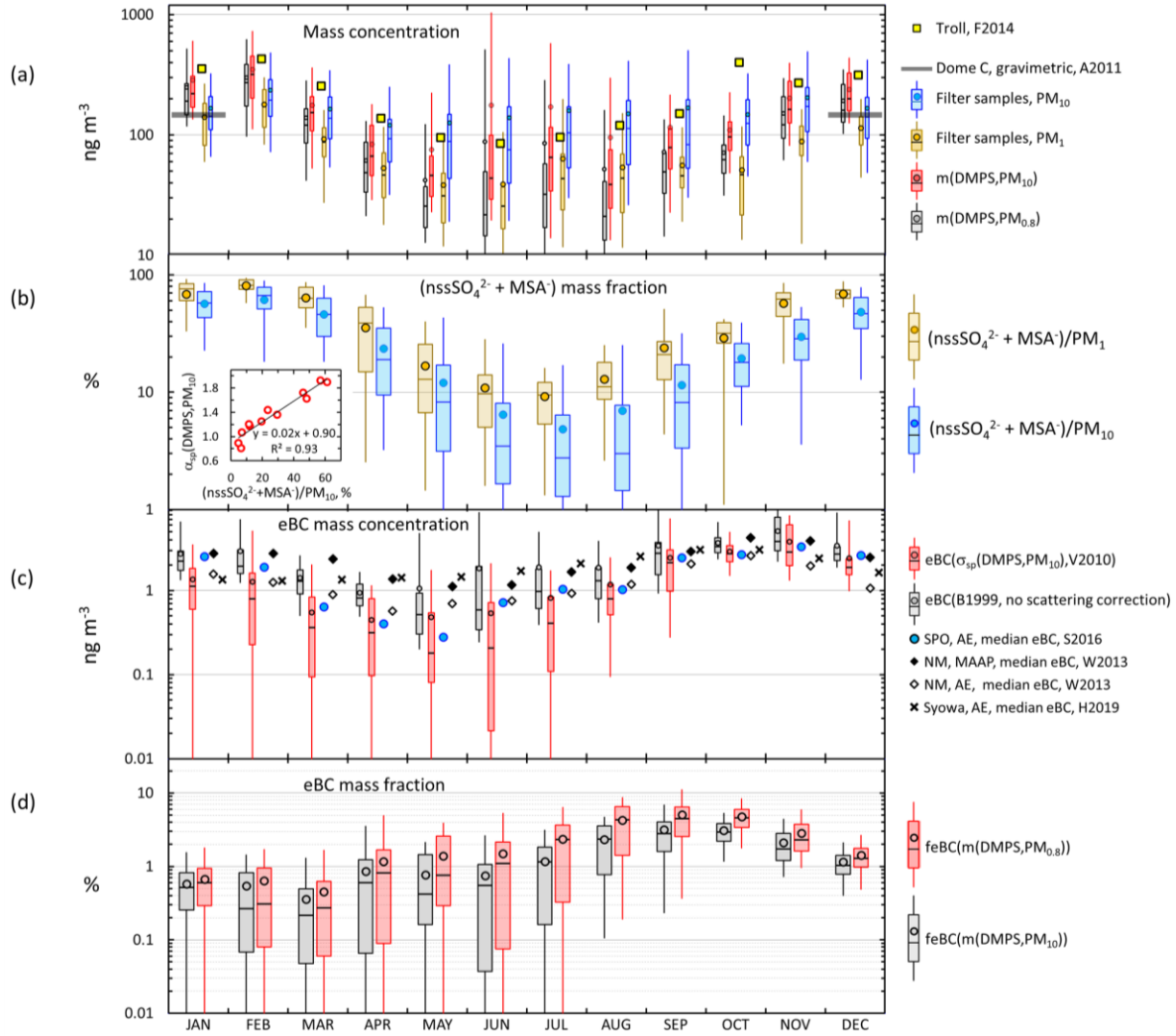
Figure 11. Seasonal cycles of a) aerosol mass concentration calculated from the particle number size distributions m(DMPS,PM$_{10}$) and m(DMPS,PM$_{0.8}$), the sum of ions analyzed from PM$_1$ and PM$_{10}$ filters, b) mass fraction of the sum of nssSO$_4^{2-}$ and MSA in PM$_1$ and PM$_{10}$ filters, c) equivalent black carbon (eBC) concentration calculated from the non-scattering-corrected absorption coefficients, and from σ_{ap} corrected with the σ_{sp} upper estimate (σ_{sp}(DMPS,PM$_{10}$)), d) mass fraction eBC calculated as the ratio of eBC corrected with the σ_{sp} upper estimate to m(DMPS,PM$_{0.8}$) and m(DMPS,PM$_{10}$). Comparison values: a) monthly average mass concentration calculated from particle volume concentrations at Troll (F2014: Fiebig et al., 2014), average gravimetric PM$_{10}$ mass concentration at Dome C (A2011: Annibaldi et al., 2011), c) monthly median eBC concentrations measured at Neumayer (NM) with a MAAP and an Aethalometer (AE) (W2013: Weller et al., 2013), at SPO with an Aethalometer (S2016: Sheridan et al., 2016), and at Syowa with an Aethalometer (H2019: Hara et al., 2019). The small insert in b) shows the scatter plot and linear regression of monthly average α_{sp}(DMPS,PM10) vs. monthly average mass fraction of the sum of nssSO$_4^{2-}$ and MSA in PM$_{10}$ filters.
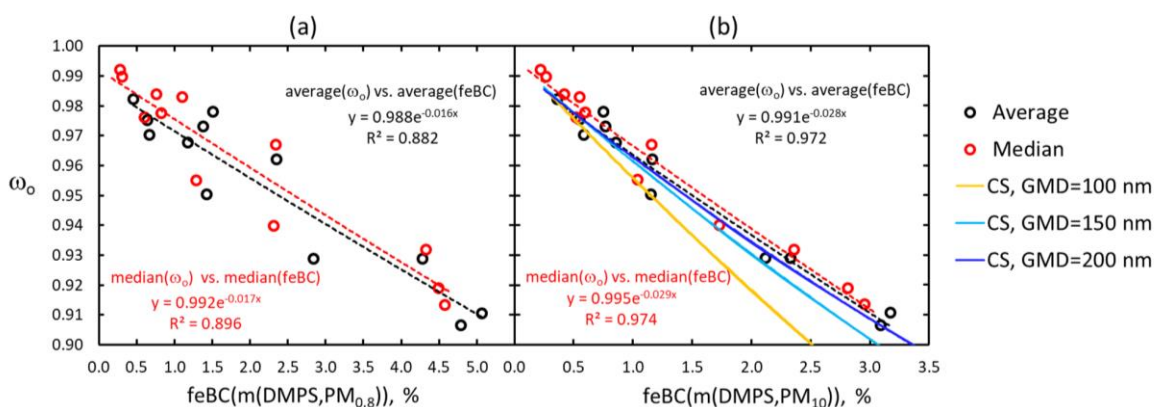
2   Figure 12. Monthly average and median ω_o vs. eBC mass fraction calculated as the ratio of eBC to a)

3   m(DMPS,PM$_{0.8}$) and b) m(DMPS,PM$_{10}$). The dashed lines represent fittings of ω_o(feBC) = ω_o(0)exp(-k·feBC) with

4   the data. The continuous lines in b) represent simulations with a core-shell (CS) model for lognormal number

5   size distributions with geometric standard deviation GSD = 1.8 and geometric mean diameter GMD shown in

6   the legend.
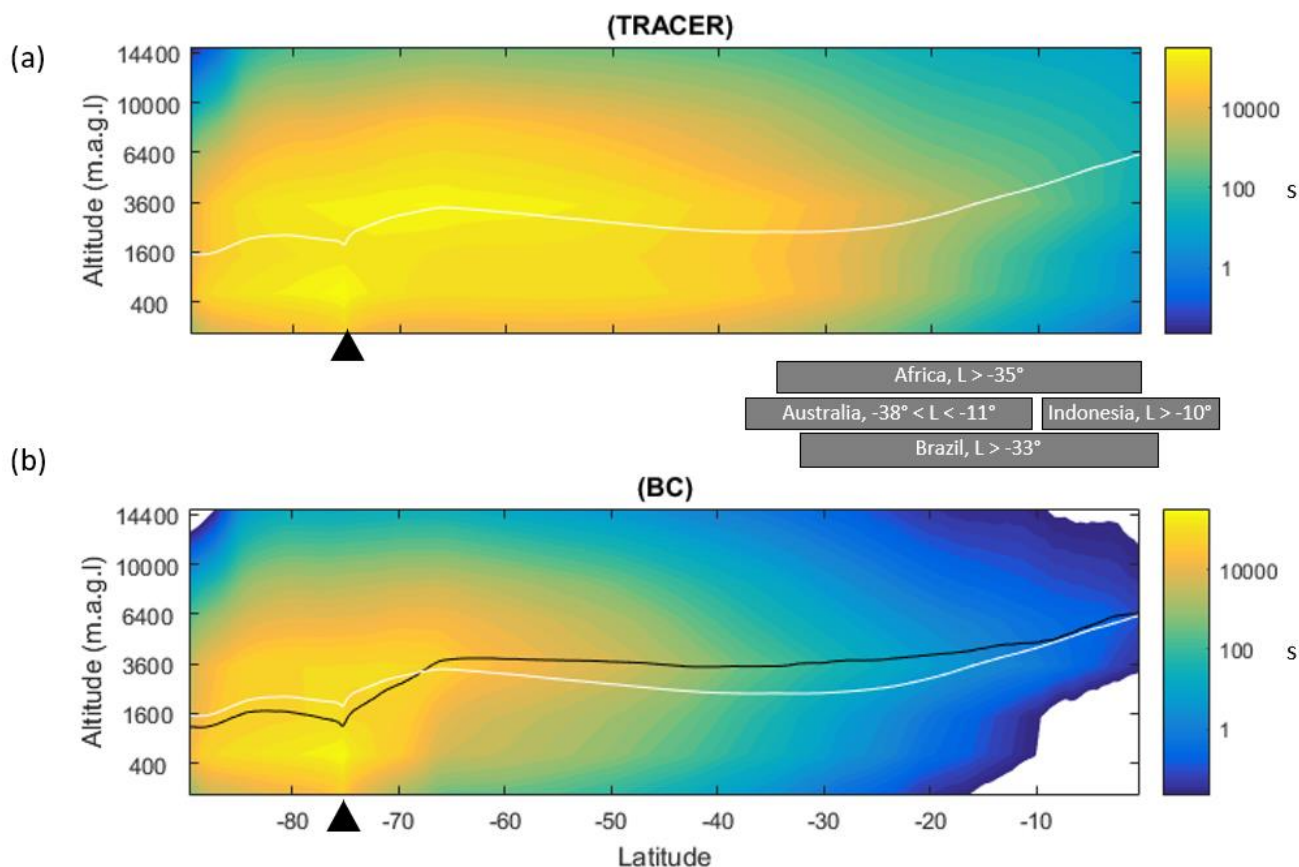
2 Figure 13. The residence time of 60000 50-day FLEXPART backtrajectories arriving at Dome C in 2008

3 – 2013 as a function of latitude and altitude above ground level. The residence time is colorcoded

4 from blue to yellow to show increasing time spent in each grid cell. a) The residence times of the inert

5 tracer backtrajectories. White line: the average altitude of trajectories at each latitude. b) Same as the

6 in (a) but for the BC tracer. Black line: the average altitude of the BC tracer, the white line is for

7 comparison average altitude of the inert tracer. The black triangle shows the latitude of Dome C

8 (75°06'S). The grey text boxes between a) and b) show the approximate latitude range of some major

9 BC emitting regions.

2   (a)   (b)
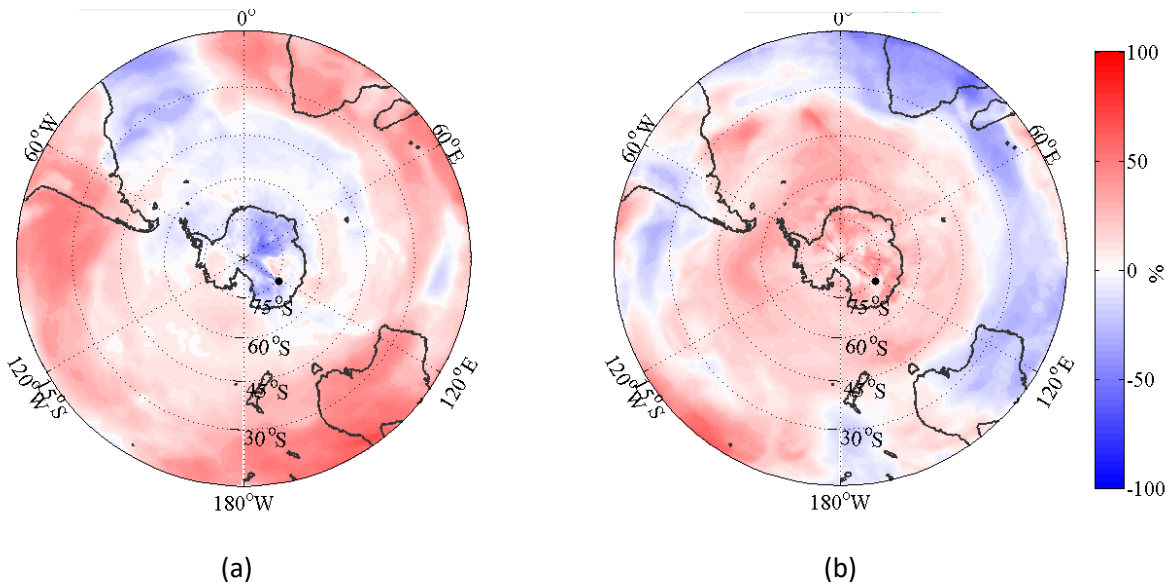
3   Figure 14. The relative difference RD, Eq. (19), of transport for the two lowest layers (>1000 magl) between the

4   highest and the lowest 10% of a) eBC concentration and b) single-scattering albedo. Positive values indicate a

5   relative increase in transport, and negative values a decreased transport from a given area by the highest 10%

6   of measurements.
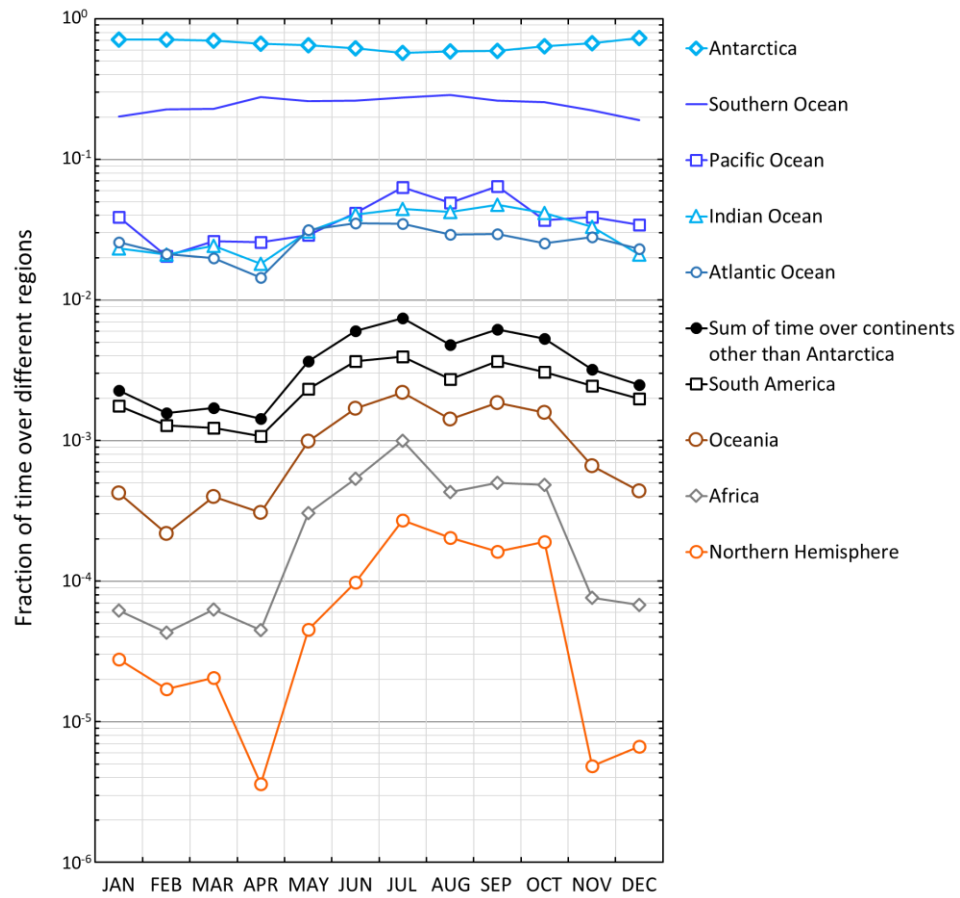
2 Figure 15. Seasonal air mass transport by region calculated as the fraction of time the FLEXPART 50-day

3 trajectories spent over Antarctica, the surrounding oceans and continents.
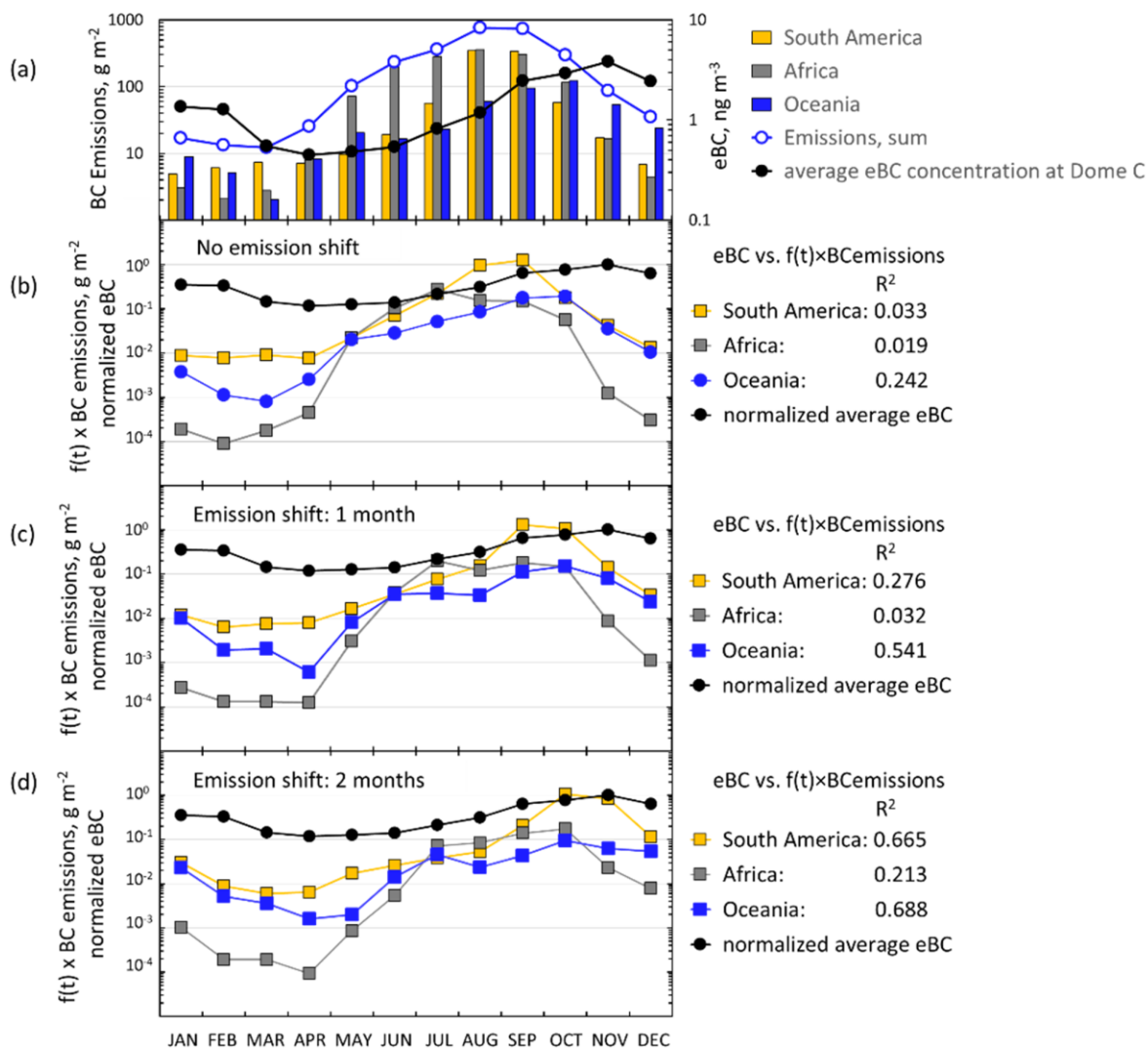
Figure 16. Seasonal cycles of fire-related BC emissions from the surrounding continents and eBC concentration
at Dome C. a) BC emissions and eBC concentrations, b) RTW BC emissions, c) f(t) × BC emissions 1 month
earlier, d) f(t) × BC emissions 2 months earlier. The numbers show the squared correlation coefficient of linear
regression between eBC concentrations and f(t) × BC emissions with the shown time shifts.
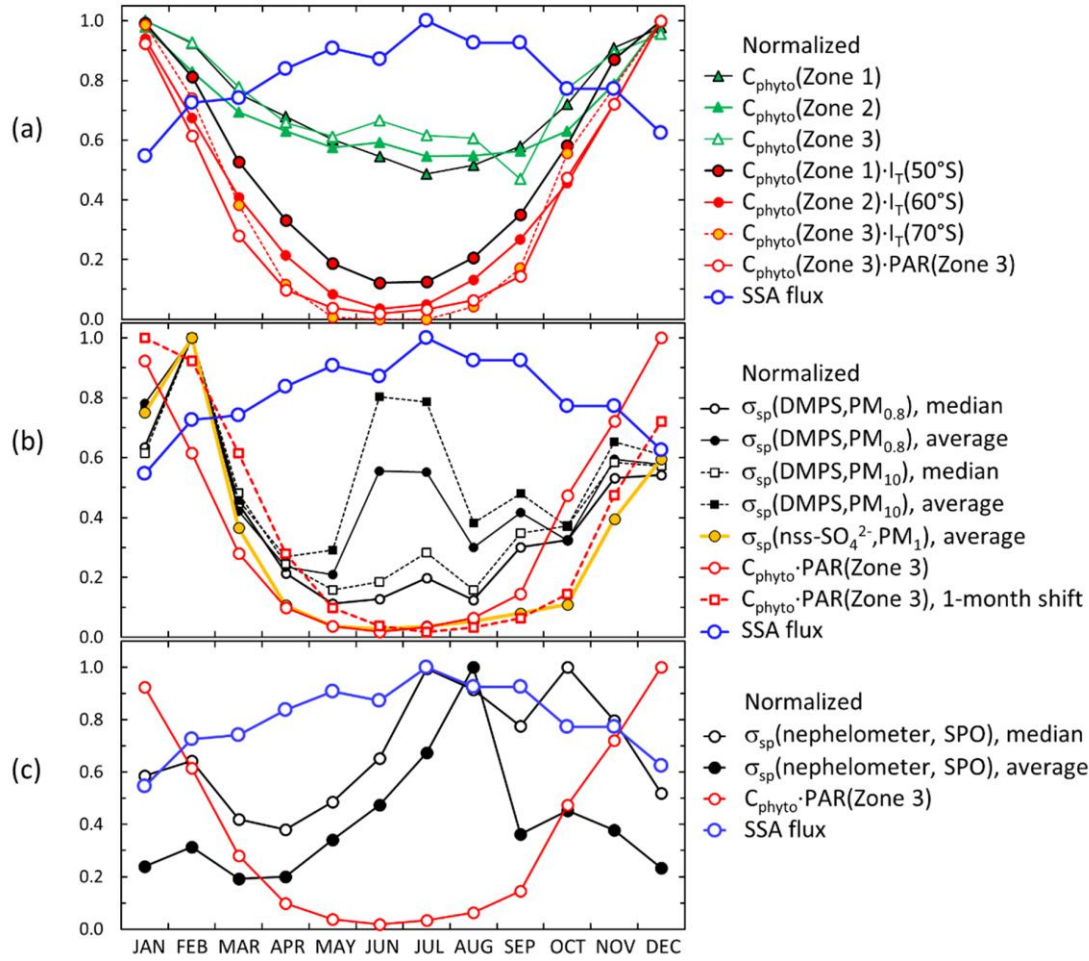
Figure 17. Normalized seasonal cycles of a) major natural sources of light-scattering aerosols from the oceans, b) scattering coefficients at Dome C and c) scattering coefficients at SPO. $\sigma_{sp}(DMPS,PM_{0.8})$ and $\sigma_{sp}(DMPS,PM_{10})$: scattering coefficient calculated from particle number size distributions; $\sigma_{sp}(nss\text{-}SO_4^{2-},PM_1)$: scattering coefficient calculated from non-seasalt sulfate concentrations in PM_1 filter samples; $\sigma_{sp}(nephelometer, SPO)$: scattering coefficient measured with the nephelometer at SPO; C_{phyto}: phytoplankton biomass concentration in 2008 – 2013 calculated as monthly averages from the time series presented by Behrenfeld et al. (2016) using CALIOP satellite data in Zone 1 (45° – 55°S), Zone 2 (55° – 65°S), and Zone 3 (65° – 75°S); $I_T(50°S)$, $I_T(60°S)$ and $I_T(70°S)$: average global radiation at latitudes 50°S, 60°S and 70°S at longitude 0° at 10 – 14 UTC; PAR(Zone 3): photosynthetically active radiation from Behrenfeld et al. (2016); SSA: Sea Spray Aerosol flux modeled according to Grythe et al. (2014).
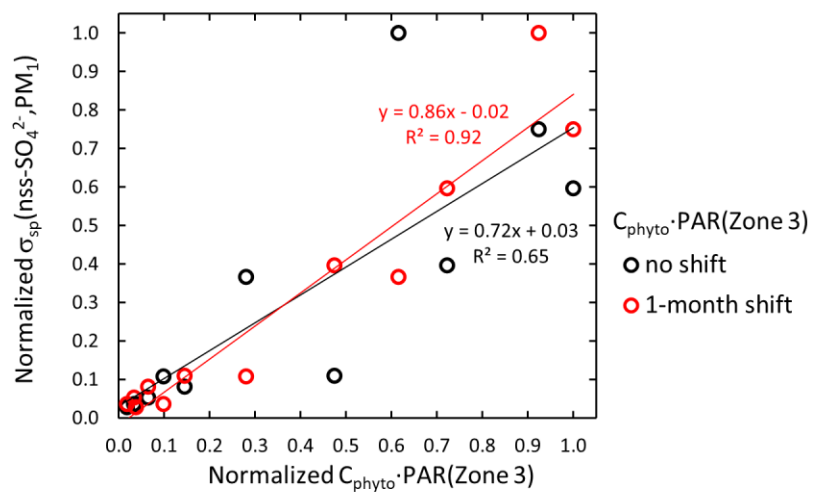
2 Figure 18. Normalized monthly average scattering coefficients calculated from the nss sulfate concentrations of

3 the PM_1 filter samples $\sigma_{sp}(nssSO_4^{2-},PM_1)$ at Dome C vs. normalized monthly averages of $C_{phyto}PAR$ in polar

4 latitude zone with and without a time shift.